Coupling between complex multiphase chemistry and detailed microphysics in a size-resolved cloud model

Von der Fakultät für Umweltwissenschaften und Verfahrenstechnik
der Brandenburgischen Technischen Universität Cottbus zur
Erlangung des akademischen Grades eines Doktor-Ingenieurs
genehmigte Dissertation

vorgelegt von

Diplom-Ingenieur Aerodynamiker

Aissa Mounir Sehili

aus Bordj Bou Arreridj, Algerien.

Gutachter: Prof. Dr. Eberhard Renner
Gutachter: Prof. Dr. Detlev Möller
Gutachter: Prof. Dr. Thomas Trautmann

Tag der mündlichen Prüfung: 17 November 2005

Acknowledgements

My first thanks go to my dear parents and my beloved wife. Without their sacrifice this thesis would not have been written. Many thanks also to all people who helped me during the long way that was the achievement of the present work. Especially, I would like to express my gratitude to Dr. Ralf Wolke for his support, advice and guidance during all the time that took this work. He was the true advisor, generous and patient. Dr. Oswald Knoth had his door always open for my questions, and I appreciated that very much. Thank you both. Beyond of being a very helpful colleague in discussing meteorological questions Dr. Olaf Hellmuth is an intimate friend. His support was in many situations decisive. May him find here the expression of my faithful gratitude. I acknowledge Dr. Martin Simmel for his help in the discussion of the microphysical issues and Dr. Jürgen Helmert for providing me in many cases with smart ideas and tricks for latex documents and presentations. The special environment at the modeling department of the Institute for Tropospheric Research (IFT) do deserve credit in the progress of this thesis. This place with its friendly and helpful atmosphere and the kindness of its director Prof. Eberhard Renner allowed me to overcome all difficulties. I would like to cite here all my colleagues in room 113, Thomas Jägemann, Wolfram Schröder and Katja Schmieder for their support.
I am also grateful to Prof. Detlev Möller and Prof. Thomas Trautmann for showing interest in my work and being on my committee.
The present work was supported by the BMBF in the framework of AFO2000 (07ATF40) joint project. Furthermore, I thank the NIC Jülich and DWD Offenbach for good cooperation.

Contents

Abbreviations

AMF	approximate matrix factorization
BDF	backward differentiation formula
CAPRAM	Chemical Aqueous Phase RAdical Mechanism
CCN	cloud condensation nuclei
CPU	central process unit
DGM	discontinuous Galerkin method
DWD	german weather service
EM	externally mixed
FEBUKO	field investigations of budgets and conversions of particle phase organics in tropospheric cloud processes
GDE	general dynamic equation
IM	internally mixed
IMEX	implicit-explicit scheme
LDM	linear discrete method
LM	non-hydrostatic limited area model (DWD)
LSODE	linear solver of ODEs systems
LWC	liquid water content
MODMEP	modeling of tropospheric multiphase processes: tools and chemical mechanisms
MPI	message passing interface
MUSCAT	MUltiScale Chemistry Aerosol Transport
NWM	non water mass
NUMFRAC	number of discretization fractions
ODE	ordinary differential equation
RESCHEM	resolution parameter for chemistry discretization
ROS2	Second order non-autonomous Rosenbrock method
RTOL	relative tolerance of the numerical scheme
SCE	stochastic collection equation
SPACCIM	SPectral Aerosol Cloud Chemistry Interaction Model
UTC	universal time

List of Tables

List of Figures

Chapter 1

Introduction

Multiphase processes are accepted to be of increasing importance in the comprehension of atmospheric processes. On the one hand, they directly influence the life cycles of trace constituents and facilitate conversions of these trace constituents, which are not possible or very inefficient in the pure gas phase. On the other hand, they strongly influence cloud formation and the radiation budget of the atmosphere. Several model studies have indicated that considering the liquid phase as sink for trace gases fundamentally modifies the chemistry in the gas phase (Lelieveld and Crutzen, 1991; Kreidenweis et al., 2003; Barth et al., 2003). Many recently available models focus either on complex multiphase chemistry only in a few aggregated drop classes (Audiffren et al., 1998; Herrmann et al., 2000; Djouad et al., 2002; Ervens et al., 2003), or detailed microphysics for strongly simplified chemical mechanisms (Liu and Seidl, 1998; Bott, 1999; Fahey and Pandis, 2001). To better understand the interaction, effects and evolution of the different physico-chemical processes taking place in the atmosphere (Fig. 1.1) their modeling requires a detailed description of all transformations with equal rigor. The efforts invested in the last years to develop sophisticated cloud models with complex multiphase chemistry allows more detailed studies on the interaction between microphysical and chemical multiphase processes (Leriche et al., 2003; Ervens et al., 2004b). In the coupled model of Leriche et al. (2000, 2001), the natural variability of cloud droplets is parameterized in a quasi-spectral form. Ervens et al. (2004a,b) use a model with moving droplet radii with 10 different fractions combined with complex inorganic and organic chemistry. Chemical conversions within cloud drops are essentially determined by the mass transfer between gas and liquid phases. Numerical studies show that these phase transitions must be described dynamically (Audiffren et al., 1998; Chaumerliac et al., 2000; Djouad et al., 2003). Furthermore, the phase interchange depends strongly on the phase surface area (Fahey and Pandis, 2001; Kreidenweis et al., 2003). Therefore, a highly resolved drop spectrum should be considered for an appropriate description.

The air parcel model SPACCIM ("SPectral Aerosol Cloud Chemistry Interaction

Model") is developed for the description of cloud processes by coupling complex multiphase chemistry and detailed microphysics. The description of both process groups is given for a size-resolved particle/drop spectrum. The droplets are subdivided into several classes. This discretization of the droplet spectrum into classes is based on droplet size. Additionally, the amount of scavenged material inside the drops can be taken into account depending on the used microphysical approach. All meteorological parameters needed by the multiphase chemistry are taken from the microphysical model. For this purpose, a new coupling scheme between microphysical and multiphase chemical models is implemented. This approach allows the coupling of the complex multiphase chemistry model with microphysical codes of different types (Sehili et al., 2005a). The coupling scheme provides time-interpolated values of the microphysical parameters (temperature, pressure, water vapor and liquid water content) and time-averaged mass fluxes between different droplet classes caused by microphysical processes, e.g., by condensation, coagulation and break up. Changes of the chemical aerosol composition by gas scavenging and chemical reactions feed back on the microphysical processes, e.g., water condensation growth rates via changes in surface tension and the Raoult term. The movement of the air parcel can follow a predefined trajectory. Entrainment and detrainment processes are included in a parameterized form. The model allows a detailed description of the transformation of gases and particles shortly before cloud formation, during the cloud life time and shortly after cloud evaporation.

The model equations resulting from multiphase chemical systems are nonlinear, highly coupled and extremely stiff. Multiphase systems are in general much stiffer than pure gas phase systems (Djouad et al., 2002). Explicit time integration methods are not suitable for an efficient integration of very stiff systems (Sandu et al., 1997a,b), since stability requirements can be maintained for very short time steps only. Therefore, implicit methods for treating multiphase processes have been investigated (Jacobson, 2002; Fahey and Pandis, 2001; Djouad et al., 2002). In our approach (Wolke et al., 2001; Wolke and Knoth, 2002), the aqueous phase and gas phase chemistry, the mass transfer between the different droplet classes, among droplets of the same class and with the gas phase are integrated in an implicit and coupled manner by a higher order Backward Differentiation Formula (BDF) method. For this part a modification of the code LSODE (Hindmarsh, 1983) with special linear system solvers is used. A second order non-autonomous Rosenbrook time integration scheme is also implemented. These direct sparse techniques exploit the special block structure of the corresponding Jacobians. Furthermore, we utilize an approximate matrix factorization which decouples multiphase chemistry and microphysical exchange processes of liquid water at the linear algebra level. The sparse Jacobians are generated explicitly and stored in a sparse form.

In the following, we will present the theoretical background and principles of both microphysical and multiphase chemistry models, the methodology adopted to

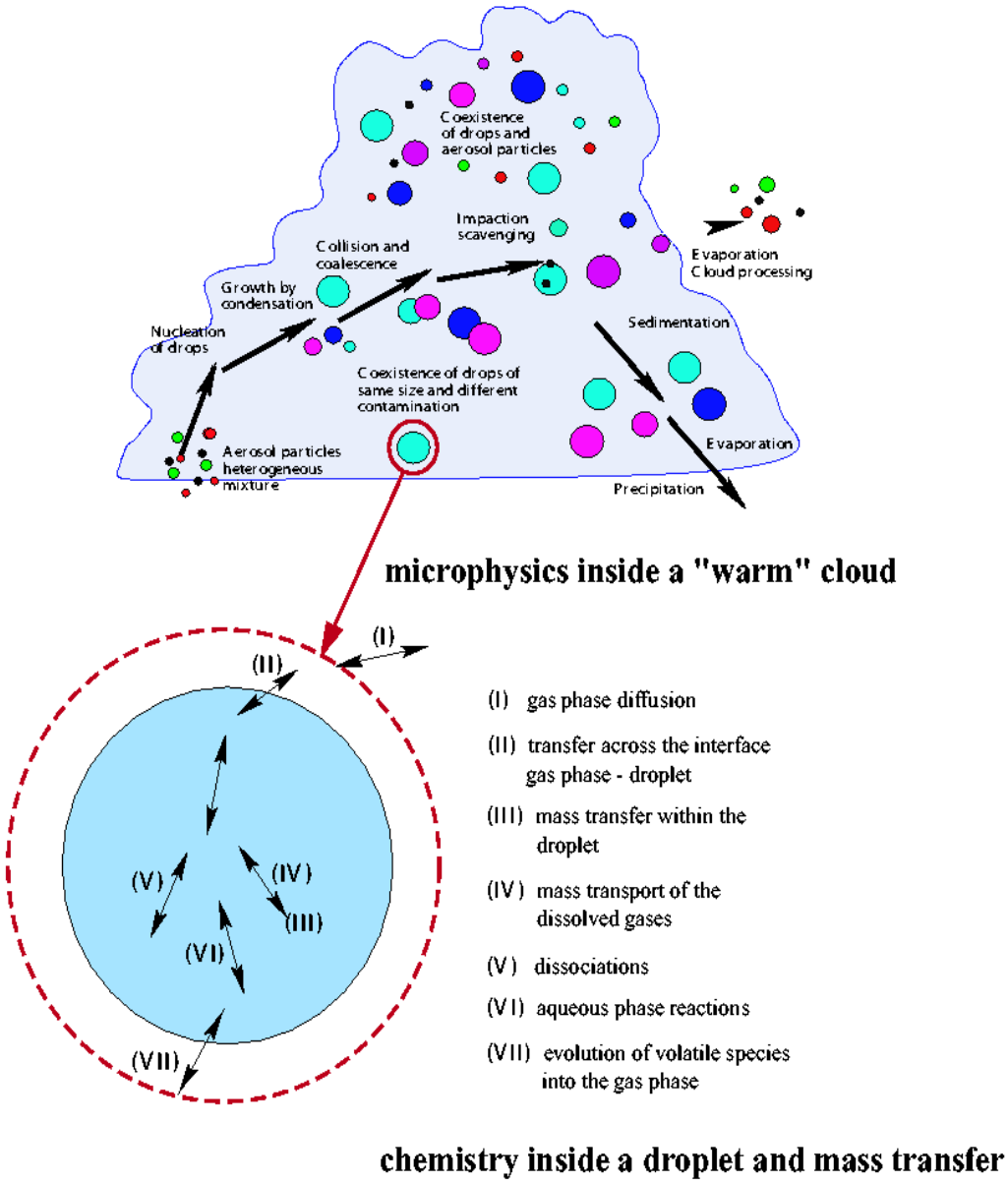

Figure 1.1: Schematic representing the physico-chemical processes taking place in a "warm" cloud.

realize the coupling, the applied numerical techniques and the sensitivity of the coupled model against changes in microphysics as well as the used control parameters. The numerical efficiency and robustness are investigated for a rising parcel test scenario (Kreidenweis et al., 2003; Sehili et al., 2005a) and one scenario derived from FEBUKO data (Herrmann et al., 2005a). An inorganic chemical scheme and four CAPRAM versions (Herrmann et al., 2000; Ervens et al., 2003; Herrmann et al., 2005b) of different complexity are used. The model simulations are compared with several measurements of the FEBUKO field campaign.

Furthermore, a comparison of SPACCIM driven by four different microphysical models with a fully coupled model is achieved. For that, two different test scenarios involving two initial compositions are developed. The simulations are performed using three different mechanisms. The behavior of the model in situations other than a hill cap cloud or cumulus cloud was also investigated. This aims to simulate cloud types where coagulation can play a substantial role. Thus, the coupled model is tested for air parcels driven by synoptic events. Two scenarios are simulated emphasizing on the quality and the importance of some parameterizations and parameters respectively. During the second scenario, a comparison is performed with the 3D coupled meteorology-chemistry-transport system LM-MUSCAT.

Along the present work we will demonstrate that the new developed coupled model is a powerful tool to understand and handle the physico-chemical processes that take place in a "warm" cloud. The model allows a high flexibility to couple different size resolved microphysical approaches to a complex multiphase chemistry using implicit time integration schemes.

Chapter 2

The microphysical model

2.1 Theoretical background

Cloud formation is a process that requires specific background conditions. It starts with the phase transition of water vapor molecules to nucleate into embryonic droplets. The stability of such droplets is reached when a certain critical size is exceeded. If this is the case, particles continue to grow by condensation as long as enough humidity is available. Otherwise, they may evaporate. In parallel, two other main processes responsible, respectively, for the broadening or the shrinking of the droplets size spectrum are active, namely the coagulation and break up of droplets. In a open system (non-adiabatic), one should also take into account the source and removal processes (entrainment/detrainment).

In order to model the cloud processes, many authors have developed a number of models that assume either a continuous size spectrum or discrete classes that vary in size in order to simulate changes in the size distribution of aerosols. Whitby and Mc Murry (1997) present a comparison of available numerical aerosol modeling techniques. The microphyical model (Simmel et al., 2002) involved in our work is based on a bin-wise representation of the particle spectrum after Gelbard and Seinfeld (l980). The General Dynamic Equation (GDE) which governs the physical processes undergone by particles (nucleation, condensation, evaporation, coagulation and breakup) is written as (Friedlander, 1977)

$$\begin{aligned}\frac{\partial n(m,t)}{\partial t} &= -\frac{\partial}{\partial m}[I(m)n(m,t)] \\ &+ \frac{1}{2}\int_0^m n(m-m',t)n(m',t)K(m-m',m')\,\mathrm{d}m' \\ &- n(m,t)\int_0^\infty n(m',t)K(m,m')\,\mathrm{d}m' \\ &- n(m,t)P(m) + \int_m^\infty n(m',t)Q(m',m)P(m')\,\mathrm{d}m' \\ &+ J_0(m,t)\delta(m-m_0) + S(m) + R(m),\end{aligned} \tag{2.1}$$

where $n(m,t)$ is the number concentration of particles of mass m, measured per unit volume at time t. The mass m represents the total mass of the particle (aerosol and water). The first term in the right hand side of (2.1) describes the condensation/evaporation process. $I(m)$ is the rate of increase or decrease in particles mass as a result of water vapor diffusion. In the model $I(m)$ is given according to Rogers and Yau (1989). The second and third terms represent respectively the gain and loss parts of the so-called Stochastic Collection Equation (SCE) (Tzivion et al., 1987). It describes the continuous probabilistic evolution of a whole coagulating particle spectrum. The fourth term accounts for the probabilistic spontaneous break up after Srivastava (1971) and is the sum of a loss and gain terms. $J_0(m,t)\delta(m-m_0)$ represents the nucleation rate from the gas phase, $S(m)$ any source term and $R(m)$ is the rate of removal (e.g., wet and dry deposition).

2.2 Droplets activation

It is well known that droplets activation occurring in the atmosphere is the so-called heterogeneous activation initiated by micron and submicron aerosol particles present in the atmosphere which have a hygroscopic affinity and constitutes the so-called cloud condensation nuclei (CCN). The rate of cloud droplets formation is determined by the number of such nuclei. The solution effect due to the presence of the CCN in the droplets is represented by the so-called Raoult term. Additionally, the equilibrium vapor pressure over a droplet surface depends on its curvature. This is known as the Kelvin term and account for the temperature and droplet surface tension effects. It expresses the increase in saturation ratio over a droplet compared to a plane water surface. In the absence of CCN, higher water vapor pressures are required to reach the equilibrium for nucleating droplets. This is known as the homogeneous activation and is less probable. The equilibrium saturation ratio S_e

determined through the interaction of both effects cited above is given by

$$S_e = \frac{e_s(r)}{e_{s,w}} = 1 + \frac{A}{r} - \frac{B}{r^3} \tag{2.2}$$

$$\frac{A}{r} = \frac{2\sigma}{\varrho_w R_v T r} \qquad \text{the curvature effect} \tag{2.3}$$

$$\frac{B}{r^3} = \frac{3iM_s m_w}{4\pi m_s \varrho_w r^3} \qquad \text{the solution effect} \tag{2.4}$$

where $e_{s,w}$ is the saturation vapor pressure over bulk water and $e_s(r)$ the equilibrium vapor pressure over the surface of a spherical droplet of radius r with surface tension σ and density ϱ_w at the temperature T. R_v is the gas constant for water vapor. M_s stands for the mass of the solute of a molar mass m_s and i is the van't Hoff factor of ionic dissociation (Rogers and Yau, 1989). The molar mass of water is denoted by m_w.
The saturation vapor pressure $e_{s,w}$ is given by

$$e_{s,w}(T) = 6.112 \exp\left(\frac{17.67T}{T + 243.5}\right) \tag{2.5}$$

with $e_{s,w}$ in mb and T in C°. Fig. 2.1 called the Köhler curve illustrate the effect of the solution term on the equilibrium state of droplets for a constant term A. It is shown that the solution effect is predominant for small particles. Moreover, both curvature and solution effects can be neglected for particles larger in size than 10 μm.

2.3 Condensation, evaporation

The condensation evaporation rate $I(m)$ due to water vapor diffusion processes in (2.1) reads (Rogers and Yau, 1989)

$$I(m) = \frac{dm}{dt} = \frac{4\pi r(S - 1 - \frac{A}{r} + \frac{B}{r^3})}{[F_{ther} + F_{diff}]}, \tag{2.6}$$

with S being the ambient saturation ratio and

$$F_{ther} = \left(\frac{L}{R_v T} - 1\right)\frac{L\varrho_w}{KT} \qquad F_{diff} = \frac{\varrho_w R_v T}{De_s(T)}$$

representing the thermodynamic term associated with heat conduction and that associated with vapor diffusion respectively. D stands for the molecular diffusion

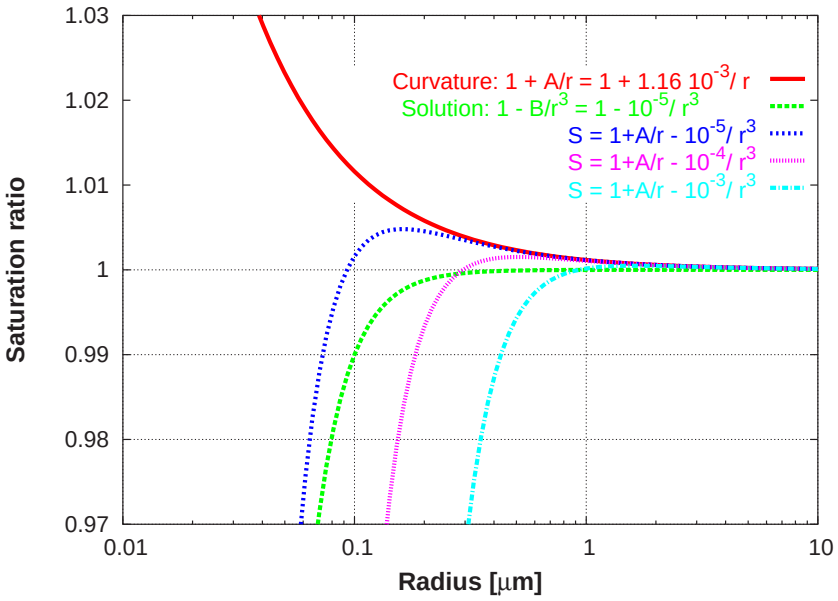

Figure 2.1: Modification of the hygroscopic behavior of the droplets caused by different solute masses.

coefficient. As discussed above, the rate of condensation/evaporation depends on the size and chemical composition of the particles. The free energy barrier which has to be surmounted for coating the particles increases with decreasing size and salt content.
The formulation of growth by diffusion is based on some assumptions which are not always satisfied. When dealing with particles ranging in size from submicrons to several hundred of microns the so-called kinetic effect has to be considered. For large particles, the continuum theory is the appropriated framework and for smaller ones the kinetic theory of the gases governs the flow. Interpolation formulas exist (Fukuta and Walter, 1970) allowing a correction for the transition regime. Furthermore, the ventilation effect due to distorted vapor field around a falling droplet, the nonstationary growth of droplets and the unsteady updraft effects represent sources of deviation for the presented diffusion theory.

2.4 Coagulation

The probabilistic growth of the particle spectrum governed by the SCE part of (2.1) requires the definition of a coagulation kernel $K(m, m')$ between two particles of masses m and m'. The most realistic kernel representing the probability that two particles collide and stick together is the combination of several kernels accounting

for Brownian diffusion, convective Brownian diffusion enhancement, gravitational collection, turbulent inertial motion and turbulent shear (Jacobson, 1999). The actual study introducing a new numerical scheme focuses only on the Brownian diffusion kernel and the gravitational collection kernel in order to make comparison with other well-accepted schemes using the same kind of kernels.

2.4.1 Brownian diffusion kernel

The Brownian kernel concerns the Brownian motion of particles suspended in the atmosphere diffusing and colliding randomly. It depends on the flow regime. To account the continuum, the free molecular and the transition regimes, the interpolation formula after Fuchs (1964) is used.
The Brownian kernel ($cm^3\ particle^{-1}s^{-1}$) after Fuchs is formulated by:

$$K_{i,j}^{B} = \frac{4\pi(r_i + r_j)(D_i + D_j)}{\frac{r_i+r_j}{r_i + r_j + (\delta_i^2 + \delta_j^2)^{1/2}} + \frac{4(D_i + D_j)}{(\bar{v}_{pi}^2 + \bar{v}_{pj}^2)^{1/2}(r_i + r_j)}}\ , \tag{2.7}$$

with r_i and r_j being the radii in centimeter of particles i and j,

$$\bar{v}_{pi} = \left(\frac{8k_BT}{\pi\bar{M}_{p,i}}\right)^{1/2}, \tag{2.8}$$

is the thermal velocity and $\bar{M}_{p,i}$ is the mass of one particle of size i.
D_i and D_j are the particle diffusion coefficients (cm^2s^{-1}) defined by

$$D_i = \frac{k_BT}{6\pi r_i\eta}\underbrace{\left[1 + Kn_i[A + Bexp(-CKn_i^{-1})]\right]}_{Cunningham\ slip-flow\ correction} \tag{2.9}$$

which reduces to Stokes-Einstein formula in the continuum regime where the Knudsen number satisfies $Kn_i \ll 1$. Let us remember that the Knudsen number represents the ratio between air mean free path and particle radius. Kasten (1968) suggests the values A=1.249, B=0.42, and C=0.87.
δ_i is a distance for interpolation defined by Fuchs as the mean distance from the enter of a sphere reached by particles leaving the surface of the sphere and traveling a distance of particle mean free path $\lambda_{p,i}$,

$$\delta_i = \frac{(2r_i + \lambda_{p,i})^3 - (4r_i^2 + \lambda_{p,i}^2)^{3/2}}{6r_i\lambda_{p,i}} - 2r_i, \qquad \lambda_{p,i} = \frac{2D_{p,i}}{\pi\bar{v}_{pi}} \tag{2.10}$$

In the continuum regime ($Kn_i \ll 1$) equation (2.7) simplifies to

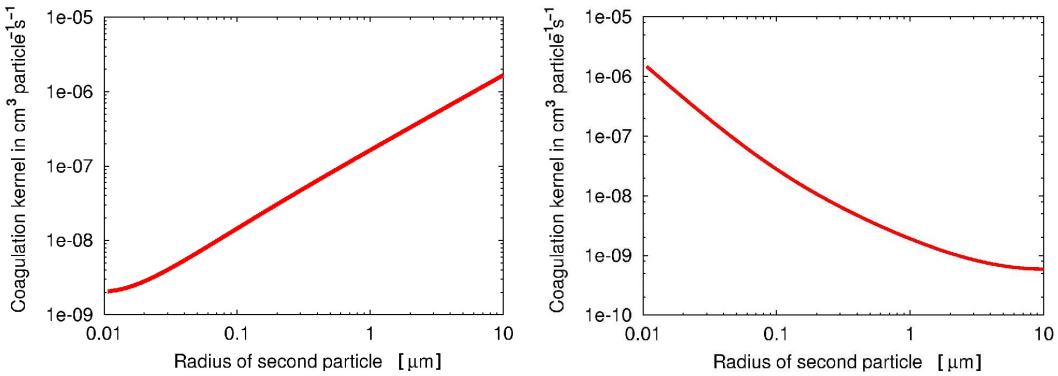

Figure 2.2: Brownian coagulation kernel when: a particle of 0.01 μm radius coagulates with particles of different sizes at 298 K (left), a particle of 10 μm radius coagulates with particles of different sizes at 298 K (right).

$$K_{i,j}^{B} = 4\pi(r_i + r_j)(D_i + D_j) \tag{2.11}$$

and in the free molecular regime ($Kn_i \gg 10$) to

$$K_{i,j}^{B} = \pi(r_i + r_j)^2(\bar{v}_{pi}^2 + \bar{v}_{pj}^2)^{1/2} \tag{2.12}$$

For small particles of the order of 1 μm, the Brownian kernel is increasing with the size of the collected particles (Fig. 2.2 left). This scheme is inverted for large particles of the order of 10 μm (Fig. 2.2 right). For small particles the Brownian kernel is predominant and represent a good approximation for the overall kernel when considering a primarily coagulation affecting the size distribution of particles smaller than 0.2 μm in diameter (Jacobson, 1999). Moreover, for a reliable description of cloud microphysical processes, it is necessary to take into account the remaining kernels.

2.4.2 Long kernel

The hydrodynamical kernel after Long (Long and Manton, 1974) reads

$$K_{i,j}^{G} = E_{i,j}\pi(r_i + r_j)^2 \mid V_{f,i} - V_{f,j} \mid, \tag{2.13}$$

where $E_{i,j}$ is the collection efficiency and reads $E_{i,j} = E_{i,j}^{coll}.E_{i,j}^{coal}$. Here, $E_{i,j}^{coll}$ is the collision efficiency. It represents the ratio of the number of collisions to the number for complete geometric sweep-out. It is approximated by (Tzivion et al., 1987)

$$E_{i,j}^{coll} = \begin{cases} 1 & \text{if } r_j \geq 50\mu\text{m}, \\ \max(4.5 \cdot 10^4\ r_j^2(1 - 3.10^{-4}/r_i), 10^{-3}) & \text{if } r_j < 50\mu\text{m} \end{cases} \tag{2.14}$$

The interaction after a collision depends on the droplets sizes and collision trajectories. It is influenced by any electrical fields that could exist. The ratio of the number of coalescences to the number of collisions $E_{i,j}^{coal}$ is the coalescence effeciency. It is assumed to be unity. This approximation is supported by experimental studies on small colliding droplets in the presence of electrical field which is the case in natural clouds. The terminal fall velocity of a particle in air is reached when its drag force is equal to the gravitational one. It results a relation of the form

$$V_x = \alpha x^{\beta}, \tag{2.15}$$

α and β depend on the flow regime (Rogers and Yau, 1989) and are given by

$$V_x = \begin{cases} k_1\, r^2, & k_1 = 1.19 \times 10^6\,\mathrm{cm^{-1}s^{-1}} & r \text{ up to about } 30\,\mu\mathrm{m} \text{ radius} \\ k_2\, r^{1/2}, & k_2 = 2.01 \times 10^3\,\mathrm{cm^{1/2}s^{-1}} & 0.6\,\mathrm{mm} < \ r\ < 2\,\mathrm{mm} \\ k_3\, r, & k_3 = 8 \times 10^3\,\mathrm{s^{-1}} & \text{in the intermediate size range} \end{cases} \tag{2.16}$$

The first and second size ranges correspond to very small and high Reynolds numbers flow regimes respectively. The third formula accounts for the intermediate regimes.

2.5 The Linear Discrete Method

One major task when developing a numerical model to solve the GDE is to select a mathematical representation for the particle size distribution function and to express the impact of microphysical processes on it. For that, the first step is the choice of the technique to be applied for the discretization in mass space. One has to decide between a modal, spline, sectional or monodisperse representation. The modal technique treat aerosols as separate multiple populations called modes (usually two or three modes). Each mode is represented by an independent continuous size distribution. The spline technique is similar to the modal one, but the different modes are connected so that one gets a single continuous function. The sectional and monodisperse techniques applied in the present work are based on the discretization of the mass space in a certain number of piece-wise bins. The two techniques are introduced in the following as "fixed bin" and "moving bin" approach respectively. In the "fixed bin" approach, the spectrum is discretized in a fixed grid according to the droplet diameter. Usually the grid size increases in a logarithmic scale. This grid is fixed over the whole simulation time and, therefore, particle sizes have to be "remapped" to the original grid. The changes in the droplet distribution caused by microphysical processes are described by mass and number fluxes between the corresponding size bins. In the "moving bin" representation, an initial size distribution based on a fixed grid discretization evolve with bins growing independently and no fluxes are generated. This approach can be considered only when no coagulation occurs and is a priori more exact but it do no allow to resolve the targeted distributions

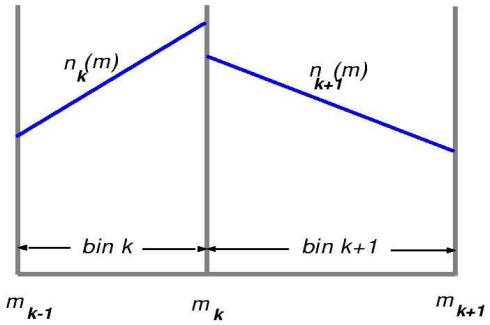

Figure 2.3: Schematic representation of the piece-wise linear approximation of the distribution function.

in some parts of the spectrum. The two methods are compared for different case studies in Chapter 7. A comparison of available numerical aerosol modeling techniques is available in Whitby and Mc Murry (1997). The Linear Discrete Method called LDM (Simmel et al., 2002) is the one implemented in the microphysical model which is involved in the coupled model SPACCIM (SPectral Aerosol Cloud Chemistry Interaction Model). It is a size-resolved method that approximates the number distribution as a piece-wise linear function in mass space. The accuracy and performance of this approach in comparison to other well accepted schemes has been demonstrated (Simmel et al., 2002). The mass is discretized over a number K of bins $[m_k, m_{k+1}]$ with $m_{k+1} = p \cdot m_k$. The spread of particles sizes over several orders of magnitude implies for their representation to consider a logarithmic size evolution through the special choice of the bin sizing factor p. In our case $p = 2$, which means that the mass is doubled after every bin. The method is a two moment scheme using particle number concentration and mass concentration, i.e.,

$$n_k(m) = \begin{cases} \alpha_k m + \beta_k & \text{if m}\in I_k, \\ 0 & \text{otherwise.} \end{cases} \tag{2.17}$$

The $j-th$ moment of the distribution function $n(m,t)$ in bin k is defined as

$$M_k^j = \int_{m_k}^{m_{k+1}} m^j n(m,t)\, dm \ . \tag{2.18}$$

Using this definition, the distribution function reads

$$n_k(m) = n_0 + p(m - m_M) \text{ for } m_k < m \leq m_{k+1},$$

The entity m_M designates the bin mean mass, $m_M = \dfrac{m_k + m_{k+1}}{2}$. The parameters n_0 and p of the linear distribution can easily be calculated using the two first

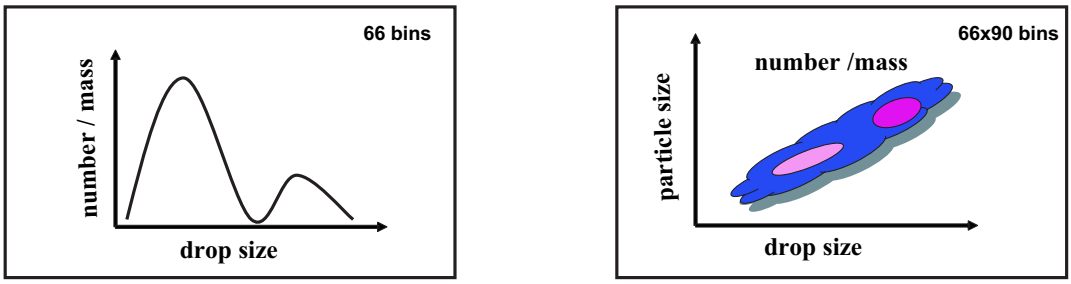

Figure 2.4: 1D (left) and 2D (right) discretization of particle/droplet spectrum.

moments N_k and M_k defined by

$$N_k = \int_{m_k}^{m_{k+1}} n_k(m)\, dm \ , \tag{2.19}$$

$$M_k = \int_{m_k}^{m_{k+1}} n_k(m) m\, dm \ . \tag{2.20}$$

For this piece-wise approximation over K bins one can write

$$n(m) \approx \sum_{k=1}^{K} n_i(m) = \hat{n}(m) \tag{2.21}$$

Fig. 2.3 describes schematically the piece-wise approximation of the distribution function.

One-dimensional particle distribution This microphysical model is based on the discretization in mass space of the one component general dynamic equation (Gelbard and Seinfeld, 1980) using the LDM. In this sectional approach, the number distribution is represented by a piecewise linear function over a prescribed number of size bins in the water mass space. Additionally, the soluble part in each bin is explicitly described for the calculation of the Raoult term (Simmel et al., 2002, 2005). The growth rate in the condensation/evaporation process and droplet activation are based on Köhler theory. Droplets are considered to be well diluted. In the present study, 66 bins and a sizing factor of 2 are applied. The range of the spectrum reaches from approximately 1 nm up to 5 mm. The model can operate in a "fixed bin" as well as in a "moving bin" mode. In the first case, the initial particle/droplet spectrum is discretized according to the water mass considered in equilibrium with the initial relative humidity. Note that droplets having the same size contain the same amount of aerosol (Fig. 2.4 left). The size distribution function is remapped to original grid every time step. Hence, this approach is seen as a semi-Lagrange method and can be a source of numerical diffusion for particle growth. In the "moving bin" case, the spectrum is obtained by discretizing the non-water mass of the particles. In

this way, the "moving bin" discretization does not depend on the initial humidity. This monodisperse approach is computationally more efficient. A limitation of this technique is the loss of the size distribution information.

Two-dimensional particle distribution. In this approach, the particles are classified according to their water mass and total aerosol mass on a two dimensional fixed grid which is comparable with the approach of Bott (2000). The discretization of the particle mass and water mass spectrum is similar to the 1D model. However, a finer resolution with a sizing factor $\sqrt{2}$ is used for the particle mass discretization. Similarly to the 1D model, the soluble part of the total particle mass is explicitly treated in the 2D spectrum (Fig. 2.4 right). The condensation process changes the particle properties on the water mass axis only but not on the aerosol mass axis. Therefore, the shift of water mass and particle number is calculated similar to the 1D approach by an extended LDM (Simmel and Wurzler, 2005). Additionally, the LDM is also applied to determine the shift of the soluble mass fraction in each size bin. Thus, droplets having the same size can show a different hygroscopic behavior.

2.6 The Discontinuous Galerkin Method

We present here a contribution to develop of a fully coupled model which should among other allow to describe microphysical processes of particles having a complex chemical composition. This is not possible whith the LDM which assumes a one component system. The discontinuous Galerkin (DGM) is based on the discretization in mass space of the multicomponent general dynamic equation (Pilinis, 1990) using a projection method. The discretization is a sectional one similar to the LDM but with a different formulation for the free parameters of the sectional linear distribution. The application of the DGM to the overall microphysical processes is beyond the focus of the present work. It is aimed in the following to present, test and evaluate this method for the coagulation process using initial data and results taken from literature. An application for condensation/evaporation process can be found in Knoth (2005). A comparison study between the LDM and the DGM method for a realistic multicomponent system is only possible when the microphysical model based on the LDM is coupled with a multiphase chemistry one. This comparison is presented in chapter 7.

The background and development of the method is first given for a one component system and then extended to the multicomponent one.

2.6.1 One component system

The size-resolved model approximates the number distribution function and the mass distribution function as a piece-wise continuous linear function similar to

(2.17). The mass is discretized over a K number of bins $[m_k, m_{k+1}](m_{k+1} = p \cdot m_k)$. The bin sizing factor p can be appropriately chosen.

The linear distribution function is of the form

$$n_k(m) = N_k[\alpha_k^N m + \beta_k^N] + M_k[\alpha_k^M m + \beta_k^M] \tag{2.22}$$

with N_k and M_k being the two first moments.
The parameters α_k^N, α_k^M, β_k^N and β_k^M depend only on m_k and m_{k+1} and read

$$\alpha_k^N = \frac{-6(m_{k+1} + m_k)}{(m_{k+1} - m_k)^3} \tag{2.23}$$

$$\alpha_k^M = \frac{4(m_{k+1}^2 + m_{k+1}m_k + m_k^2)}{(m_{k+1} - m_k)^3} \tag{2.24}$$

$$\beta_k^N = \frac{12}{(m_{k+1} - m_k)^3} \tag{2.25}$$

$$\beta_k^M = \frac{-6(m_{k+1} + m_k)}{(m_{k+1} - m_k)^3} \tag{2.26}$$

Identically to (2.21) one can write

$$n(m) \approx \sum_{k=1}^{K} n_i(m) = \hat{n}(m) \tag{2.27}$$

Before discussing the application of the DGM to the SCE, a short introduction to the theoretical background of the method is presented. We refer to Cockburn (1988) for more detail.

Let us consider the following model representing the rate of change in the density distributions function

$$\frac{\partial n(m,t)}{\partial t} = f(n,m,t) \qquad \text{in } (0,1) \times (0,T) \tag{2.28}$$

$$n(m,0) = n_0(m) \qquad \forall\, m \in (0,1) \tag{2.29}$$

The discretization in mass space is proceeded as follows
For each partition of the whole interval $\{m_k\}_{k=1}^N$ we set $I_k = (m_k, m_{k+1})$, with $\Delta m_k = m_{k+1} - m_k$ for $k = 1, \ldots, K$.
The approximate distribution function belongs to the finite element space for each time $t \in [0, T]$.
The finite element space is defined as

$$V_h = V_h^k \tag{2.30}$$

$$\equiv \{v \in L^1(0,1) : v\,|_{I_k} \in P^K(I_k), k = 1, \ldots, K\}\ . \tag{2.31}$$

$P^K(I)$ is the space of polynomials in I of degree at most K.
The determination of an approximate solution n_a is done through the use of a weak formulation.
Equations (2.28) and (2.29) are multiplied by arbitrary, smooth function $v(m)$ and integrated over I_k:

$$\int_{I_k} n_t v(m) dm - \int_{I_k} f(n, m, t) v(m) dm = 0 \ . \tag{2.32}$$

Then the smooth functions $v(m)$ are replaced by test functions belonging also to the finite element space.
In our case the order of the space of polynomials in I, i.e., $P^K(I)$ is $K = 1$. Consequently, the approximated test functions are piece-wise first order or lower.

$$\int_{I_k} n_t dm - \int_{I_k} f(n, m, t) dm = 0 \ , \tag{2.33}$$

$$\int_{I_k} n_t m dm - \int_{I_k} f(n, m, t) m dm = 0 \ . \tag{2.34}$$

The two last equations define the time derivatives of the two first moments (0-th and 1-st) of the distribution function. They represent the free parameters for the linear description of the piece-wise distribution function as we saw previously, i.e.,

$$\dot{N}_k = \int_{m_k}^{m_{k+1}} \dot{n} \, dm = \int_{m_k}^{m_{k+1}} f(n, m) \, dm \ , \tag{2.35}$$

and

$$\dot{M}_k = \int_{m_k}^{m_{k+1}} \dot{n} m \, dm = \int_{m_k}^{m_{k+1}} f(n, m) m \, dm \ . \tag{2.36}$$

The weak formulation of the Discontinuous Galerkin Method is aimed to give an approximate solution of a conservative law with a definition of a numerical flux. In the present case, the function $f(n, m, t)$ describing coagulation by the Stochastic Collection Equation is the sum of two integrals summarizing the gain and loss terms as shown above. There is no need to further development. The main remaining task is the computation of the integrals in equation (2.35) and (2.36) using the piece-wise description of the distribution function.
Setting then $n = \hat{n}$ we obtain a system of ordinary differential equations (ODE) of the form

$$\dot{N} = F^N(N, M) \ ,$$
$$\dot{M} = F^M(N, M) \ ,$$

where $N = (N_1, N_2, \cdots, N_K)^T$ and $M = (M_1, M_2, \cdots, M_K)^T$.

The Stochastic Collection Equation SCE part of (2.1) is used to figure out the behavior of the DGM during coagulation process. We consider in this section the development of the solution for

$$\dot{M}_k = F_k^M(N, M) \ , \tag{2.37}$$

which reads when applied to the SCE

$$\begin{aligned} \dot{M}_k = & \underbrace{\frac{1}{2}\int_{m_k}^{m_{k+1}} m\,dm \int_0^m n(m-m')K(m-m',m')n(m')\,dm'}_{gainterm\ [G]} \\ & - \underbrace{\int_{m_k}^{m_{k+1}} mn(m)\,dm \int_0^\infty n(m')K(m,m')\,dm'}_{lossterm\ [L]} \ , \end{aligned} \tag{2.38}$$

Introducing the new variables $u = m'$, $v = m - m'$ and using the fact that $\int_a^b dx \int_c^d F(x,y)dy = \int_c^d dy \int_a^b F(x,y)dx$ the gain term in (2.38) can be rearranged and reduced to a discrete form reading

$$[G] = \frac{1}{2}\int_0^{m_{k+1}} \int_{max\{m_k - v, 0\}}^{m_{k+1}-v} (u+v)n_i(v)K(v,u)n_j(u)\,dudv. \tag{2.39}$$

Furthermore, We introduce the test function θ defined as

$$\theta(m_k, m_{k+1}, u, v) = \begin{cases} 1 & \text{if } (u+v) \in [m_k, m_{k+1}] \\ 0 & \text{otherwise.} \end{cases} \tag{2.40}$$

The limit of integration should consider the overall possible gain sources coming in fraction $[m_k, m_{k+1}]$. Consequently, the gain term in (2.39) can be rewritten

$$[G] = \frac{1}{2}\int_0^{m_{k+1}} \int_0^{m_{k+1}} \theta(m_k, m_{k+1}, u, v)(u+v)K(u,v)n(u)n(v)dudv, \tag{2.41}$$

which is then decomposed into

$$[G] = \frac{1}{2}\int_0^{m_k} \int_0^{m_k} \theta(m_k, m_{k+1}, u, v)(u+v)K(u,v)n(u)n(v)dudv \tag{2.42a}$$

$$+ \int_{m_k}^{m_{k+1}} \int_0^{m_k} \theta(m_k, m_{k+1}, u, v)(u+v)K(u,v)n(u)n(v)dudv \tag{2.42b}$$

$$+ \frac{1}{2}\int_{m_k}^{m_{k+1}} \int_{m_k}^{m_{k+1}} \theta(m_k, m_{k+1}, u, v)(u+v)K(u,v)n(u)n(v)dudv \tag{2.42c}$$

The variables in the loss term in (2.38) are separated and this term can rewritten in the form

$$[L] = -\int_{m_k}^{m_{k+1}} vn(v) \int_0^{\infty} K(u,v)n(u)dudv, \tag{2.43}$$

and then decomposed in

$$\begin{aligned}
[L] &= -\int_{m_k}^{m_{k+1}} \int_0^{m_k} vK(u,v)n(u)n(v)dudv && \text{(2.44a)}\\
&- \frac{1}{2}\int_{m_k}^{m_{k+1}} \int_{m_k}^{m_{k+1}} (u+v)K(u,v)n(u)n(v)dudv && \text{(2.44b)}\\
&- \int_{m_k}^{m_{k+1}} \int_{m_{k+1}}^{\infty} vK(u,v)n(u)n(v)dudv && \text{(2.44c)}
\end{aligned}$$

Combining the integrals (2.42b) and (2.44a) and the integrals (2.42c) and (2.44b) one obtains finally

$$\begin{aligned}
I = [G] + [L] = \\
&\frac{1}{2}\int_0^{m_k} \int_0^{m_k} \theta(m_k, m_{k+1}, u, v)(u+v)K(u,v)n(u)n(v)dudv\\
&- \int_{m_k}^{m_{k+1}} \int_0^{m_k} \theta(m_{k+1}, \infty, u, v)vK(u,v)n(u)n(v)dudv\\
&+ \int_{m_k}^{m_{k+1}} \int_0^{m_k} \theta(m_k, m_{k+1}, u, v)uK(u,v)n(u)n(v)dudv\\
&- \frac{1}{2}\int_{m_k}^{m_{k+1}} \int_{m_k}^{m_{k+1}} \theta(m_{k+1}, \infty, u, v)(u+v)K(u,v)n(u)n(v)dudv\\
&- \int_{m_k}^{m_{k+1}} \int_{m_{k+1}}^{\infty} vK(u,v)n(u)n(v)dudv
\end{aligned} \tag{2.45}$$

Moreover, the kernel is approximated as being the sum of elementary kernels $\tilde{K_{ij}}$ for the interaction of bins i and j

$$K(u,v) = \sum_{i=1}^{K}\sum_{j=1}^{K} \tilde{K_{ij}}(u+v)\ . \tag{2.46}$$

Using the previous expression and replacing the linear approximation of the number

distribution function (2.27) in (2.45) the sectional solution of the SCE reads

$$\begin{aligned} I = &\sum_{i}^{k}\sum_{j}^{k}\frac{1}{2}\int_{m_i}^{m_{i+1}}\int_{m_j}^{m_{j+1}}\theta(m_k,m_{k+1},u,v)(u+v)^2\tilde{K_{ij}}n_i(u)n_j(v)dudv \\ &-\sum_{i}^{k}\int_{m_k}^{m_{k+1}}\int_{m_i}^{m_{i+1}}\theta(m_{k+1},\infty,u,v)v(u+v)\tilde{K_{ij}}n_i(u)n_j(v)dudv \\ &+\sum_{i}^{k}\int_{m_k}^{m_{k+1}}\int_{m_i}^{m_{i+1}}\theta(m_k,m_{k+1},u,v)u\tilde{K_{ij}}(u+v)n_i(u)n_j(v)dudv \\ &-\frac{1}{2}\int_{m_k}^{m_{k+1}}\int_{m_k}^{m_{k+1}}\theta(m_{k+1},\infty,u,v)(u+v)^2\tilde{K_{ij}}n_i(u)n_j(v)dudv \\ &-\sum_{i=k+1}^{K}\int_{m_k}^{m_{k+1}}\int_{m_i}^{m_{i+1}}v(u+v)\tilde{K_{ij}}n_i(u)n_j(v)dudv \end{aligned} \tag{2.47}$$

The integrand in (2.47) is piecewise polynomial in u and v and the resulting integrands can be computed exactly. If we insert the expression (2.22) in the last expression, the right hand side of (2.47) can be written as a bilinear function in N and M. The coefficients of this bilinear form depend only on the discretized mass space and can be computed in advance.

2.6.2 Multicomponent system

In a multicomponent system, assumption is made that particles having the same mass m are identically composed (internally mixed) with partial masses $m^l(m,t)$, $l = 1,\cdots,L$. L represents the number of the different components involved. This reads

$$m = \sum_{l=1}^{L} m^l(m,t) \tag{2.48}$$

In reality, the atmosphere contains also externally mixed (EM) particles contributing to the creation of new internally mixed particles or to existing ones by collision process. Taking into account this fact implies the resolution of a rather complicated model when a large number of particles types are involved. Consequently, the method is restricted to treat IM particle types.
The discretization is performed identically to the one component system.
The first moment of a mass fraction l over a section is defined as

$$M_k^l = \int_{m_k}^{m_{k+1}} m^l(m,t)n(m,t)\,dm\ , \tag{2.49}$$

with

$$M_k = \sum_{l=1}^{L} M_k^l \ . \tag{2.50}$$

To develop a solution for a coagulating multicomponent system, we write again for more clearness the SCE

$$\begin{aligned} \frac{\partial n(m,t)}{\partial t} = \frac{1}{2}\int_0^m n(m-m',t)n(m',t)K(m-m',m')\,\mathrm{d}m' \\ - n(m,t)\int_0^\infty n(m',t)K(m,m')\,\mathrm{d}m'. \end{aligned} \tag{2.51}$$

Multiplying the two sides of (2.51) with $m^l(m,t)$ and integrating them over the interval $[m_k, m_{k+1}]$ one gets

$$\begin{aligned} &\int_{m_k}^{m_{k+1}} \frac{\partial n(m,t)}{\partial t} m^l(m,t)\,dm = \\ &\quad \frac{1}{2}\int_{m_k}^{m_{k+1}} m^l(m,t)\,dm \int_0^m n(m-m')K(m-m',m')n(m')\,dm' \\ &\quad - \int_{m_k}^{m_{k+1}} m^l(m,t)n(m)\,dm \int_0^\infty n(m')K(m,m')\,dm', \end{aligned} \tag{2.52}$$

The left hand side of (2.52) can be transformed in

$$\begin{aligned} \int_{m_k}^{m_{k+1}} \frac{\partial n(m,t)}{\partial t} m^l(m,t)\,dm = \int_{m_k}^{m_{k+1}} \frac{\partial}{\partial t}[n(m,t)m^l(m,t)]\,dm \\ - \int_{m_k}^{m_{k+1}} n(m,t)\frac{\partial m^l(m,t)}{\partial t}\,dm, \end{aligned} \tag{2.53}$$

with the first term on the right hand side of (2.53) representing the first moment relatively to species l

$$\int_{m_k}^{m_{k+1}} \frac{\partial}{\partial t}[n(m,t)m^l(m,t)]\,dm = \frac{\partial}{\partial t}\int_{m_k}^{m_{k+1}} n(m,t)m^l(m,t)\,dm = \dot{M}_k^l. \tag{2.54}$$

The material derivative is now introduced

$$\frac{dm^l(m,t)}{dt} = \frac{\partial m^l(m,t)}{\partial m}\frac{dm}{dt} + \frac{\partial m^l(m,t)}{\partial t}. \tag{2.55}$$

Since no condensation process is acting, the partial derivative of species $m^l(m,t)$ to m vanish and consequently $\dfrac{\partial m^l(m,t)}{\partial t} = 0$. That nullify the second term on the right

hand side of (2.50) and consequently, an expression similar to the one component form (2.38) is obtained

$$\begin{aligned}\dot{M}_k = &\frac{1}{2}\int_{m_k}^{m_{k+1}} m^l(m,t)\,dm \int_0^m n(m-m')K(m-m',m')n(m')\,dm' \\ &- \int_{m_k}^{m_{k+1}} m^l(m,t)n(m)\,dm \int_0^\infty n(m')K(m,m')\,dm' \ ,\end{aligned} \tag{2.56}$$

Following the same resolution steps as done for the one component system and inserting the relation $m^l(u+v) = m^l(u) + m^l(v)$ (which means that any species mass fraction $m^l(u+v)$ is the gain product of the interaction of mass fractions $m^l(u)$ and $m^l(v)$) one gets the multicomponent form similarly to (2.47)

$$\begin{aligned}I = &\sum_i^k \sum_j^k \frac{1}{2}\int_{m_i}^{m_{i+1}} \int_{m_j}^{m_{j+1}} \theta(m_k, m_{k+1}, u, v)(m^l(u) + m^l(v))(u+v)\tilde{K_{ij}} n_i(u)n_j(v)dudv \\ &- \sum_i^k \int_{m_k}^{m_{k+1}} \int_{m_i}^{m_{i+1}} \theta(m_{k+1}, \infty, u, v)m^l(v)(u+v)\tilde{K_{ij}} n_i(u)n_j(v)dudv \\ &+ \sum_i^k \int_{m_k}^{m_{k+1}} \int_{m_i}^{m_{i+1}} \theta(m_k, m_{k+1}, u, v)m^l(u)(u+v)\tilde{K_{ij}} n_i(u)n_j(v)dudv \\ &- \frac{1}{2}\int_{m_k}^{m_{k+1}} \int_{m_k}^{m_{k+1}} \theta(m_{k+1}, \infty, u, v)(m^l(u) + m^l(v))(u+v)\tilde{K_{ij}} n_i(u)n_j(v)dudv \\ &- \sum_{i=k+1}^K \int_{m_k}^{m_{k+1}} \int_{m_i}^{m_{i+1}} m^l(v)(u+v)\tilde{K_{ij}} n_i(u)n_j(v)dudv\end{aligned} \tag{2.57}$$

By definition the mass fraction of any species in a particle of mass m discretized in a section k is

$$m_k^l(m,t) = \xi_k^l(t)\, m_k, \ with\ \xi_k^l(t) = \frac{M_k^l}{M_k}.$$

Introducing the last expression and (2.22) in (2.57), the right hand side can then be written similarly to the one component system as a bilinear function in N and M. The coefficients of this bilinear form depend only on the discretized mass space.

2.6.3 Application and results

The previous ODEs systems are integrated in time by a first order forward scheme which leads to

$$N(t+\Delta t) = N(t) + \Delta t F^N(N(t), M(t)) \ ,$$

$$M(t+\Delta t) = M(t) + \Delta t F^M(N(t), M(t)) \ .$$

Higher order variants or implicit multistep methods are possible.
The discretized form of the density function distribution $\hat{n}(m)$ implies as one can expect discontinuities at the bin limits. The use of a limiter allows the setting of the slopes a_i so that $\hat{n}(m)$ behaves somewhat smoother, i.e.,

$$n_i(m) = a_i(m - \widehat{m}) + b_i \qquad \text{with} \qquad b_i = N_i \ .$$

In the optic to validate the new scheme, some test were performed using initial data taken from some well accepted available schemes running also applications.
The simulations have been carried out using a bin-sizing factor $p = \sqrt{2}$ and a total number of bins $K = 100$.

First test example (one component model) The first attempt was the use of initial data for the multicomponent model from Trautmann and Wanner (1999). Data are fitted to an exponential function

$$n(m) = N m_0^{-1} \exp[-m/m_0] \tag{2.58}$$

with N, being the initial total number concentration of the particles and m_0, being the mass corresponding to the mode radius of the initial distribution.
For physical and graphical reasons the results are shown using the log-increment mass density function introduced by Berry and Reinhardt (1974), i.e.,

$$g(r) = 3m^2 n(m) \ , \tag{2.59}$$

whereas $g(r)d(lnr)$ is equal to the mass of particles per unit volume of air with radii in $d(lnr)$. The initial spectrum is the combination of three completely separated modes having the same total mass as summarized in Table 2.1. Such a spectrum may be characteristic for the interaction of small haze particles, cloud droplets and rain drops. The hydrodynamical kernel after Long is involved.
During the simulation the two first modes are depleted gradually and vanish rapidly. The third mass mode referring to rain drops increases gradually and is shifted to

Table 2.1: Parameters of the initial aerosol distribution for the first example.

Modes	Mass $[g\,m^{-3}]$	Number $[m^{-3}]$	Radius $[\mu\,m]$
first mode	1	2. e10	2.28
second mode	1	1. e08	13.3
third mode	1	2. e13	610

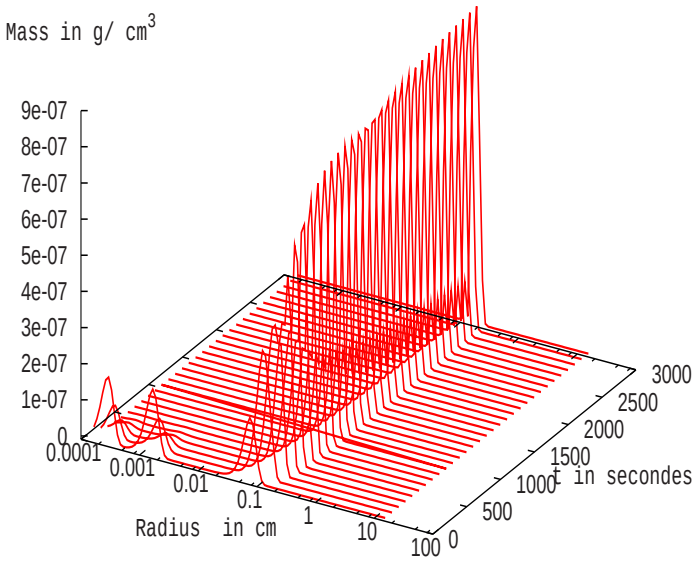

Figure 2.5: Coagulation process with the Long kernel during the first example. Simulation is performed for 3000s. $\Delta t = 1s$.

bigger sizes. This process is very fast. At the end of the simulation we obtain only one narrow mass mode with an average radius of 1200 μm representing the accumulation of the three initial mass modes due to the coagulation process. The same conclusions can be drawn here as the ones in Trautmann and Wanner (1999) (their Fig. 7) namely that even the small particles from the first mode participate in the coagulation process by accumulating on the other modes and that the presence of the precipitation mode (rain drops) accelerates the coagulation drastically (disappearance of the two first modes within 200 s).

Second test example (multicomponent model) In this second example a lognormal function is used for fitting our data due to its well representation of aerosols modes (Whitby and Mc Murry, 1997). With respect to mass, the lognormal distribution assumes the following form

$$\frac{dN}{dm} = \frac{N}{\sqrt{2\pi} m \ln \sigma_{gm}} \exp\left(-\frac{\ln^2(\frac{m}{m_{gN}})}{2\ln^2 \sigma_{gm}}\right) ,$$

with $m_{gN} = \frac{\pi}{6}\rho d_{gN}^3$, $\ln\sigma_{gm} = 3\ln\sigma_g$ and m being a dummy variable representing the particles mass for the bin wise discretization.
The 0-th moment N and the 1-st moment M are related to each other by

$$N = \frac{M(\frac{\pi}{6}\rho)^{-1}}{d_{gN}^3 \exp(\frac{9}{2} ln^2\sigma_g)} ,$$

with, d_{gN} the geometric mean diameter, σ_g the geometric standard deviation of the distribution and m_{gN} and σ_{gm} the corresponding modal parameters for the lognormal distribution with respect to mass.
N and M are then calculated for each bin using a trapezoidal scheme.
Table 2.2 presents the initial data used in this test example. They represent a set of aerosol concentrations likely to exist in an automobile tunnel (Jacobson et al. 1994). Mass is in $\mu g.m^{-3}$ and D_{gv} in μm.The simulations have been carried out using the Brownian kernel after Fuchs.

Fig. 2.6 illustrates the initial volume distribution of the different internally mixed aerosol types involved in the system. The comparison of the DGM scheme results with the ones given by the semi-implicit model of Jacobson et al. (1994) using Fuchs interpolation formula for the kernel shows a good agreement for the total volume distribution of all externally and internally mixed components (Fig. 2.7 a, c). The coagulation concerns only the particles smaller than $1\,\mu m$ and the left part of the curve is consequently shifted to bigger sizes. The general behavior of the volume distribution of the sum of all particles is similar to the evolution due to auto-conversion of a single particle type having the same total distribution. The evolution of every individual particle type after the whole simulation time using the DGM plotted in Fig. 2.7 (b) shows that the coagulation of IM types occurs in the submicron ranges, and that no coagulation occurs for particles bigger than 1 μm.
Because we do consider only IM particles, a difference is noticed for the EM particles with the reference results (sulfate and water in EM3 and IM). The externally mixed constituents along the coagulation process become part of the IM ones leading also to creation of newly IM particles which leads to a rather complicated system when all the possible combinations are treated . Due to numerical cost reasons and to the fact that after a sufficiently long coagulation process, most of the EM particles hetero-coagulate to finally become part of the IM particles (Jacobson et al., 1994) we restricted the study to IM particle types. Trautmann et Wanner (1999) used the same simplifications when implementing the present test example for their exponential scheme and their results (their Fig. 8) are in very good agreements with the results shown in Fig. 2.7(a, b). Accordingly, The reliability and numerical accuracy of the DGM method was demonstrated.

Table 2.2: Parameters of the initial distribution of IM and EM aerosols.

	Nuclei mode			Accumulation mode			Coarse mode		
particle	Mass	D_{gv}	σ_g	Mass	D_{gv}	σ_g	Mass	D_{gv}	σ_g
EM1									
EC	67.0	0.107	1.66						
EM2									
OC	47.6	0.136	1.50						
EM3									
Sulfate	0.008	0.04	1.8	0.49	0.32	2.16	0.050	12.3	2.4
Water	0.012	0.04	1.8	0.74	0.32	2.16	0.075	12.3	2.4
IM									
Sulfate	0.072	0.04	1.8	4.43	0.32	2.16	0.450	12.3	2.4
Water	0.100	0.04	1.8	5.00	0.32	2.16	2.000	12.3	2.4
Nitrate	0.003	0.04	1.8	2.00	0.32	2.16	2.500	8.1	2.4

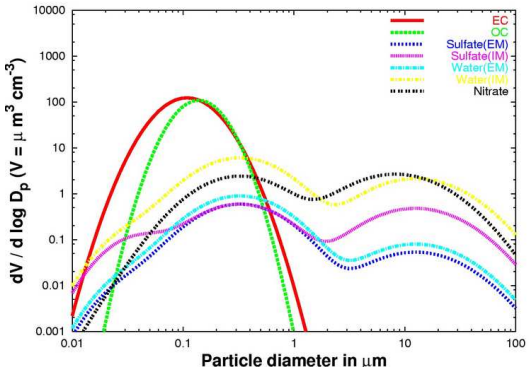

Figure 2.6: Initial volume distribution of the different internally mixed aerosol types.

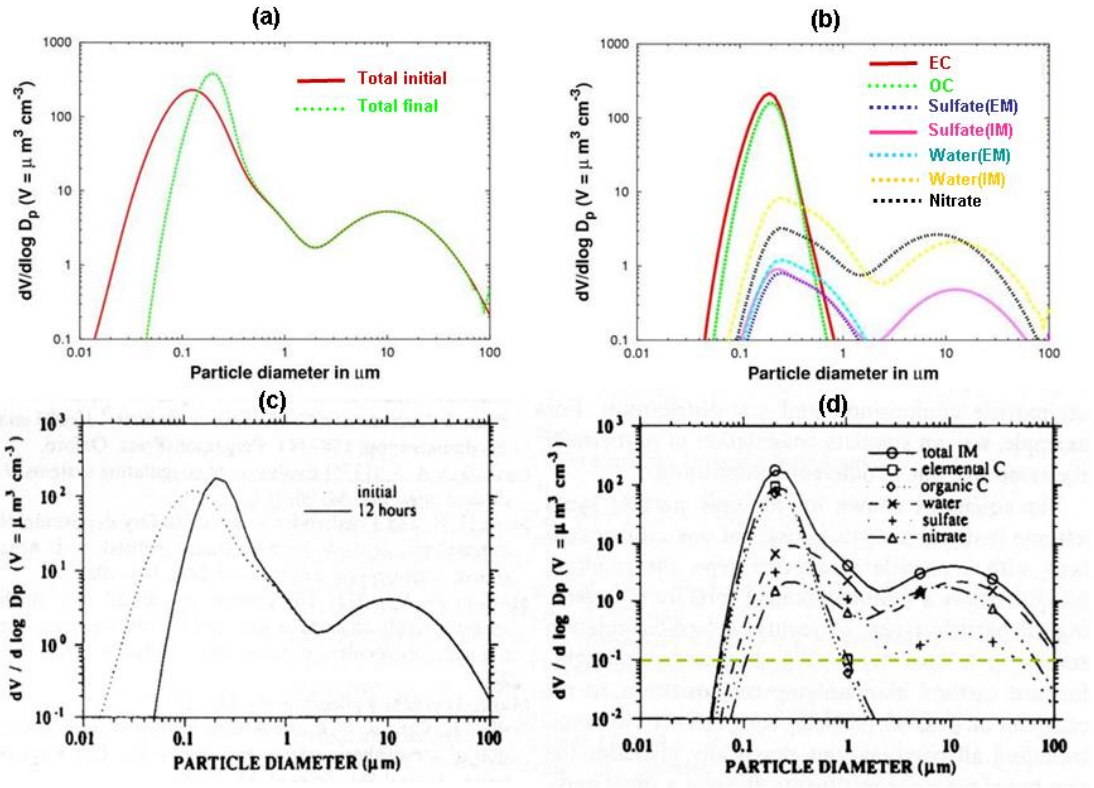

Figure 2.7: Volume distribution of the sum of all internally mixed aerosol types after 12 h of coagulation (a); volume distribution of the different internally mixed aerosol types after 12 h of coagulation (b), $\Delta t = 1s$. The volume distributions in (c) and (d) are the corresponding results from Jacobson et al. (1994) for an EM aerosol populations (their Fig.6 and 9).

Chapter 3

The multiphase chemistry model

3.1 Model formulation

In the real atmosphere, multiphase chemistry closely interacts with microphysical cloud processes. These essential interchange effects have to be taken into consideration also for the development of numerical techniques. The treatment of the multiphase chemistry is achieved for a size-resolved particle/droplet spectrum in a box model (e.g., one "grid cell" of an Eulerian grid model). The particle/droplets are segregated into K classes. This decomposition into classes is based on their droplet size and, eventually, on the amount of scavenged material inside the drops. We assume that the size distribution and all other microphysical parameters are given by a microphysical cloud model. In each of the K droplet classes, N_A aqueous phase species are considered. Some of these aqueous phase species interact with one of the N_G gas phase species. Note that the number of species in the gas phase is not necessarily the same as the number of aqueous species which occur in all droplet classes.

In a box model the multiphase chemical processes can be described by the mass balance equations

$$\frac{dc_{l^*}^G}{dt} = R_{l^*}^G(t, c_1^G, \ldots, c_{N_G}^G) - \kappa_l \sum_k^K L_k \cdot k_t^{kl} \cdot \left[c_{l^*}^G - \frac{m_l^k}{H_l} \right] + \mu \cdot [c_{l^*}^G - c^{G_{ent}}] \tag{3.1}$$

$$\begin{aligned} \frac{d(c_l^k)}{dt} = {} & L^k \cdot R_l^A(t, m_1^k, \ldots, m_{N_A}^k) + \kappa_l \cdot L_k \cdot k_t^{kl} \cdot \left[c_{l^*}^G - \frac{m_l^k}{H_l} \right] \\ & + T(c_l^1, \ldots, c_l^K) + \mu \cdot [c_l^k - c_l^{k_{ent}}], \end{aligned} \tag{3.2}$$

with $l^* = 1, \ldots, N_G$; $l = 1, \ldots, N_A$; $k = 1, \ldots, K$.
L_k denotes the volume fraction $[V_k/V_{box}]$ of the k-th droplet class inside the box volume. The vectors $c^k, k = 1, \ldots, K$, are the mass concentrations related to air

volume of aqueous species in the k-th liquid water fraction. The corresponding aqueous phase concentrations related to liquid water in each class are given by $m^k = c^k/L_k$. The vector c^G stands for the concentrations of the gas phase species. All concentrations are given in moles per cubic meters. The chemical reaction terms are denoted by R^G and R^A. The second term on the right hand side describes the interchange between the gas and aqueous phases. It will be referred to as Henry term in the following. The indicator κ is equal to 1 if the species is soluble. In the other cases, the Henry term will be dropped in both equations. The term T in (3.2) stands for the mass transfer between different particle/droplet classes by microphysical exchange processes of liquid water (e.g., by condensation, coagulation, break up). The time-dependent natural and anthropogenic emissions as well as dry and wet deposition are parameterized in the last terms of the right hand sides using the time dependent entrainment/detrainment rate μ. Additionally in a parcel model, variations in the air density should be considered. These density changes influence especially the gas phase chemistry and the mass transfer. To simplify the model formulation, density variations are neglected in (3.1, 3.2).

3.2 Multiphase chemical processes

The considered chemical reactions are two types: Forward and equilibria reactions. In the following, the whole reaction types in both gas and aqueous phase are presented. The formulation of the different reactions rate types is presented in Appendix A.1.

3.2.1 Forward reaction types in gas and aqueous phase

The main reaction types involve photolysis and temperature dependent reactions. Additionally, some special reactions are considered depending on the used mechanism.

Photolysis: As an example for the gas phase photolysis, the photodissociation of nitrogen dioxide which represents the unique significant source of atomic oxygen for wavelength $\lambda > 300nm$

$$\mathrm{NO_2} + h\nu \rightarrow \mathrm{NO} + \mathrm{O(^3P)} \ ,$$

and in the aqueous phase

$$\mathrm{NO_2^-} + h\nu \rightarrow \mathrm{NO(aq)} + \mathrm{OH(aq)} + \mathrm{OH^-}.$$

Units for the photolysis frequencies are $\mathrm{s^{-1}}$.

Temperature dependent reactions: In the gas phase reaction

$$O_3 + NO \xrightarrow{k} NO_2 + O_2,$$

the contribution of e.g. O_3 and NO_2 species to the mass balance reads

$$\frac{d[O_3]}{dt} = \ldots - k[O_3].[NO] + \ldots \ , \tag{3.3}$$

$$\frac{d[NO_2]}{dt} = \ldots + k[O_3].[NO] + \ldots . \tag{3.4}$$

An example in the aqueous phase is the reaction

$$HSO_3^- + H_2O_2 + H^+ \rightarrow SO_4^{2-} + 2H^+ + H_2O$$

The reaction rate k can take different temperature dependent forms. It can also be constant and the reaction is then temperature independent. In the aqueous phase mechanism CAPRAM (Herrmann et al., 2000) special reactions are introduced which are two types of pH dependent reactions. Appendix A.1 contains the different formulations of all reaction rates.

3.2.2 Dissociation

The chemistry in the aqueous phase differs from the gas phase chemistry by the occurrence of fast dissociation equilibria. This process is treated by modelers using different techniques and assumptions. In the lumping techniques (e.g., Djouad and Sportisse (2002)) the original reacting systems are reduced by defining a set of lumped species and algebraic constraints. These techniques do not always give a "correct" model and the construction of the reduced system is not an easy task, especially, when mixed lumping are involved. In our approach, dissociation is considered as forward and backward reaction defined by the equilibrium and the backward reaction rate. Generally, only the equilibrium rate is known. The determination of the backward rate is the remaining task to complete the description of dissociation reactions. If the backward reaction rate is not available, which is mostly the case, and no analogy is possible, a high value ensuring the equilibrium is taken. The dissociation rates can be temperature dependent or constant. The following reaction illustrates a temperature dependent dissociation and the way it is treated in the model

$$HNO_3(aq) \underset{k_-}{\overset{k_+}{\Longleftrightarrow}} H^+ + NO_3^-$$

The equilibrium constant in the last example is $k_e = \frac{k_+}{k_-}$ and the contribution to the mass balance is

$$\frac{d[HNO_3](aq)}{dt} = \ldots - k_+[HNO_3](aq) + k_-[H^+].[NO_3^-] + \ldots , \tag{3.5}$$

or

$$\frac{d[\mathrm{HNO_3}](\mathrm{aq})}{dt} = \ldots - k_{-}.\big(k_e[\mathrm{HNO_3}](\mathrm{aq}) + [\mathrm{H^+}].[\mathrm{NO_3^-}]+\big)\ldots, \tag{3.6}$$

where the k_e depends on temperature and k_- is constant.
As an example of temperature independent dissociation, the reaction

$$\mathrm{HO_2} \underset{k_-}{\overset{k_+}{\Longleftrightarrow}} \mathrm{O_2^-} + \mathrm{H^+},$$

where k_e and k_- are both constant.
Most of the dissociations include $\mathrm{H^+}$ or $\mathrm{OH^-}$ ions. Therefore the behavior of the system depends very strongly on the underlying pH value. In contrast to other authors (Chaumerliac et al., 2000), the pH value is not prescribed a priori. The H^+ concentration as part of the chemical system is determined initially by the charge balance and then computed for each droplet class dynamically.

3.2.3 Mass transfer

In presence of water droplets, a mass transfer mode is established at the gas-droplet interface. The eventual concentration equilibrium reached by a molecule A between the gas and the liquid phase is described by the Henry´s law, i.e.,

$$A(g) \Longleftrightarrow A(aq)\ ,$$

with

$$\frac{A_a}{A_g} = H_l\ . \tag{3.7}$$

The value H_l denotes the real dimensionless Henry's law coefficient for the l-th species and stands for the constant of equilibrium of mass transfer process at the gas-liquid interface.
The interchange process itself between the gas and liquid phases is specified according to the Schwartz approach (Schwartz, 1986). Mass transport process is seen as being reversible. The mass transfer coefficient

$$k_t^{kl} = \left(\frac{r_k^2}{3D_g} + \frac{4r_k}{3\nu\alpha_l}\right)^{-1} \tag{3.8}$$

depends on the droplet size r_k, the gas diffusion coefficient D_g, the molecular speed ν and the mass accommodation coefficient α_l of the l-th species. The ratio $\frac{r_k^2}{3D_g}$ corresponds to a diffusion time in the gas phase and $\frac{4r_k}{3\alpha_l\nu}$ corresponds to a transfer time through the interface (Fig. 3.1). For small droplets or small accommodation coefficient ($\alpha < 10^{-2}$), the second term is dominant (i.e., the transfer through the

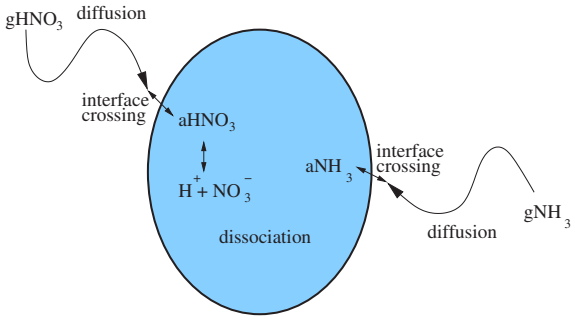

$P_{HNO_{3,surf}} < P_{gHNO_3}$

P_{gHNO_3} is the partial pressure far from the particle.
$P_{HNO_{3,surf}}$ is the particle surface vapor pressure.

Figure 3.1: Schematic representation of mass transfer of volatile species between gas and condensed phase. The two steps described by the accommodation coefficient (diffusion time and interface crossing time) after Schwartz are shown.

interface is less limiting). For nonstationary consideration, a correction has to be applied.

For the mass transfer and the aqueous chemistry, well-diluted droplets are assumed. In fact, the assumption of an ideal solution is not valid especially for non-activated particles and small droplets. The non-ideal behavior can be parameterized by activity coefficients. The influence of activity effects on multiphase chemistry and droplet activation is an important issue being the focus of many studies and models (Zaveri et al., 2005; Pitzer, 1991)

3.2.4 Handling of the chemical mechanism

The handling and computing of the above mentioned reactions and phase transfer in chemical reacting mechanisms is a rather complicated task especially when those mechanisms are very detailed like the CAPRAM family (Fig. 3.1). In our implementation, the chemical reaction systems (gas and aqueous phases, phase transfer according to Schwartz) are given in ASCII data files. The syntax to describe the system is very easy and allows large flexibility (Wolke and Knoth, 2002; Sehili et al., 2005a). Changes within the chemical mechanism or the replacement of the whole

Table 3.1: Characteristics of the used chemical mechanisms.

	number of species			number of reactions					
mechanism	total	gas	aqua	total	gas	Henry	disso	aqua	Reference
INORG	100	80	20	259	237	8	10	4	Sehili et al. (2005a)
BARTH	122	80	42	284	237	14	6	27	Barth et al. (2003)
CAPRAM2.3	162	82	80	508	237	34	27	210	Herrmann et al. (2000)
CAPRAM2.4	220	83	137	653	237	34	54	328	Ervens et al. (2003)
CAPRAM2.4RED	194	83	111	421	237	33	37	114	Ervens et al. (2003)
CAPRAM3.0	492	99	389	1087	261	51	88	687	Herrmann et al. (2005b)

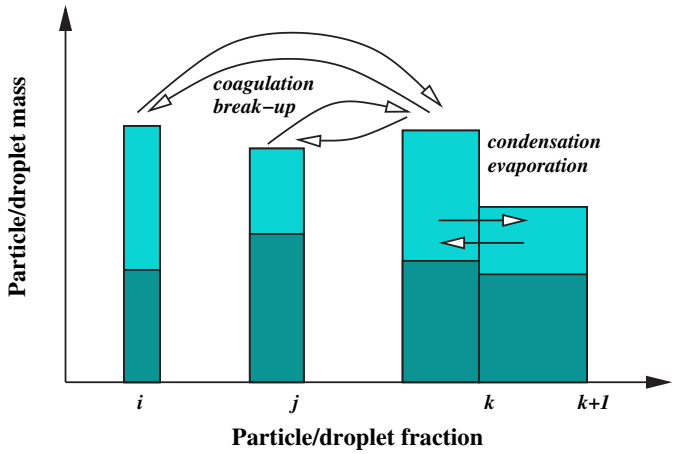

Figure 3.2: Schematic representation of the microphysical fluxes.

chemistry can be performed in a simple and comprehensive way. The preprocessor PreChem is used for the task of reading and interpreting the chemical data. It allows the passage from the symbolic chemical reaction notation to a mathematical one (input data for the multiphase model) and the automatic generation of the parameters needed to build the sparse system (e.g., the Jacobian) while an implicit time integration is considered. PreChem ensures a high flexibility in choosing the reacting mechanism or replacing a part of it. As an example, fragments of the input/output data files are presented in Appendix A.2.
On the other hand, complex multiphase mechanisms although easily handled induce large systems that are numerically expensive. Thus, reduction algorithms are being developed in order to generate automatically reduced reacting mechanisms from condensed ones for specifiable application purposes. In Mauersberger (2005) the new reduction tool ISSA (Iterative Screening and Structure Analysis) is developed and applied to CAPRAM2.4 mechanism.

3.2.5 The microphysical fluxes

The mass fluxes T caused by microphysical exchange processes are linearized in the form

$$T(c_l^1, \ldots, c_l^K) = \sum_{i=1}^{K} \left[T_{ik} c_l^i - T_{ki} c_l^k \right] \tag{3.9}$$

These liquid water fluxes transport the corresponding fractions of all included aqueous phase species into other classes. When two particles coagulate, for instance, they transfer their masses to the resulting particle class which can also grow by condensation to bigger particle class as described in Fig. 3.2. Assuming IM aerosol in each

class, the input and mixing in this class are realized instantly.
In the ODE system (3.1), (3.2), the species within one class are coupled through the chemical reaction system. Furthermore, two types of coupling between different droplet classes can be identified. First, the aqueous phase species within different classes interact directly by the exchange term T. Additionally, they are indirectly coupled via the gas phase by the phase interchange described by the Henry term.

Chapter 4

Coupling

Coupling between the complex multiphase chemistry model and the detailed microphysical one presented above implies the definition of an interface for codes communication. For that, the different kind of variables have to be arranged. The model variables can be grouped as follows
$m = (T, q, L_1 \dots L_K)$ for microphysical variables, $c = (c^G, c^1 \dots c^K)$ for chemical variables and $T = (T_{i\ k})_{i=1\dots K,\ k=1\dots K}$ for mass fluxes generated by microphysical processes. The 'abstract' model formulation is described by

$$\frac{\mathrm{d}m}{\mathrm{d}t} = f_{microphys}(t, m, c) \qquad \text{for microphysics ,} \tag{4.1}$$

$$\frac{\mathrm{d}c}{\mathrm{d}t} = f_{multichem}(t, c, m) \qquad \text{for multiphase chemistry .} \tag{4.2}$$

The two previous equations can be solved numerically by a fully coupled time integration, or by using an *Operator splitting* technique. The last technique allows the possibility to treat sequentially several coupled processes taking place simultaneously and to reduce the size of the system to be inverted. The combination and the order of operator are very important because of the stiffness of the equations.

4.1 The operator splitting technique

Mainly due to limited computing resources, the operator splitting methods became one of the most commonly used techniques in air pollution modeling. These techniques are aimed to integrate different processes involved in the one problem with optimal schemes. In coupled cloud chemistry models, the chemical multiphase reactions are the source of stiffness. Then, implicit numerical schemes are required. The operator splitting technique allows to handle the stiffness of the initial systems (decoupling the fast and slow processes). As one can expect, the solution of the initial problem when the operator splitting method is applied suffers from an additional

lack of accuracy caused by the so-called operator splitting error. The derivation of the splitting error expression or an estimation of its order of magnitude in complex non-linear systems such as in our case is so far not possible (Müller, 2001). Lanser and Verwer (1999) derived a general formulation of the Strang splitting error in the case of pure initial value non-linear time-dependent advection-diffusion-reaction problems. For that, the Lie operator formalism and the BCH (Baker-Campbell-Hausdorff) formula were used. In Sportisse (2000) an analysis for some splitting techniques in the case of linear operators is presented with a focus on stiff problems. For practical use, a systematic investigation of the splitting error for coupled microphysical-multiphase chemical systems is presented in (Müller, 2001).
Let us consider a problem involving several processes of the form

$$\frac{\partial c}{\partial t} = \left(\frac{\partial c}{\partial t}\right)_{process\ 1} + \left(\frac{\partial c}{\partial t}\right)_{process\ 2} + \ldots + \left(\frac{\partial c}{\partial t}\right)_{process\ n} .$$

An example of which is the advection-diffusion-reaction equation which represents the basic theoretical background of the 3D atmospheric dispersion models. For a chemical species i one reads

$$\frac{\partial c_i}{\partial t} + \nabla \cdot (u(x,t)c_i) = \nabla \cdot (K(x,t) \cdot \nabla c_i) + \chi_i(c, T(x,t), t) + S_i(x,t) - R_i(x,t)c_i \ . \quad (4.3)$$

where x and t denote respectively the space and time coordinates, c is the vector of chemical concentrations, $u(x,t)$ the field of wind velocity, $\chi_i(c, T(x,t), t)$ stands for the chemical production of species i at temperature T and $S_i(x,t)$ a source term of species i (i.e., punctual industrial emissions). The removal rate of species i, $R_i(x,t)$ corresponds to wet deposition including phase transfer from the gas phase. $K(x,t)$ is the diffusive coefficient describing atmospheric turbulence. In a linear operator form the last problem and similar problem types are written

$$\frac{\partial c}{\partial t} = P_1 c + P_2 c + \ldots + P_n c \ . \quad (4.4)$$

The exact solution c at the time step $t + \Delta t$ is then

$$c(x, t + \Delta t) = exp\big([P_1 + P_2 + \ldots + P_n]\Delta t\big) c(x,t) \ . \quad (4.5)$$

That represents a fully coupled problem where all processes are simultaneously treated. Numerically, this can be synonym of high computational cost considering that the numerical scheme is not always the optimal one for every process. The other strategy offered by the operator splitting techniques is to transmit the effect

of every process on the next one, i.e.,

$$\begin{aligned} c^1(x,t+\Delta t) &= exp(P_1\Delta t)c(x,t) \\ c^2(x,t+\Delta t) &= exp(P_2\Delta t)c^1(x,t+\Delta t) \\ &\vdots \\ c^n(x,t+\Delta t) &= exp(P_n\Delta t)c^{n-1}(x,t+\Delta t)\ . \end{aligned}$$

Hereafter, we further consider the following abstract initial value problem

$$c'(t) = f(c) = f_1(c) + f_2(c), \qquad c(0) = c_0 \tag{4.6}$$

4.1.1 First order operator splitting

The solution is splitted into two intermediate steps

$$\begin{aligned} C_1^{'} &= f_1(C_1),\ t \in [t_n, t_n + h],\ C_1(t_n) = c_n\ , \\ C_2^{'} &= f_2(C_2),\ t \in [t_n, t_n + h],\ C_2(t_n) = C_1(t_n + h)\ . \end{aligned} \tag{4.7}$$

The approximated solution is then $c_{n+1} = C_2(t_n + h)$

4.1.2 Strang splitting

In this case, the solution is splitted into three intermediate steps

$$\begin{aligned} C_1^{'} &= f_1(C_1),\ t \in [t_n, t_n + \frac{h}{2}],\ C_1(t_n) = c_n\ , \\ C_2^{'} &= f_2(C_2),\ t \in [t_n, t_n + h],\ C_2(t_n) = C_1(t_n + \frac{h}{2})\ , \\ C_3^{'} &= f_1(C_3),\ t \in [t_n + \frac{h}{2}, t_n + h]\ , C_3(t_n) = C_2(t_n + h)\ . \end{aligned} \tag{4.8}$$

The approximated solution is $c_{n+1} = C_3(t_n + h)$.

4.1.3 Source splitting

For practical applications, a third scheme was proposed by Knoth and Wolke (1994) derived form the first-order one. The new feature here is to add a source term representing the mean evolution of the first intermediate step over the time step to the second intermediate step with a non modified initial conditions. The intermediate steps are

$$\begin{aligned} C_1^{'} &= f_1(C_1),\ t \in [t_n, t_n + h],\ C_1(t_n) = c_n\ , \\ C_2^{'} &= f_2(C_2) + \frac{C_1(t_n + h) - C_1(t_n)}{h},\ t \in [t_n, t_n + h],\ C_2(t_n) = c_n\ . \end{aligned} \tag{4.9}$$

The approximated solution is $c_{n+1} = C_2(t_n + h)$.
This scheme is equivalent to an explicit integration of the first operator.

As we saw above, the combination and the order of the operators are very important because of the coexistence of time scales dispersed over several orders of magnitude, i.e., stiff problems. In the case of stiff and nonstiff operators, the last one should be taken for the first intermediate step. The stiff operators need evidently an implicit time integration approach. The scheme represents the inspiring idea to couple the nonstiff microphysical model with the stiff multiphase chemistry one.

The derivation of the local error for linear systems is possible for the three techniques using the Taylor series expansion. Considering the following more simple initial value linear evolution system involving two processes, i.e.,

$$\frac{dc}{dt} = P_1 c + P_2 c, \qquad c(0) = c_0, \qquad c \in \mathbb{R}^d \ . \tag{4.10}$$

The exact solution of the system at $t = h$ reads

$$c_{exct} = exp(P_1 + P_2)hc_0 \ . \tag{4.11}$$

The solution using the first order splitting $P_1 - P_2$ is given by

$$c_{1st} = exp(P_1 h)exp(P_2 h)c_0 \ . \tag{4.12}$$

The local error is then straightforwardly $E_l =$ (4.12) - (4.11) .
A Taylor series expansion of (4.12) up to the second order with respect to time leads to the following second order local error formulation

$$E_l = \frac{P_1 P_2 - P_2 P_1}{2} h^2 c_0 + O(h^3) \ . \tag{4.13}$$

This last vanish completely if P_1 and P_2 commute with one another.
A similar analysis for the Strang splitting case $P_1 - P_2 - P_1$ leads to the solution

$$c_{str} = exp(P_1 \frac{h}{2})exp(P_2 h)exp(P_1 \frac{h}{2})c_0 \ , \tag{4.14}$$

and the local error is then a third order one given by $E_l = O(h^3)$.
In the case of a source splitting scheme $P_1 - P_2$, the solution assumes the form

$$c_{src} = exp(P_2 h)\left[I + \int_0^h exp(-P_2 t)dt \frac{exp(P_1 h) - I}{h}\right]c_0 \ , \tag{4.15}$$

and the second order local error reads

$$E_l = (4.15) - (4.11) = -\frac{P_1 P_2}{2} h^2 c_0 + O(h^3) \ . \tag{4.16}$$

Unfortunately, the analysis of such errors for the nonlinear case like in our present case is quiet difficult and remains beyond the scope of our work. Nevertheless, as said above, a systematic evaluation remains feasible. Sportisse (2000) showed that for a linear stiff case, the error is increasing function with the smallest time scale of the stiff process which is in contradiction with the philosophy motivating the use of operator splitting techniques. In addition, it was also demonstrated that the order of the splitting sequence plays a substantial role. The stiff part of the problem have to be integrated at last in order to reduce the splitting error. In our case, that means first integrating microphysics and then the multiphase chemistry part.

4.2 The coupling strategy

The mass fluxes T and all meteorological parameters needed by the multiphase chemistry are taken over from the microphysical model. For this purpose, a new coupling scheme between microphysical and multiphase chemical models was implemented as described schematically in Figure 4.1. The coupling scheme provides time-interpolated values of the meteorological variables (temperature, water vapor, liquid water content) and generates time-averaged mass fluxes T over the coupling time interval. The changes in the chemical aerosol composition by gas scavenging and the chemical reactions feed back on the microphysical processes (e.g., water condensation growth rates via changes in surface tension and the Raoult term). Therefore, the modified chemical composition of the particle/drop spectrum has to be taken into account by the microphysical model. This feedback is also considered in the coupling scheme (see Fig. 4.1). The two models run separately and exchange information only every coupling time step. Each of the two models uses its own time step control. This approach allows the coupling of the complex multiphase chemistry model with microphysical codes of different types. The exchange of information is organized over well-defined interfaces. The size bin discretization of the multiphase chemistry is taken over from the microphysical model. However, the use of coarser resolutions in the multiphase chemistry computations is possible by averaging the meteorological variables. The mass fluxes of the matrix T are summarized. In the feed back case, the chemical composition of the coarser size bin calculated in multiphase chemistry is transferred to all corresponding microphysical bins. In the framework of SPACCIM simulations, two adiabatic air parcel models with detailed microphysics and interactions between aerosol particles and drops are employed: one with traditional 1D treatment of the microphysics (water mass only) and one with a two-component treatment of the microphysics (water and aerosol

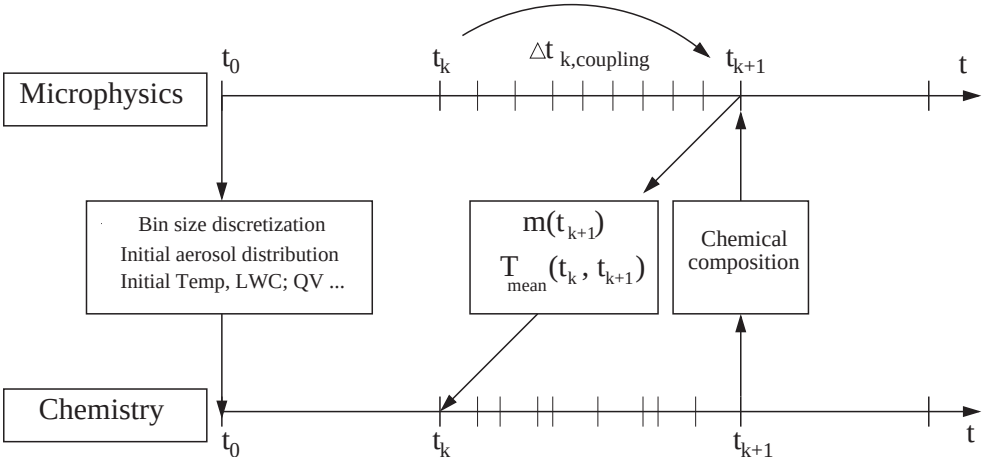

Figure 4.1: Schematic representation of the coupling strategy.

mass) (Simmel and Wurzler, 2005). The latter allows drops of the same size to have different aerosol mass contents and, therefore, different gas scavenging properties (Sehili et al., 2005a). The prognostic microphysical variables for each bin are water mass, total and soluble particulate mass as well as particle number. The model considers the following processes: growth/shrinking and impaction of aerosol particles as well as activation, condensation/evaporation and collision-coalescence of droplets. The activation of droplets is explicitly described in the microphysical model.
A moving bin version of the traditional 1D microphysical model was also coupled, motivated by the predominance of condensation/evaporation processes in some case studies. In the moving bin representation, an initial size distribution based on a fixed grid discretization evolves with bins growing by condensation and decreasing by evaporation independently from each other. This approach is more accurate than a fixed bin discretization when only condensation/evaporation is considered. In this case, the number concentration of particles in a size bin does not changes. The treatment of coagulation/break up in the moving bin approach is possible, but difficult to implement (Jacobson, 1999).

The coupling strategy can be considered as a two stage one. At first, microphysics is coupled to multiphase chemistry by a "modified" first order operator splitting techniques, whereas "modified" means that not the end microphysical values after every coupling time step are delivered to chemistry but time interpolated and mean values as explained above. The mean microphysical fluxes can also be seen as a source term when a similarity is to be made with the source splitting. Furthermore, the system in the multiphase chemistry model is fully coupled.

Chapter 5

Time integration

The abstract formulation of the mass balance equation of the coupled size-resolved multiphase box model represents a system of ordinary differential equations (ODEs) where the right-hand side is non-linear and where the time scales can range over several orders of magnitude (stiff problem). These facts restrict the choose of the numerical solver. Special ones are indeed necessary in order to reduce CPU cost (which is always the case in comprehensive 3-D dispersion models).
In our box model treating microphysical processes and chemistry reactions separately from a numerical point of view, the main burden is computing chemistry every coupling time step. Most of the models addressing multiphase chemistry use either dedicated explicit methods (Hertel et al. (1993), Jay et al. (1997), Verwer (1994), Verwer and Simpson (1995)) or sparse implicit solvers adjusted for exploiting the sparsity in the Jacobian matrix (Jacobson and Turco (1994a), Dabdub and Seinfeld (1995), Wolke and Knoth (2002)). Sandu et al. (1997a) expose a benchmarking of both solver types. The explicit solvers present the disadvantage of being less efficient or do not work when treating gas-liquid phase problems. We present in this chapter two numerical implicit approaches used for solving the system of ODEs. The first method is an implicit multistep method based on differentiation namely the Backward Differentiation Formulas (BDF). The second one is based on a Rosenbrock scheme. The ODE system (3.1, 3.2) can formally be written in the form

$$\dot{c} = f_{chem}(t, c; m) + f_{henry}(t, c; m) + f_{mphys}(t, c; m) \ , \tag{5.1}$$

where c denotes the vector of mass concentrations relating to air volume of the gas phase species and the aqueous species in each particle/drop fraction. The vector m represents the time-dependent microphysical variables which have to be provided simultaneously by the microphysical model. The term f_{chem} stands for the chemical reactions in gas and aqueous phase. The gas-liquid mass transfer term is represented by f_{henry}. The term f_{mphys} stands for mass fluxes between different size bins caused by microphysical processes (condensation/evaporation, coagulation/break up,...).

5.1 The stiffness problematic

As mentioned above, stiffness stands for the coexistence of time scales which are spread over several orders of magnitude in one problem. This is the case in our multiphase system where the reaction rates range over several order of magnitudes. The time scales are directly linked to the eigen values of the Jacobian matrix of the system. We present here a comprehensive example on stiffness taken from Hindmarsh et al. (1987), i.e.,

$$\dot{y} = -[exp(-t)] - 10^2[y - exp(-t)], \quad y(0) = 0 \quad 0 \leq t \leq t_{final}$$

The exact solution of this ODE is

$$y(t) = -exp(-10^2\, t) + exp(-t)$$

The stiffness can be considered as the ratio between the two time scales: $\tau_1 = 10^{-2}$ and $\tau_2 = 1$. After the transition period the **fast** component of the solution is relaxed and the solution is dominated by the **slow** one (Fig. 5.1). Though, the use of the smallest time scale is necessary to ensure convergence. From a numerical point of view, a system is said to be stiff for a given numerical scheme when the integration time step is limited by stability and not precision issues.

For a huge ODE system dimension, the stiff ODE solvers based on standard numerical algebra routines are not feasible. As a consequence, special stiff chemistry time integration techniques have been developed. Both explicit and implicit methods are used. Among the most popular dedicated explicit techniques we cite the Quasi Steady State Approximation QSSA , the Euler Backward Iterative EBI and the variable step size solver TWOSTEP. A detailed description of the three method is

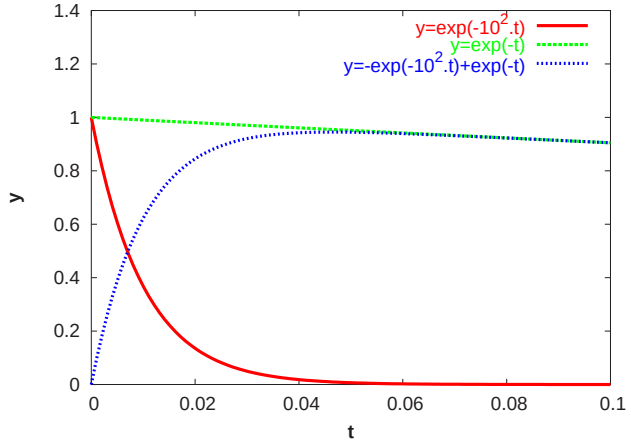

Figure 5.1: Solution of the problem emphasizing the stiffness.

available in Verwer et al. (1998a). Unfortunately, the explicit techniques are used only for gas phase problems and are not efficient or do not work for multiphase chemistry problems. The implicit solvers are more efficient and better appropriated when treating multiphase chemistry systems and some of them constitute established frameworks (e.g., the Rosenbrock family) . Two implicit numerical approaches will be detailed in the following.

5.2 The BDF scheme

In contrast to the multistep formulas based on numerical integration like for instance the Adams methods, the underlying idea of the multistep BDF formulas is the numerical differentiation of a given function. These formulas are widely used for the integration of stiff differential equations. When assumed that the approximations $c_{n-k+1}, \ldots, c_n$ to the exact solution of (5.1) are known, the derivation of a formula for c_{n+1} needs the consideration of a polynomial $q(t)$ which interpolates the values $\{(t_i, c_i)|i = n-k+1, \ldots, n+1\}$.

The implicit formulas of the BDF scheme reads (Hairer and Wanner, 1991)

$$\sum_{j=0}^{k} \frac{1}{j} \bigtriangledown^j c_{n+1} = h f_{n+1} \ , \tag{5.2}$$

where h is the time step and $\bigtriangledown^j$ represents the backward differences

$$\bigtriangledown^0 c_n = c_n, \qquad \bigtriangledown^{j+1} c_n = \bigtriangledown^j c_n - \bigtriangledown^j c_{n-1}$$

The BDF scheme is used in the present work in its fifth order. We give in the following the detailed form until the fifth order of the implicit BDF scheme

$$\begin{aligned}
k = 1: &\ c_{n+1} - c_n = h f_{n+1} \\
k = 2: &\ \frac{3}{2} c_{n+1} - 2c_n + \frac{1}{2} c_{n-1} = h f_{n+1} \\
k = 3: &\ \frac{11}{6} c_{n+1} - 3c_n + \frac{3}{2} c_{n-1} - \frac{1}{3} c_{n-2} = h f_{n+1} \\
k = 4: &\ \frac{25}{12} c_{n+1} - 4c_n + 3c_{n-1} - \frac{4}{3} c_{n-2} + \frac{1}{4} c_{n-3} = h f_{n+1} \\
k = 5: &\ \frac{137}{60} c_{n+1} - 5c_n + 5c_{n-1} - \frac{10}{3} c_{n-2} + \frac{5}{4} c_{n-3} - \frac{1}{5} c_{n-4} = h f_{n+1}
\end{aligned}$$

Accordingly, the use of the BDF implicit multistep method implies the solution of a non-linear functional of the form

$$F(c_{n+1}) = c_{n+1} - C^n - \beta \Delta t_n f(t_{n+1}, c_{n+1}) = 0, \tag{5.3}$$

where c_{n+1} is the solution vector, $\beta > 0$ a parameter of the integration method which depends on the order of the BDF method and C^n a linear combination of c values at time steps $t_n, t_{n-1} \ldots$.
The previous problem is solved by a Newton-like iteration.

$$f(t_{n+1}, c^{n+1}) = f(t_n, c^n) + \frac{\partial f}{\partial c}(c^{n+1} - c^n). \tag{5.4}$$

The entity $\dfrac{\partial f}{\partial c}$ is approximated by the Jacobian J which is not evaluated in every time step.
Equation (5.3) reduce to a linear system of the form

$$(I - \beta \Delta t \ J)\Delta c = b \ , \tag{5.5}$$

with I standing for the idendity matrix and Δt representing the time step size. The right hand side reads

$$b = c^n - C^n - \beta \Delta t f(t_n, c^n) \ . \tag{5.6}$$

The ordinary differential equations (ODE) system (3.1, 3.2) is integrated in an implicit and coupled manner by a higher order Backward Differential Formula (BDF) method. For this part a modification of the code LSODE (Hindmarsh, 1983) with special linear system solvers is used. The time step control and order control are the same as in the original LSODE code.

5.3 The approximate matrix factorization

An efficient solution of the linear system (5.5) is only practicable by applying sparse techniques utilizing the properties of the Jacobian (e.g., sparsity, block structure, different types of coupling). In atmospheric gas phase chemistry, the sparse linear system (5.5) can be solved by linear Gauss-Seidel iterations (Knoth and Wolke, 1995). Unfortunately, for aqueous chemistry mechanisms the Gauss-Seidel iteration converges only slowly or even fails (Wolke and Knoth, 2000).

The Jacobian structure of the right hand side of the multiphase system (3.1, 3.2) is given in Fig. 5.2. The blue blocks in the diagonal are the Jacobians of the gas phase and aqueous phase reaction terms, respectively. In our example, the upper left block stems from the gas phase. The other two diagonal blocks coming from the aqueous phase chemistry have the same sparse structure. The green left and upper boundary blocks represent the phase interchange according to Schwartz (1986). The structure of the Jacobian J^C including the multiphase chemistry as well as the phase

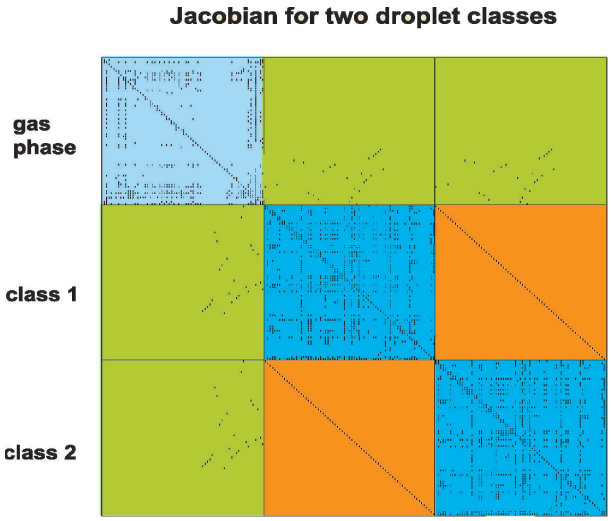

Figure 5.2: Sparse structure of Jacobian for CAPRAM2.3 and two droplet classes.

interchange has the form

$$\mathbf{J^C} = \begin{pmatrix} G & X_1^T & X_2^T & \cdots & X_{K-1}^T & X_K^T \\ Y_1 & A_1 & 0 & \cdots & 0 & 0 \\ Y_2 & 0 & A_2 & \cdots & 0 & 0 \\ & & & \ddots & & \\ Y_{K-1} & 0 & 0 & \cdots & A_{K-1} & 0 \\ Y_K & 0 & 0 & \cdots & 0 & A_K \end{pmatrix},$$

The matrices $G \in \mathrm{R}^{N_G \times N_G}$ and $A_i \in \mathrm{R}^{N_A \times N_A}$ denote the Jacobian of the gas phase and aqueous phase chemistry, respectively. The matrices $Y_k, X_k \in \mathrm{R}^{N_A \times N_G}$ as the Jacobians for the Henry term f^{Hen} contain only N_H non-zero entries.
The orange diagonal matrices include the coupling terms resulting from the mass transfer between the droplet classes and is represented by the Jacobian J^P

$$\mathbf{J^P} = \begin{pmatrix} 0 & 0 & 0 & \cdots & 0 & 0 \\ 0 & 0 & T_{21} & \cdots & T_{K-1,1} & T_{K,1} \\ 0 & T_{12} & 0 & \cdots & T_{K-1,2} & T_{K,2} \\ & & & \ddots & & \\ 0 & T_{1,K-1} & T_{2,K-1} & \cdots & 0 & T_{K,K-1} \\ 0 & T_{1,K} & T_{2,K} & \cdots & T_{K-1,K} & 0 \end{pmatrix}.$$

The diagonal matrices $T_{i\,j}$ contain the mass flux from the i-th to j-th fraction on the diagonal.
In the implementation, the sparse block matrices are generated explicitly and stored in a sparse form. Consequently, a new sparse factorization is performed only when the Jacobian J has to be newly approximated by a Newton iteration. This occurs either if the convergence is slow or if a fixed number of time steps is reached. The

matrix $(I - \beta\Delta t\ J)$ is rather large and the benefit of the sparsity would be largely lost when system (5.5) is solved by a full LU factorization. This is synonym of an increase of the numerical costs. Furthermore, this approach leads to large "fill-in" when the number of droplets classes increases. This is due mainly to entries from J^{TFrac}. The "fill-in" represents the ratio between the number of non-zero in the LU decomposition and the corresponding Jacobian. A better way to avoid the expensive full LU decomposition is to utilize an Approximate Matrix Factorization (AMF), where the splitting between the multiphase chemistry part and the part from microphysical exchange processes is performed at the linear algebra level (Verwer et al., 1999; Wolke and Knoth, 2000). The idea is to approximate the matrix $(I-\beta\Delta t\ J)$ by

$$(I - \beta\Delta t\ J) \approx (I - \beta\Delta t\ J^P)(I - \beta\Delta t\ J^C) = (I - \beta\Delta t\ J) + \beta^2\Delta t^2 J^P J^C\ , \quad (5.7)$$

where $J = J^P + J^C$. Then the linear system (5.5) can be solved by two sequential linear system solutions, i.e.,

$$(I - \beta\Delta t\ J^P)b^* = b\ , \quad (5.8)$$

$$(I - \beta\Delta t\ J^C)\Delta c = b^*\ . \quad (5.9)$$

Additionally to (5.7), two alternative matrix approximations are tested

$$(I - \beta\Delta t J) \approx (I - \beta\Delta t J^C)(I - \beta\Delta t J^P) = (I - \beta\Delta t\ J) + \beta^2\Delta t^2 J^C J^P\ , \quad (5.10)$$

$$(I - \beta\Delta t J) \approx (I - \beta\Delta t J^C) \qquad = (I - \beta\Delta t\ J) + \beta\Delta t J^P\ . \quad (5.11)$$

This is inspired by the discussion of the influence of the splitting sequence and the quality of the Jacobian approximation on the accuracy, e.g., in Verwer and Sportisse (1998b) and Wolke and Knoth (2000). In the approach (5.11), $J^P \approx 0$ and only the sparse system from the multiphase chemistry has to be solved. The approximation error of the approaches (5.7) and (5.10) is analyzed in the following. The AMF formulation gives an $O(\Delta t^2)$ approximation to (5.5) with the error in the form

$$\mathbf{J^C J^P} = \begin{pmatrix} 0 & \sum\limits_{i\neq 1}^{K} X_i^T T_{1,i} & \cdots & \sum\limits_{i\neq K-1}^{K} X_i^T T_{K-1,i} & \sum\limits_{i\neq K}^{K} X_i^T T_{K,i} \\ 0 & 0 & \cdots & A_1 T_{K-1,1} & A_1 T_{K,1} \\ & & \ddots & & \\ 0 & A_{K-1}T_{1,K-1} & \cdots & 0 & A_{K-1}T_{K,K-1} \\ 0 & A_K T_{1,K} & \cdots & A_K T_{K-1,K} & 0 \end{pmatrix}\ , \quad (5.12)$$

$$\mathbf{J^P J^C} = \begin{pmatrix} 0 & 0 & \cdots & 0 & 0 \\ \sum\limits_{i\neq 1}^{K} T_{i,1}Y_i & 0 & \cdots & T_{K-1,1}A_{K-1} & T_{K,1}A_K \\ & & \ddots & & \\ \sum\limits_{i\neq K-1}^{K} T_{i,K-1}Y_i & T_{1,K-1}A_1 & \cdots & 0 & T_{K,K-1}A_K \\ \sum\limits_{i\neq K}^{K} T_{i,K}Y_i & T_{1,K}A_1 & \cdots & T_{K-1,K}A_{K-1} & 0 \end{pmatrix}\ . \quad (5.13)$$

Considering the structure of (5.12) and (5.13), the following remarks can be made In (5.13), all elements of the first row are zero and, therefore, the gas phase is exactly calculated in AMF (5.7). When only condensation and coagulation are involved, that means $T_{ij} = 0$ for $i \geq j$, the matrix J^P is lower triangular. It becomes lower bidiagonal when only condensation is present. This is mainly the case during cumulus cloud type. This constellation offers the possibility for an exact solution of (5.5).

For a linear liquid water transfer term T, the linear system (5.8) is resolved into N_A non-coupled K-dimensional subsystems

$$(I - \beta \Delta t \, \widehat{T}) b_l^* = b_l \ , \qquad l = 1, \ldots, N_A$$

with b_l^*, $b_l \in R^K$ being the vectors for the lth aqueous phase species and $\widehat{T} \in R^{K \times K}$ reading

$$\widehat{T} = \begin{cases} -\sum_{i \neq k} T_{ik} & \text{if } i = k, \\ T_{ik} & \text{if } i \neq k. \end{cases} \tag{5.14}$$

That means, each diagonal element in $\widehat{T}$ is set equal to the sum of the off-diagonal elements of its column taken with the opposite sign.
These linear subsystems are solved by a full LU decomposition without pivoting. The coefficient matrix is the same for all subsystems. Consequently, only one LU decomposition is required. Note that the decoupling into the N_A subsystems is also valid for a nonlinear term T. But the coefficient matrix can be dependent on the considered species in this case.

5.4 Direct sparse solver

The sparse linear system (5.9) is solved by a sparse LU decomposition with diagonal pivoting. An optimal order of the pivot elements to avoid fill-in is determined by a diagonal Meis-Markowitz strategy, e.g., Sandu et al. (1996). To improve this usual strategy two additional requirements are introduced:

1. All gas phase species which occur in Henry terms are placed at the end of the pivot order.

2. In the modified strategy, the vector $\mathbf{c_l} \in R^K$ of the l-th aqueous phase concentration is understood as a "supernode". If one of these species is picked up as pivot element the whole sub-matrix is treated as the pivot. After the reordering all species of the vector appear one after another in the order.

Additionally, a Schur complement implementation for the solution of the system (5.9) is investigated in Wolke and Knoth (2002). We present here the basic theory

behind this approach.
The system (5.9) has the explicit form

$$\begin{pmatrix} G & X_1^T & X_2^T & \cdots & X_{K-1}^T & X_K^T \\ Y_1 & A_1 & 0 & \cdots & 0 & 0 \\ Y_2 & 0 & A_2 & \cdots & 0 & 0 \\ & & & \ddots & & \\ Y_{K-1} & 0 & 0 & \cdots & A_{K-1} & 0 \\ Y_K & 0 & 0 & \cdots & 0 & A_K \end{pmatrix} \begin{pmatrix} g \\ a_1 \\ a_2 \\ \cdots \\ a_{K-1} \\ a_K \end{pmatrix} = \begin{pmatrix} b_G \\ b_1 \\ b_2 \\ \cdots \\ b_{K-1} \\ b_K \end{pmatrix}$$

where the notation $g = c^G$ for gas phase, $a_1, \ldots, a_K$ for the aqueous phase concentrations and $b_G, b_1, \ldots, b_K$ for the corresponding vectors in the right hand side.
The solution of the system is then given by

$$g = \left(G - \sum_{k=1}^{K} X_k^T A_k^{-1} Y_k \right)^{-1} \left(b_G - \sum_{k=1}^{K} X_k^T A_k^{-1} b_k \right) , \tag{5.15}$$

$$a_k = A_k^{-1}(b_k - Y_k g), \ k = 1, \cdots, K \ . \tag{5.16}$$

The benefit relative to the use of an approximate matrix factorization with Meis-Markowitz strategy and Schur complement approach in comparison to the full LU factorization is presented in Wolke and Knoth (2002).

5.5 The second order Rosenbrock method

Among the methods which already give satisfactory results for stiff problems, Rosenbrock methods have the advantage of being simple to understand and to implement. For moderate accuracies ($\epsilon \lesssim 10^{-4} - 10^{-5}$ in the error criterion) and small systems, they are competitive with the more complicated algorithms. For the integration of the 0-D box model, we propose here a second order non-autonomous Rosenbrock method called ROS2. Rosenbrock methods belong to a class of methods which try to avoid nonlinear systems and replace them by a sequence of linear systems.

In this section we consider the box model

$$\dot{c} = f(c) \tag{5.17}$$

where c denotes the vector of chemical concentration of gas and aqueous species involved in the system. The family of two-stage Rosenbrock methods has the following formulation

$$c_{n+1} = c_n + \sum_{i=1}^{2} b_i k_i \ , \tag{5.18}$$

with

$$k_i = \tau f(t_n + \alpha_i \tau, c_n + \sum_{j=1}^{i-1} \alpha_{ij} k_j) + \tau J \sum_{j=1}^{i} \gamma_{ij} k_j + \gamma_i \tau^2 \frac{\partial f}{\partial t} \ , \tag{5.19}$$

and

$$\alpha_i = \sum_{j=1}^{i-1} \alpha_{ij} \ , \quad \gamma_i = \sum_{j=1}^{i} \gamma_{ij} \ ,$$

where $c_n \approx c(t)$ at $t = t_n$, $\tau = t_{n+1} - t_n$ is the step size, and $J = \dfrac{\partial f(t_n, c_n)}{\partial c_n}$ the Jacobian matrix. Consequently, two linear systems are solved using the same Jacobian. The conditions on the free parameters which ensure that the method is second-order and consistent for any J, i.e., the local error satisfying

$$c(t + \tau) - c_{n+1} = O(\tau^3)$$

are

$$b_1 = 1 - b_2, \ \gamma_{21} = -\gamma / b_2, \ \alpha_{21} = \frac{1}{(2b_2)} \ ,$$

where $b_2 \neq 0$ and γ representing the really free parameters for this order. To achieve a L-stability of the method, the fellowing setting of the free parameters are taken:

$$\gamma = 1 + \frac{1}{\sqrt{2}}, \ \gamma_1 = \gamma_{11} = \gamma, \ \gamma_{21} = -2\gamma, \ \gamma_{22} = \gamma \ ,$$

$$\alpha_1 = 0, \ \alpha_2 = \alpha_{21} = 1, \ b_1 = b_2 = \frac{1}{2} \ .$$

The two linearization steps have then the forms

$$k_1 = \tau f(t_n, c_n) + \tau J \gamma k_1 + \gamma \tau^2 \frac{\partial f}{\partial t} \ , \tag{5.20}$$

$$k_2 = \tau f(t_n + \tau, c_n + k_1) + \tau J(\gamma k_2 - 2\gamma k_1) - \gamma \tau^2 \frac{\partial f}{\partial t} \ . \tag{5.21}$$

Redefining k_2 by $k_2 - k_1$, The nonautonoumous ROS2 scheme reads

$$c_{n+1} = c_n + \frac{3}{2} k_1 + \frac{1}{2} k_2 \ , \tag{5.22}$$

$$(I - \gamma \tau J) k_1 = \tau f(t_n, c_n) + \gamma \tau^2 \frac{\partial f}{\partial t} \ , \tag{5.23}$$

$$(I - \gamma \tau J) k_2 = \tau f(t_n + \tau, c_n + k_1) - 2k_1 - \gamma \tau^2 \frac{\partial f}{\partial t} \ . \tag{5.24}$$

The non-autonomous term $\gamma \tau^2 \dfrac{\partial f}{\partial t}$ is non zero for time dependent liquid water content or during photolytic activity. It can be computed using a finite difference

method.
One advantage of the ROS2 method is the possibility offered to calculate the local error by comparing the two orders of the scheme and consequently, the implementation of the time step control.
The two orders of the scheme are

$$c_{n+1}^{(I)} = c_n + k_1 \ , \tag{5.25}$$

$$c_{n+1}^{(II)} = c_n + \frac{3}{2}k_1 + \frac{1}{2}k_2 \ . \tag{5.26}$$

Straightforwardly, one get the estimated local error

$$err = c_{n+1}^{(II)} - c_{n+1}^{(I)} = \frac{1}{2}k_1 + \frac{1}{2}k_2 \ . \tag{5.27}$$

Chapter 6

Robustness, sensitivity and numerical efficiency

The run control parameters are introduced in a script file according to the considered scenario allowing high flexibility. The run start by performing the initialization for microphysics. The size resolved initial aerosol number and mass distribution including the ratio of soluble material in each section is calculated. The initial meterological variables are initialized. The microphysical simulation is performed for a short period in order to bring the system in equilibrium and then resumed for a coupling time step. The multiphase chemistry simulation follows including the first call of the solver. The sensitivity of the coupled model to some relevant control parameters as well as a numerical efficiency study are presented.

6.1 Test scenarios

Simulations for two different scenarios are carried out. The first one called RISING is described schematically in Fig. 6.1. It was inspired by Kreidenweis et al. (2003) and simulates an air parcel lifted adiabatically at 0.5 $\mathrm{m\,s^{-1}}$ from 98 m below cloud base up to 1200 m above cloud base. The initial dry aerosol number size distribution consists of two lognormal modes, covering the Aitken and the accumulation size range. The initial gas phase concentration and aerosol parameters and composition is given in appendix B.2. In the present test scenario, aerosol composition is represented in appendix B.2 by the second mode. Two modes having different aerosols composition are mixed according to the second mode only. This mode is characterized by a high soluble part. The air parcel start location is 45^oN and 600 m altitude for summer solstice at 9.00 AM. The second scenario described schematically in Fig. 6.2 simulates event E I of the orographic cloud experiment FEBUKO that took place in the Thuringian forest in October 2001 (Herrmann et al., 2005a).
The detailed data set of the used FEBUKO scenario is given in appendix B.3. In-

cloud gas phase photolysis rates are decreased using a factor 0.5 due to cloud droplet scattering. In both test cases, the initial aerosol composition is prescribed independently from the used mechanism. All species not participating in the corresponding reaction scheme are considered as "passive", non-reactive tracers. They affect the pH value and are part of the total mass. The initial pH value is determined through the charge balance equation for the initial aerosol and is then computed dynamically throughout the whole simulation time.

6.2 Model setup

The discussion of the chemical issues is not the focus of the present work. For that, We refer to Herrmann et al. (2005a) and Sehili et al. (2005a). The main task here is to investigate some features and parameter setups of SPACCIM from a numerical point of view. This sensitivity study is performed in order to determine "optimal" control parameters without significant loss of accuracy. Due to the availability of measurements, most of the results presented here concern the FEBUKO case. Options and parameters being subject to assessment are the used mechanism, the coupling time step Δt_{cpl}, feedback from microphysics to chemistry, the number of bins NUMFRAC, the solver relative tolerance RTOL and the applied AMF. Furthermore, coarser size bin resolutions in the multiphase chemistry to reduce the computational costs are investigated. In this approach, RESCHEM bins of the microphysical grid are summarized for the chemistry calculations. The FEBUKO default run is carried out with CAPRAM2.4RED, without feedback, NUMFRAC = 66 bins, RESCHEM = 1, a coupling time step $\Delta t_{cpl} = 10$ s, RTOL $= 10^{-5}$ and approximation (5.10) with Meis-Markowitz LU decomposition strategy. The RISING default run uses CAPRAM 2.3,

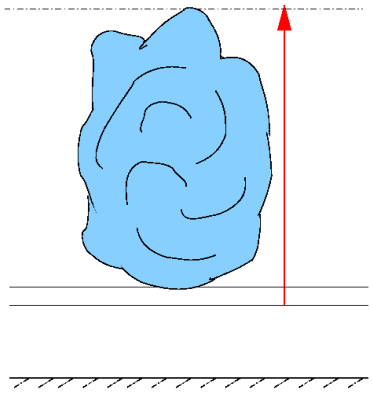

Vertical velocity : 0.5 ms^{-1}
Start altitude : 600 m
Cloud base : +98 m
Cloud top : +1200 m
Meteorological initial values :
Absolute temperature : 285.2 K
Relative humidity : 95%
Pressure : 950 hPa
Temperature (cloud base): 284.2 K
Pressure (cloud base) : 939 hPa
Air density (cloud base): 1.15 kgm^{-3}

Figure 6.1: Schematic description of RISING scenario

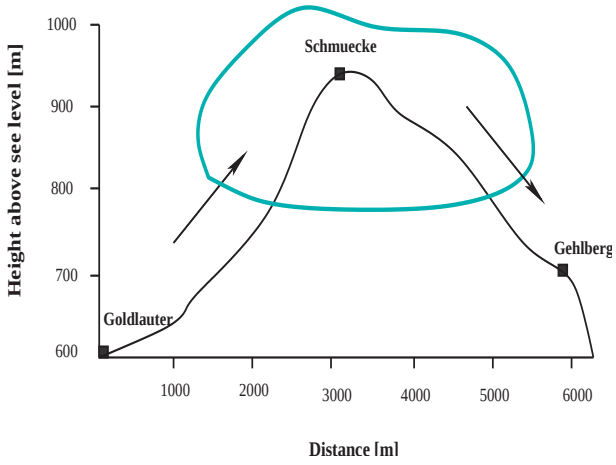

Meteorological data at Goldlauter
Absolute temperature : 281.24 K
Relative humidity : 95.28%
Air density : 1.172 kgm^{-3}
Pressure : 950.19 hPa
Wind speed : 3.00 ms^{-1}

Validation values at Schmuecke :
Absolute temperature : 279.18 K
Air density : 1.131 kgm^{-3}
Pressure : 910.40 hPa
Wind speed : 5.73 ms^{-1}

Figure 6.2: Schematic description of FEBUKO scenario

RTOL $= 10^{-3}$, AMF (5.11) and otherwise the same parameters. The changes are motivated by preliminary simulations. In the moving bin runs, $J^P = 0$ and, therefore, approximation (5.13) is applied.

In the following, the time series plots of aqueous phase variables show summarized masses and averaged concentrations over the whole spectrum. The annotation aORA1 represents the sum of formic acid and formate and aORA2 stands for the sum of acetic acid and acetate. All mass concentrations in the tables are given in mol/m^3. The numerical effort is characterized by the number of required time integration steps *stp*, right hand side evaluations fcn and the CPU time. All runs are carried out on a four processor IBM pSerie workstation with 8 GByte memory.

6.3 Microphysical aspects

As the parcel ascends, the air becomes supersatured and aerosols whose radii exceed the critical ones are considered to be "activated" and continue to grow according to the Koehler equation. During the FEBUKO scenario, the air parcel reaches Schmuecke summit after 710 s, then evaporation proceeds until the final parcel location. In RISING the top of the cloud is reached after 2596 s simulation time. Fig. 6.3 shows

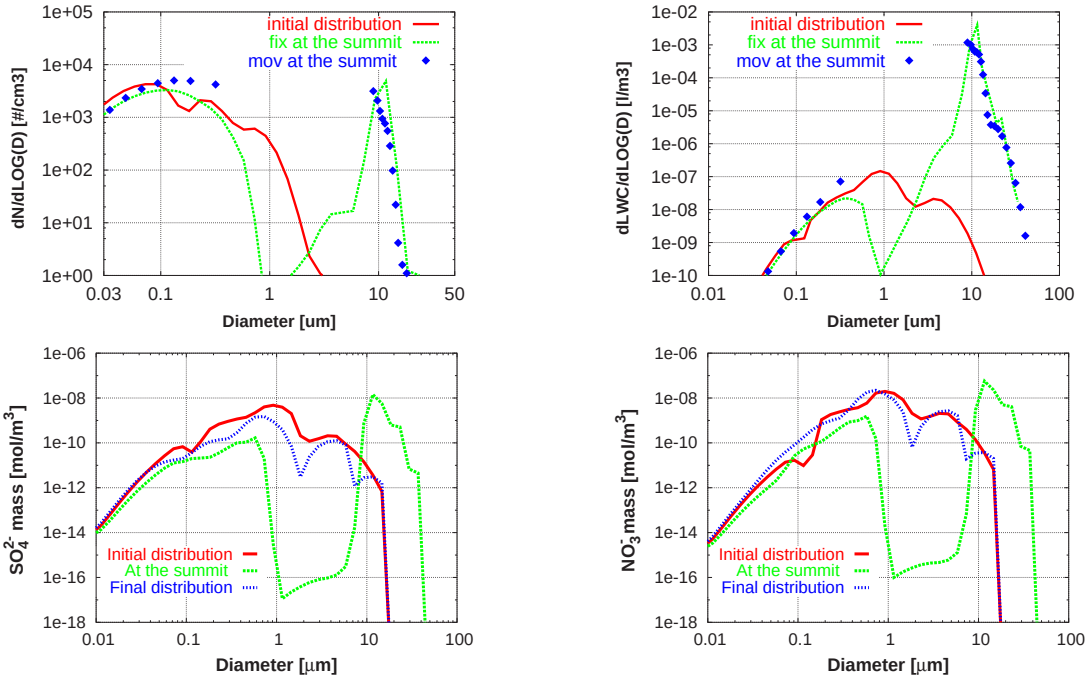

Figure 6.3: Comparison of number and LWC size distributions at Schmücke summit during FEBUKO between 'fixed bin' and 'moving bin' approaches (top). $SO_4{}^{2-}$ and $NO_3{}^-$ mass size distribution during FEBUKO with the fixed bin approach (bottom).

the explicit description of the activation process for the two versions of SPACCIM. In the moving bin discretization, no remapping to the original fixed grid is considered and bins evolve independently from each other. Therefore, spectral variables are plotted using points which are not connected with lines. Between the activated and non-activated part of the spectrum, the microphysical properties can not be resolved. The smaller gap for the fixed bin approach seems to be mainly caused by numerical diffusion. Furthermore, the number distribution of the activated droplets remains within a narrow size range around 10 μm and agrees well with the fixed bin representation. The same remarks can be made for the spectrum of the liquid water content (LWC). The model allows also a spectral description of chemical aqueous species at any time of the simulation. The evolution of mass size distribution of sulfate and nitrate as dissolved material (Fig. 6.3 bottom) is directly influenced by the spectral evolution of the LWC through gas uptake processes. At the end of the evaporation period, aerosols are reprocessed. The differences between the initial and final distributions are due to non-reversible processes.

The total LWC is a key value in model simulations dealing with complex multiphase reacting systems including phase uptake. Fig. 6.4 (left) illustrates the correlation between simulated total LWC and total non-water mass (NWM) during

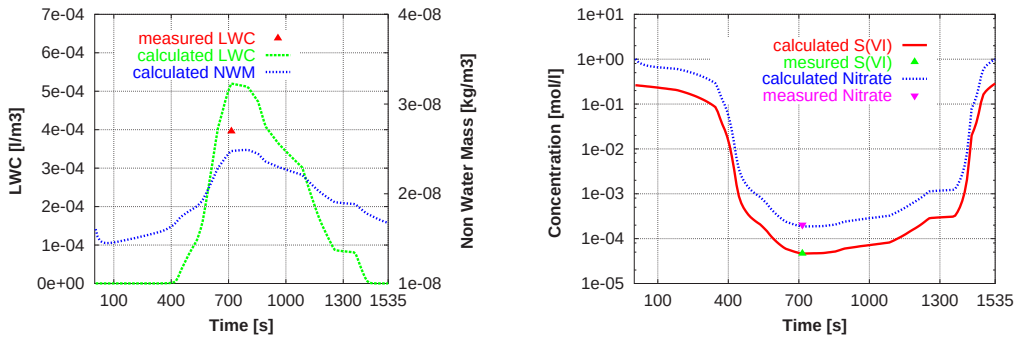

Figure 6.4: Comparison of simulated and measured LWC, NWM, S(VI) and Nitrate during FEBUKO at Schmücke. Simulation are with SPACCIM1D-FIX using CAPRAM2.4RED mechanism.

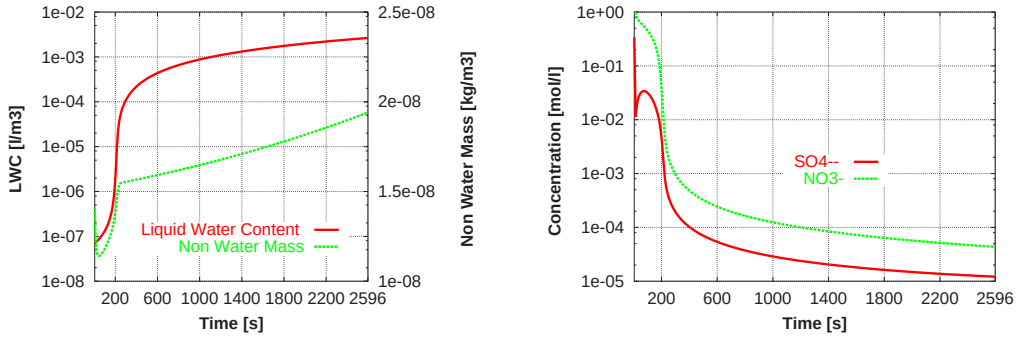

Figure 6.5: Evolution of total LWC and NWM during the RISING scenario. Calculations are performed with SPACCIM1D-FIX using CAPRAM2.3 mechanism.

FEBUKO caused by uptake processes. A punctual comparison with measured LWC on mount Schmuecke shows that about 25 % more LWC is simulated. On the other hand, simulated and measured molalities of S(VI) and nitrate on mount Schmuecke are in good agreement (Fig. 6.4, right). During the rising scenario LWC, NWM and aqueous phase species molalities time series behaves similarly to the upward period of FEBUKO scenario (Fig. 6.5).

6.4 Simulations for different mechanisms

For the tests a more simple inorganic reaction scheme (Sehili et al., 2005a) and four versions of the **C**hemical **A**queous **P**hase **RA**dical **M**echanism (CAPRAM)[1] are used (Herrmann et al., 2000; Ervens et al., 2003; Herrmann et al., 2005b). The gas phase chemistry of all mechanisms is based on the RACM mechanism (Stock-

[1] http://www.tropos.de/CHEMIE/multimod/CAPRAM/capram.html

well et al., 1997). Typical characteristics of the mechanisms are given in Table 3.1. The use of CAPRAM3.0 (where much more organic compounds and reacting path-

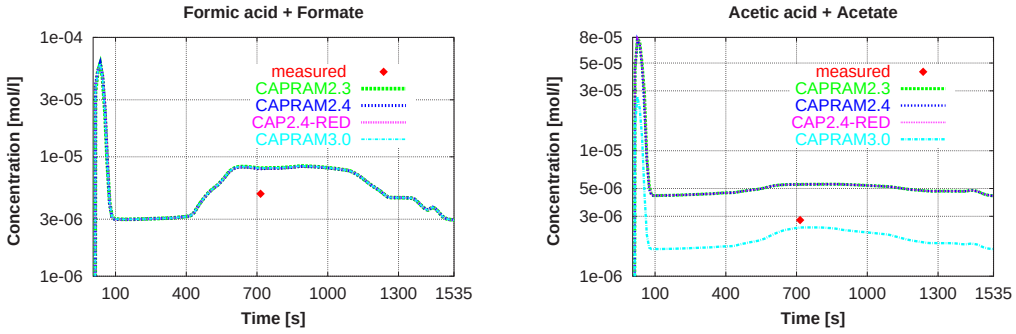

Figure 6.6: Comparison of simulated and measured aORA1 and aORA2 during FEBUKO at Schmücke. Simulations with SPACCIM1D-FIX for the 4 different versions of CAPRAM are plotted.

ways are considered) leads to a better agreement between measured and simulated molalities of some organic species, e.g., aORA2 at mount Schmuecke as shown in Fig. 6.6 (right) and Table 6.1. For other organic species, no significant differences between the mechanisms are observed (Fig. 6.6, left).
Moving to sulfur chemistry (Fig. 6.7), SPACCIM1D-FIX simulates less SO_2 uptake when using the INORG mechanism. Runs with the other mechanisms remain comparable whereas the good agreement between CAPRAM2.4 and CAPRAM3.0 is remarkable. Results with SPACCIM1D-FIX for S(VI) show that INORG and CAPRAM2.3 mechanisms have a similar behavior before activation. Deviations compared to the other mechanisms can be explained by a different equilibrium constant in the Schwartz approach. The initial sharp decrease in S(VI) predicted by the three newer versions of CAPRAM is caused by the imbalance of initial particulate S(VI) and the gas phase applying the modified equilibrium constant. Therefore, S(VI) is released as H_2SO_4 from the particle to the gas phase. Using INORGANIC, less S(VI) is taken up in the particle phase after activation due to the omission of the aqueous phase dissociation pathways of organic acids such as formic acid and, additionally for CAPRAM2.4 or higher versions, dicarbonylic acids such as oxalic acid. These dissociations influence strongly the pH and, consequently, the S(VI) chemistry. The flexibility of SPACCIM concerning the use of various mechanisms offers the possibility to analyze pathways of selected species.

Tables 6.1 and 6.2 summarize the mass concentrations of selected aqueous phase species, the pH values and the computational effort simulated by SPACCIM1D-FIX and SPACCIM1D-MOV. The numbers of steps *stp* and function evaluations fcn are comparable for all mechanisms. However, the CPU times are strongly related to the complexity of the mechanisms. Besides the dimension of the system and the

number of reactions, the types of reaction rates has a large influence on the computing time. For instance, the calculation of a large number of Arrhenius type reaction constants can consume more CPU time than the efficient solution of the sparse linear systems. SPACCIM1D-MOV runs much faster since neither a remapping to original grid nor the computation of microphysical fluxes are required. The resulting deviations from SPACCIM1D-FIX are small (Table 6.2). Hence, SPACCIM1D-MOV constitutes a reliable alternative when only condensation/evaporation are involved.

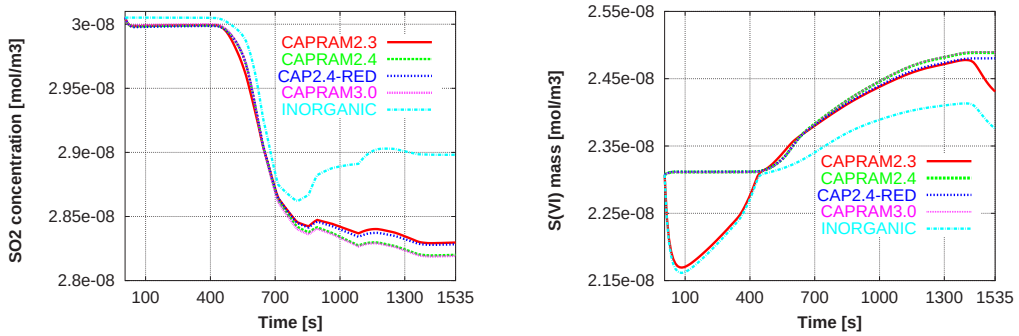

Figure 6.7: Comparison of SO_2 and S(VI) evolution during FEBUKO for 5 different mechanisms with SPACCIM1D-FIX.

Table 6.1: Sensitivity of SPACCIM1D-FIX to different reacting mechanisms during the FEBUKO scenario.

mechanism	S(VI)	NO_3^-	aORA1	aORA2	pH	stp	fcn	CPU [s]
CAPRAM2.3	2.414e-8	9.690e-8	3.650e-9	2.621e-9	4.238	8079	13885	861
CAPRAM2.4	2.417e-8	9.690e-8	3.651e-9	2.618e-9	4.237	8138	14098	1659
CAPRAM2.4RED	2.415e-8	9.690e-8	3.653e-9	2.618e-9	4.238	8336	14308	1412
CAPRAM3.0	2.417e-8	9.691e-8	3.666e-9	1.166e-9	4.242	7744	13182	4105
INORGANIC	2.373e-8	9.493e-8	-	-	4.301	7037	12155	245

Table 6.2: Sensitivity of SPACCIM1D-MOV to different reacting mechanisms during the FEBUKO scenario.

mechanism	S(VI)	NO_3^-	aORA1	aORA2	pH	stp	fcn	CPU [s]
CAPRAM2.3	2.383e-8	9.859e-8	4.134e-9	2.806e-9	4.195	3515	6295	77
CAPRAM2.4	2.386e-8	9.860e-8	4.126e-9	2.797e-9	4.193	3619	6456	134
CAPRAM2.4RED	2.384e-8	9.860e-8	4.129e-9	2.799e-9	4.193	3984	6931	97
CAPRAM3.0	2.386e-8	9.861e-8	4.168e-9	1.269e-9	4.199	3204	5732	271
INORGANIC	2.343e-8	9.662e-8	-	-	4.26	2915	5232	25

6.5 Feedback of multiphase chemical on microphysics

The Raoult term in the condensation rate is calculated using osmotic coefficient according to Pruppacher and Klett (1997). The microphysical model considers initially ammonium bisulfate aerosol. As described in the coupling scheme, SPACCIM allows the feedback of chemical particle composition onto microphysics. For that, the original Raoult term in the condensation rate calculation is replaced by the sum of the molar ratios (mol_{sol}/mol_w) of all soluble aqueous phase species

$$Raoult^k_{chem} = \sum_i^{N_{aqua}} mol^k_{sol_i}/mol^k_w.$$

When the feedback of chemistry onto microphysics is considered more particles are activated in the fixed bin case (Fig. 6.8). That means that droplets competing for the

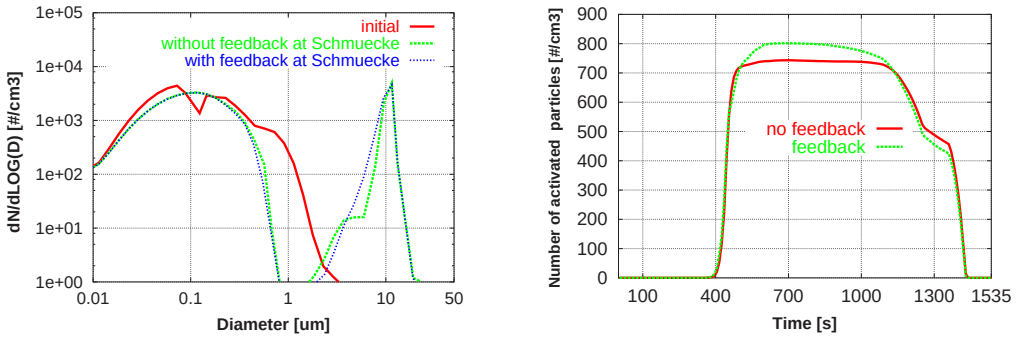

Figure 6.8: Number size distribution at Schmucke during FEBUKO with and without feedback (left), total number of 'activated' particle during FEBUKO with and without feedback (right).

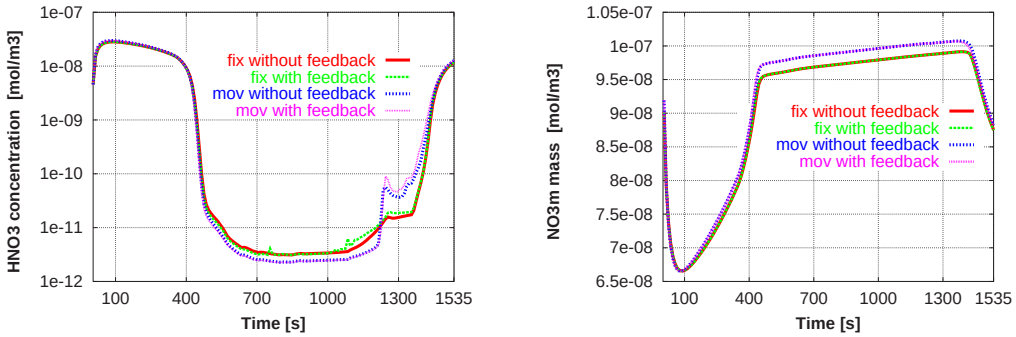

Figure 6.9: HNO_3 and NO_3^- simulated evolution during FEBUKO using CAPRAM2.4RED. Comparison is shown between the 'fixed bin' and the 'moving bin approaches with and without feedback.

same available humidity are smaller in size. When evaporation becomes significant, particles smaller in size evaporate faster. Therefore, the two curves in Fig. 6.8 (right) evolve almost identically during the evaporation phase. Moreover, a spectral analysis of the number distribution at the summit confirms this observation (Fig. 6.8, left). In the feedback run, the non-activated part of the spectrum shrinks towards smaller sizes. One explanation could be that the more realistic Raoult term delivered by chemistry reduces the critical supersaturation. Furthermore, more particles are being activated due to the lower critical radius. These additional smaller particles are activated and grow into droplets. No significant influence of the feedback on microphysics is observed for the moving bin version. The main reason may be that the Raoult term is calculated from the soluble fraction of the initial aerosol composition. For the "non-activated" particles, the ratio between soluble and total mass is only slightly changed by the gas uptake. For the "activated" particles, the Raoult term is dominated by the large water fraction. As seen in Fig. 6.9 for HNO_3 and nitrate, the effect of the feedback on the species evolution is also not substantial. We refer to Sehili et al. (2005a) for a further discussion of the differences between the moving and fixed bin approach.

6.6 Coupling time step and its control

The coupling strategy is based on a definition of a coupling time step Δt_{cpl} along which the two models communicate. Δt_{cpl} is a key control parameter of SPACCIM. It has an influence on chemistry, numerics and also on microphysics when considering feedback. A first and precautionary attempt to choose Δt_{cpl} is to take a small one. But this implies more numerical costs in the time integration of multiphase chemistry due to the larger number of restarts which are expensive for higher order implicit solvers. In contrary, using a large Δt_{cpl} increases the risk to not resolve critical time points like the start of the activation. Furthermore, the differences between the interpolated meteorological variables and their real values can adulterate also species chemical evolution. The benefit in the computational effort is bought by a lower accuracy in the simulated species concentrations (Tables 6.3 and 6.4). For the FEBUKO scenario, a coupling time step of 10 s appears to be reasonable and gives satisfactory results. SPACCIM allows also a dynamical control of Δt_{cpl} during the runs. This control is closely related to changes in LWC. During periods with large local variations of the LWC, Δt_{cpl} is reduced. If the changes in LWC are small then Δt_{cpl} can be increased. Additionally, critical points along the parcel trajectory (e.g., start of activation, summits and other turning points) are located and taken into account for the control.
The following implementation of this algorithm is realized:

BEGIN
Initialization
⋮
Index = 0
Flag = 0
Δ t_{cpl} = Δt_{cpl}(initial)
DO WHILE (t $\leqq$ End_{simul})
Initialization
⋮
t_{end} = t + Δt_{cpl}
DO WHILE (t $\leqq$ t_{end})
CALL Microphysics
Sum = $\sum_{k=1}^{K} \Delta LWC_k$ (increase/decrease in LWC)
$LWC_{relv} = \frac{ABS(Sum - Sum_{old})}{ABS(MAX\{Sum, Sum_{old}\})}$
IF (Index = 0) THEN
IF($LWC_{relv} \geqq LWC_{relv}$(old) .and. $\frac{Sum}{\Delta t_{micfys}} > 10^{-7}$) THEN
SCAL = LWC_{relv}
Index = 1 (SCAL is determined only one time)
ENDIF
ENDIF
IF ($LWC_{relv} \geqq$ SCAL) THEN
Flag = 1 (reduce Δt_{cpl} in the main loop)
EXIT
ELSE
Flag = -1 (increase Δt_{cpl} in the main loop)
ENDIF
Save
END DO
⋮
END DO
⋮
END.

The results in Tables 6.3, 6.4 and Fig. 6.10 for RISING illustrate the benefit of such dynamic strategy. However, our experiences for the FEBUKO runs shows that such strategy does not always bring noticeable gain. In general, simulations of multiphase processes for air parcels forced by synoptic events over a long period need the optimization of the control parameters. A dynamic choice of Δt_{cpl} is a promising issue in this context.

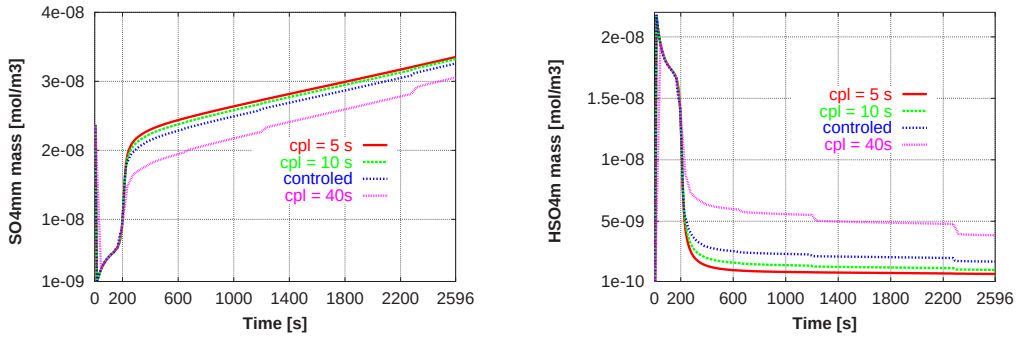

Figure 6.10: Sensitivity of SO_4^{2-} and HSO_4^- to different coupling time step with SPACCIM1D-FIX during RISING .

Table 6.3: Sensitivity of SPACCIM1D-FIX to different coupling time steps during the RISING scenario.

Δt_{cpl}	S(VI)	NO_3^-	aORA1	aORA2	pH	stp	fcn	CPU [s]
5	3.423e-8	1.152e-7	7.081e-9	7.188e-9	4.472	4747	6458	400
10	3.426e-8	1.152e-7	7.078e-9	7.193e-9	4.473	4447	6035	410
20	3.432e-8	1.152e-7	7.069e-9	7.204e-9	4.477	3875	5456	344
30	3.435e-8	1.152e-7	7.065e-9	7.211e-9	4.479	3631	5142	341
40	3.442e-8	1.152e-7	7.054e-9	7.224e-9	4.484	3275	4596	528
controlled	3.429e-8	1.152e-7	7.072e-9	7.201e-9	4.476	3446	4726	334

Table 6.4: Sensitivity of SPACCIM1D-MOV to different coupling time steps during the RISING scenario.

Δt_{cpl}	S(VI)	NO_3^-	aORA1	aORA2	pH	stp	fcn	CPU [s]
5	3.502e-8	1.150e-7	7.185e-9	7.371e-9	4.459	2233	2743	63
10	3.406e-8	1.150e-7	7.185e-9	7.365e-9	4.460	1686	2231	59
20	3.399e-8	1.138e-7	7.173e-9	7.320e-9	4.470	1557	2097	51
30	3.405e-8	1.150e-7	7.191e-9	7.372e-9	4.459	1304	1757	47
40	3.405e-8	1.150e-7	7.191e-9	7.372e-9	4.459	1266	1750	108
controlled	3.413e-8	1.149e-7	7.190e-9	7.375e-9	4.460	1578	1985	58

6.7 Size resolution of multiphase chemical model

The dimension of the ODE system (3.1, 3.2) depends on the size resolution of the spectrum. Usually, the multiphase chemistry uses the discretization of the spectrum specified by the microphysical model. Coarser resolutions RESCHEM for multiphase chemistry calculations reduce the dimension of the system and, consequently, the numerical costs. Obviously, the accuracy suffers in this case. Especially, the lower resolution of the spectrum part where activation takes place influences mainly the

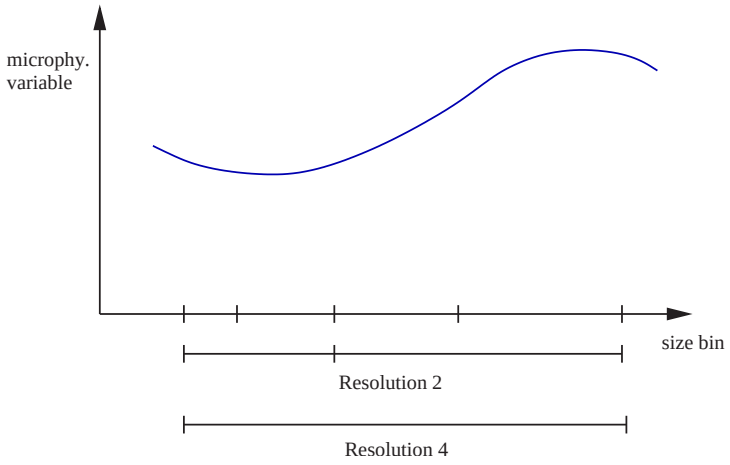

Figure 6.11: Coarse resolution for chemistry.

chemistry (Fig. 6.11). Simulations with RESCHEM = 2 and 4 are carried out. The use of RESCHEM = 2 is a good compromise between the loss of accuracy and the numerical gain (Tables 6.5 and 6.6). Furthermore, it is observed that the loss of accuracy using SPACCIM1D-FIX increases gradually with RESCHEM in the same tendency (increase or decrease). For SPACCIM1D-MOV, the loss of accuracy with RESCHEM = 4 evolves in an opposite way to RESCHEM = 2. A finer size resolution in microphysics as well as in multiphase chemistry improves the accuracy of chemical species concentrations (Tables 6.5 and 6.6). As expected, the effect of NUMFRAC is contrary to RESCHEM. Using NUMFRAC = 264 does not lead to a noticeable difference in species concentrations compared to NUMFRAC = 132. The numerical cost of a finer size resolution is evidently much higher. The default setup with NUMFRAC = 66 represents a good compromise between the chemical and numerical aspects.

Table 6.5: Sensitivity of SPACCIM1D-FIX to different chemistry resolution and different bin size resolution for CAPRAM2.4RED during FEBUKO scenario.

Resolution	S(VI)	NO_3^-	aORA1	aORA2	pH	stp	fcn	CPU [s]
DEFAULT	2.414e-8	9.688e-8	3.643e-9	2.612e-9	4.237	8336	14308	1412
RESCHEM = 2	2.435e-8	1.001e-7	3.494e-9	2.567e-9	4.185	6641	11475	335
RESCHEM = 4	2.477e-8	1.005e-7	3.427e-9	2.547e-9	4.154	6050	10395	311
NUMFRAC = 132	2.385e-8	9.634e-8	3.769e-9	2.655e-9	4.254	10310	17218	10472
NUMFRAC = 264	2.382e-8	9.619e-8	3.925e-9	2.714e-9	4.250	9949	16511	27008

Table 6.6: Sensitivity of SPACCIM1D-MOV to different chemistry resolution and different bin size resolution for CAPRAM2.4RED during FEBUKO scenario.

Resolution	S(VI)	NO_3^-	aORA1	aORA2	pH	stp	fcn	CPU [s]
DEFAULT	2.384e-8	9.860e-8	4.129e-9	2.799e-9	4.193	3984	6931	97
RESCHEM = 2	2.395e-8	9.986e-8	4.057e-9	2.769e-9	4.173	3846	6520	56
RESCHEM = 4	2.374e-8	8.791e-8	4.741e-9	3.106e-9	4.418	3077	5220	31
NUMFRAC = 132	2.343e-8	9.635e-8	4.251e-9	2.850e-9	4.233	4247	7295	319
NUMFRAC = 264	2.336e-8	9.629e-8	4.275e-9	2.861e-9	4.240	4661	8361	758

6.8 Optimal choice of numerical control parameters

The time step control of the BDF solver requires the definition of a relative error tolerance. Stronger relative tolerances imply smaller time steps and, hence, higher numerical costs. But risk of a solver failure is minimized in this case. When the solver fails, an expensive restart using sharper tolerances has to be performed. A compromise is reached when those two sides of the problem are taken into account. Thus, every simulated scenario needs its specific tolerance to reach "optimal" performance. In the case of FEBUKO simulations (Table 6.7), the convergence of the solver is ensured with RTOL $= 10^{-3}$ for both fixed and moving versions. No influence on the solution accuracy between sharper and weaker tolerance was observed. From a numerical point of view, the direct sparse Meis-Markowitz and Schur complement solvers discussed in Wolke and Knoth (2002) for time-constant microphysics remain comparable for more realistic coupled simulations (Table 6.8). Furthermore, the choice of AMF can become important under some microphysical conditions. The deviations between the numerical efficiencies of AMF (5.7), (5.10) and (5.11) become substantial during the "monotone" RISING scenario. Approximation (5.11) is comparable to (5.10). As shown in Table 6.8, less function evaluations fcn and, therefore, less CPU time are needed for approach (5.10) in comparison to (5.7). Here the transport matrix J^P is mostly lower bidiagonal due to the presence of condensation mainly. One explanation for the benefit of (5.10) could be that the

Table 6.7: Numerical efficiency of SPACCIM for different relative tolerances during FEBUKO scenario.

	SPACCIM1D-FIX			SPACCIM1D-MOV		
Relative tolterance	stp	fcn	CPU	stp	fcn	CPU [s]
RTOL = 1.E-7	17024	26742	1948	8776	14203	120
RTOL = 1.E-6	11902	19500	1731	6117	10322	132
RTOL = 1.E-5	8336	14308	1412	3984	6931	97
RTOL = 1.E-4	6010	10598	1351	2463	4188	65
RTOL = 1.E-3	3939	6913	1301	81694	2860	69

Table 6.8: Numerical efficiency of SPACCIM for different solver variants during FEBUKO and RISING scenarios.

			FEBUKO			RISING		
model	AMF	LU strategy	stp	fcn	CPU [s]	stp	fcn	CPU [s]
SPACCIM1D-FIX	(5.10)	Meis-Markowitz	9161	15997	1714	4447	6035	410
	(5.7)	Meis-Markowitz	9423	18563	1968	10491	43122	2050
	(5.11)	Meis-Markowitz	8336	14308	1412	5404	9961	610
	(5.10)	Schur complement	9138	15978	1723	4378	6061	403
	(5.7)	Schur complement	9345	18431	1867	10440	42543	2112
	(5.11)	Schur complement	8546	14467	1675	5388	9992	625
SPACCIM1D-MOV	(5.11)	Meis-Markowitz	3984	6931	97	1686	2231	59
	(5.11)	Schur complement	4134	7120	128	4131	5859	130

predicted vector of aqueous chemical species c is firstly updated through the solution of the sparse multiphase chemistry system (5.9) and then passed to the transport part (5.8). The vector c given by (5.9) is only slightly modified by (5.8) and remains closer to the solution of original system (5.5). In the opposite case, when the transport is performed first, after every occurrence of a convergence failure, the newly predicted vector c is first rearranged by the microphysical flux and then passed to (5.9) making it being a coarser approximation of the solution of (5.5). As a results, the convergence process is weakened. Surprisingly, the approximation (5.11) is the most efficient one for the FEBUKO simulations which needs further investigations.

6.9 Comparison of LSODE and ROS2

The second order non-autonomous Rosenbrock scheme ROS2 presented in (5.5) was likewise implemented to simulate the two case scenarios. The method was implemented with a step size control using the norm of the local error and a relative tolerance RTOL=10^{-1}. Some recent works (Djouad et al., 2002) advocated the use of ROS2 to simulate complex multiphase systems as it was shown that this scheme is more efficient than LSODE for large kinetic mechanisms. The simulation of FEBUKO scenario with a sparse ROS2 scheme using CAPRAM2.3 allowed us first to test the accuracy of the ROS2 as compared to the direct sparse solver based on the BDF scheme. This last was used with the default setup.
ROS2 had big difficulties to achieve the pure gas phase simulation during the downhill period. That was the reason that pushed us to limit the simulation to Gehlberg station after nearly 1360 s traveling time.
Species concentrations agreed in a good way and no noticeable deviations deserve to be mentioned. However, the numerical efficiency comparison between the two schemes shows clearly that ROS2 scheme is less efficient than the BDF scheme. This can be due to the required number of solutions of linear systems (two) in each step of the ROS2 scheme which is in relation with the step size control. The BDF

Table 6.9: Comparison of the numerical efficiency of the BDF and the ROS2 solvers during FEBUKO using CAPRAM2.3 mechanism. AMF = (5.11) for both cases.

model	scheme	jac	fcn	CPU [s]
SPACCIM1D-FIX	BDF	2397	10456	735
	ROS2	5001	15903	987
SPACCIM1D-MOV	BDF	1130	5016	66
	ROS2	1724	7296	84

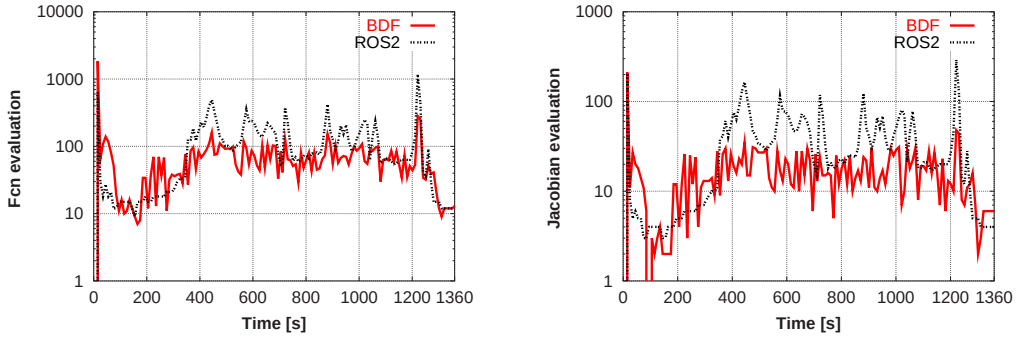

Figure 6.12: Evolution of the number of fcn and Jacobian evaluation needed by the two sparse solvers BDF and ROS2 during the simulation of FEBUKO using CAPRAM2.3.

scheme allows higher flexibility for Newton iterations making the step size control more efficient.

We have shown here under realistic conditions using complex multiphase chemical mechanisms that the direct sparse solver based on the BDF scheme is numerically more efficient than the nonautonomous second order Rosenbrock scheme.

6.10 Conclusion

The performance of the size-resolved parcel model SPACCIM with detailed microphysics and complex multiphase chemistry is discussed for simulations of realistic scenarios like event E I of the FEBUKO field campaign. The simple chemical mechanism INORG which contains only inorganic aqueous phase chemistry and very complex mechanisms of the CAPRAM family are involved in this study. A high flexibility is offered concerning the use of the reacting systems. Local events involving only condensation/evaporation process like FEBUKO can be analyzed using SPACCIM1D-MOV. The comparison between simulated and measured results shows a reasonable agreement. The sensitivity study indicates that the coupling scheme is robust and reliable. The setup of the control parameters affords to find an "optimal" adjustment depending on the considered application. The SPACCIM approach allows the

coupling of a complex multiphase chemistry model with microphysical codes of various types. In addition to the one-dimensional discretization of the particle spectrum used in the present chapter, a microphysical model with a two-component treatment of the microphysics (water and aerosol mass) is implemented into SPACCIM (Sehili et al., 2005a) and presented in the next chapter.

Chapter 7

Comparison of different model approaches

7.1 Introduction

Cloud-chemistry models are developed intensively with increasing complexity, leading to new knowledge and offering new possibilities to understand the physico-chemical processes taking place in the atmosphere. Intercomparing such detailed models is the way to test the robustness and reliability of their parameterizations and numerical schemes. The present chapter presents an intercomparison study between newly developed parcel models treating microphysics and chemistry with equal rigor.

Within atmospheric clouds, gaseous, aqueous, and solid species interact with each other in chemical and physical ways. These multiphase processes affect the global radiation field via modified scattering and absorption properties of the atmospheric system which in turn influences photolysis rates and the transport of chemical species. Modeling such complex physico-chemical processes demands the use of appropriate approaches and numerical techniques which differ from one single model to another. Literature addressing intercomparison of cloud chemistry models is not abundant and focuses only on some special issues. Jacobson (2002) presents some numerical techniques to solve the size- and time-dependent aerosol processes including dissolution and reversible chemistry. In Roelofs (1993) and Kreidenweis et al. (2003) simplified reacting mechanism and idealized meteorological conditions are used with a focus on bulk and size-resolved approaches. Some studies concerned with a more detailed reacting mechanism assume a prescribed microphysics (Sandu et al., 1996; Chaumerliac et al., 2000; Djouad et al., 2002; Barth et al., 2003). Furthermore, the phase interchange depends strongly on the phase surface area (Kreidenweis et al., 2003). For an appropriate description a highly resolved drop spectrum has to be considered.

The aim of the present intercomparison is to figure out the effect of different microphysical approaches and numerical schemes on cloud chemistry and, at last, on changes in particle composition and size distribution by microphysical processes. Moreover, these changes feed back on cloud microphysics. From the numerical point of view, the participating models differ in the manner of coupling between microphysics and multiphase chemistry, the discretization of the particle/droplet spectrum and the time integration schemes, see chapter 2. Two principal approaches for coupling microphysics and multiphase chemistry are considered. In the "fully-coupled" approach (Knoth, 2005), the model equations for the microphysical variables (temperature, water vapor, liquid water content) as well as for all chemical species are considered as one system which is integrated in a coupled manner by an implicit-explicit time integration scheme. Therefore, the splitting error between microphysics and multiphase is avoided. The second approach is the coupled model (SPACCIM) presented in chapter 4. This approach allows the coupling of a complex multiphase chemistry model with microphysical codes of various types. In this study, the multiphase chemistry is coupled to three microphysical models which use different discretization techniques of the particle/droplet spectrum.

In principle, the numerical behavior and/or the influence of microphysics on chemistry can change considerably for different chemical mechanisms,aerosol compositions or meteorological situations. Therefore, significant conclusions are only arrived at from simulations over a wide range of input data. Against this background, the behavior of the compared parcel models is discussed for three mechanisms of different complexity using the same gas phase system RACM (Stockwell et al., 1997) and two initial compositions. Two meteorological cases were studied. The first one is taken from Kreidenweis et al. (2003) representing a rising air parcel with a constant vertical velocity, traveling through a cloud. Inspired by the FEBUKO experiment (Herrmann et al., 2005a), the second case describes an air parcel undergoing a cycle of hill cap clouds.

7.2 Theoretical background and the models

This comparison study focuses on an appropriate characterization of the pathways of selected key species during cloud processes. Generally, the chemical multiphase processes are described by the mass balance equations of the species in a size-resolved droplet spectrum as described in (5). Note that the liquid phase chemistry is always performed for ideal solutions. In fact, this assumption is not valid for non-activated particles and small droplets. However, activity coefficients are not taken into account in this study. In this chapter, we will not discuss the uncertainties associated with bulk and size-resolved approaches. That has been done in many intercomparison studies and the effects are close to be understood (Roelofs, 1993). All the considered

models are size-resolved ones allowing alternatively a "fixed bin" or "moving bin" discretization of the particle/droplet spectrum. A part of our comparison is the evaluation of the uncertainties due to the use of the "fixed bin" or "moving bin" approach. Of course, such a comparison between the two approaches is possible only for condensation and evaporation. Preliminary setup simulations show that coagulation and break up can be neglected in our test scenarios.

In the following we discuss the main differences between the participating models. Table 7.1 summarizes some numerical features of the codes.

Table 7.1: Some numerical aspects of the compared models.

Models	Solver	Time step	Number of bins	Discretization scheme
SPACCIM	BDF	controlled	66	LDM
SPACCIM2D	BDF	controlled	66×90	LDM-2D
GALERKIN	Implicit Euler	controlled	66	DGM

7.2.1 The SPACCIM approach

The coupled model presented in the previous chapters represent the first approach involved in the present intercomparison study. The same multiphase chemistry is coupled with the "fixed bin" and "moving bin" versions of the 1D and 2D microphysical models presented in (2.5). SPACCIM offers accordingly four participating simulations. For the multiphase chemistry, several bins of the 2D grid are collected. In the "moving bin" version, a projection of particle mass on the aerosol grid is performed. That means, all bins with the same aerosol mass are summarized. In the "fixed bin" version, all particles with the same water mass are collected for chemistry. In this approach, the particle compositions of various bins are mixed for the chemistry calculations. This may be the reason for appreciable discrepancies of this approach from the other ones in our simulations. Furthermore, SPACCIM2D does not have to assume an internally mixed aerosol. However, a fair evaluation is only possible by the implementation of the more expensive and complicated 2D discretization also for the multiphase chemistry which will be tackled in the future

7.2.2 Fully-coupled GALERKIN approach

In this approach (referred to as GALERKIN), the model equations for the microphysical variables m (temperature, water vapor, liquid water content) as well as the system (5.1) for all chemical species are considered as one system which is integrated in a coupled manner. Therefore, no splitting error between microphysics and

multiphase chemistry occurs. Basics of the model and developement for the coagulation process are presented in (2.6). A more detailed description of the model with developement and application for condensation/evaporation process is presented in (Knoth, 2005). Köhler theory is likewise used to determine the growth rate with an explicit description of activation. Well diluted droplets are considered. A "fixed bin" and "moving bin" versions of the model are implemented. The time integration in this fully coupled model is based on an implicit-explicit scheme. In the "fixed bin" case, the advective part caused by condensation and evaporation is integrated by an explicit Euler scheme. All other terms including the multiphase chemistry are treated by an implicit first order BDF method. The time step control is performed by a Richardson extrapolation scheme. Similar to the SPACCIM code, the linear solvers exploit the special sparse structure of the system. Our simulations reveal clearly that this fully-coupled method with a DGM discretization technique works stable and keeps competitive to the SPACCIM approach.

7.3 Conditions of the intercomparison

Simulations for two different meteorological scenarios and two initial aerosol compositions were carried out. In all runs, the air parcel is located at 45^o N and starts at 600 m altitude for summer solstice at 9.00 AM (UTC). The RISING scenario is identical to the one presented in chapter 6. The air parcel in the WAVE scenario undergoes three cycles of hill cap clouds. It starts at 600 m altitude, rises adiabatically for 500 s until it reaches the altitude of 1000 m and a horizontal distance of 1000 m (an implicit 2 $\mathrm{m\,s^{-1}}$ horizontal velocity is assumed), stays at the same altitude for 200 s, then descents for 500 s to recover its initial altitude. This cycle is repeated three times for an overall traveling time of 1 hour (Fig. 7.1). This imitates the cloud processing of aerosols within air parcels in the convective boundary layer forced by large eddies going in and out of clouds.
The gas phase initial concentrations are the same for both scenarios (appendix B.2). The initial dry aerosol number size distribution consists of two lognormal modes, covering the Aitken and the accumulation size range (appendix B.2). Those data are inspired by the collected ones during E I of the FEBUKO experiment in the Thuringian forest in Germany (Herrmann et al., 2005a; Tilgner et al., 2005). The photolysis rates are determined for the corresponding mechanism with a damping factor of 0.5. Two different initial aerosol compositions with the same number and mass distribution are considered for RISING and WAVE. AEROSOL1 is characterized by a high soluble part and has a uniform composition for all particles over the whole spectrum as specified in the second mode in appendix B.2. AEROSOL2 is given as an external mixture of the two modes having different particle compositions. The particles of the first mode are less hygroscopic.

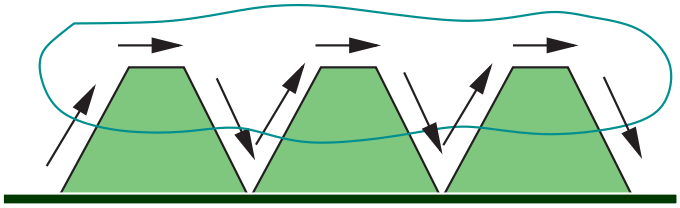

3 cycles (traveling time = 1 h)
Upwards traveling time: 500 s
Mountain residence time: 200 s
Downwards traveling time: 500 s
Altitude (valley): 600 m
Altitude (mountain): 1000 m

Meteorological initial values :
Absolute temperature: 280 K
Relative humidity: 95 %
Air density: 1.15 kg m^{-3}
Pressure (valley): 950 hPa
Pressure (mountain): 910 hPa

Figure 7.1: WAVE scenario schematic description.

During the initialization of the microphysical models with a one-dimensional spectrum, an internally mixed aerosol is generated also for AEROSOL2. But in contrast to AEROSOL1, the composition depends on the particle size. For SPACCIM2D the explicit mixture can be directly taken into account. It should be stressed that the initial aerosol composition is prescribed independently from the used chemical mechanism. The remarks stated in (6.1) concerning the non-reactive species, the initial pH value and the in-cloud photolysis rates correction remain valid in the present study. The first considered mechanism is the rather complex CAPRAM2.3 (Herrmann et al., 2000). The sulfate dedicated mechanism INORG was extracted from CAPRAM2.3 by neglecting all organic reactions. This is motivated by the fact that sulfate is one major constituent of aerosol mass (Hegg, 1985; Langner and Rodhe, 1991). In the gas phase sulfate is produced through the reaction of SO_2 with OH radicals. The dominant pathway for the conversion of S(IV) to S(VI) on the global scale is through aqueous phase oxidation of SO_2 in clouds. Sulfate is mainly produced via the reactions of SO_2 with H_2O_2 and O_3 in the aqueous phase (Walcek and Taylor, 1986; Lelieveld and Crutzen, 1991; Fleicher et al., 1996; Barth et al., 2000; Rasch et al., 2000). The third mechanism is the sulfur free mechanism BARTH (Barth et al., 2003) which was slightly modified for this comparison. Table 3.1 summarizes the characteristics of the considered multiphase reaction schemes. A more detailed description of the three mechanisms is given in Appendix B. It should be stressed that all models involved in the present study treat the chemical reactions terms and the phase transfer in the same way. In all implementations, the reaction system (gas and aqueous phases, phase transfer according to Schwartz) is read from an ASCII data file. Afterwards all data structures required for the computation of the chem-

ical terms and the corresponding Jacobians are generated. This approach allows a large flexibility in the choice of the chemical reacting mechanism.

7.4 Results

This intercomparison study should allow us to figure out the effect of different microphysical approaches on multiphase chemical processes, to compare the numerical schemes of involved models and to investigate the influence of the initial aerosol composition on the fate of some important chemical species like sulfate, nitrate or sulfuric dioxide for different kinds of cloud exposure. A selection is made for the most interesting and appropriate issues from our point of view. Comparison between models aims mainly to state differences and not to make an evaluation. In the following, time series figures describe averaged values over the whole spectrum. In the "moving bin" representation, the droplet radius corresponds to the average mass of one particle in each bin.

7.4.1 Microphysical aspects

Under the same meteorological conditions, the different microphysical models were expected to behave similarly. Fig. 7.2 shows the evolution of total liquid water content and supersaturation ratio of the parcel in RISING and WAVE. The liquid water content evolves linearly above cloud base during RISING and follows the orographic cycle in WAVE. As the parcel ascends the air becomes supersaturated and aerosol particles whose radii exceed the critical ones are considered "activated" and continue growing. Activation takes place at cloud base after nearly 200 s ascension in RISING and 150 s in WAVE. During the last, evaporation occurs down-hill allowing a processing of aerosol particles. As expected, no relevant differences have been noted between the models. The models contain an explicit size dependent description of the microphysical processes responsible for aerosol activation and droplet growth by condensation. The total particle number concentration is constant during all scenarios and all cases when no entrainment, no deposition and no secondary particle formation from the gas phase are considered. Fig. 7.3 illustrates the time evolution of the number concentrations of particles having radii larger than 1 μm during RISING. The two variants of SPACCIM remain comparable for both cases. This is in good agreement with GALERKIN-MOV for both AEROSOL1 and AEROSOL2. In the GALERKIN simulations around 200 cm^{-3} particles more activate with the "moving bin" version in comparison with the "fixed bin" version. This discrepancy is caused by the used advection scheme in GALERKIN-FIX (Knoth, 2005). SPACCIM2D versions which involve an additional resolution of the particulate mass simulate less activated particles in the order of 650 cm^{-3} in AEROSOL1. During AEROSOL2, the "moving bin" version shows a step-wise activation behavior.

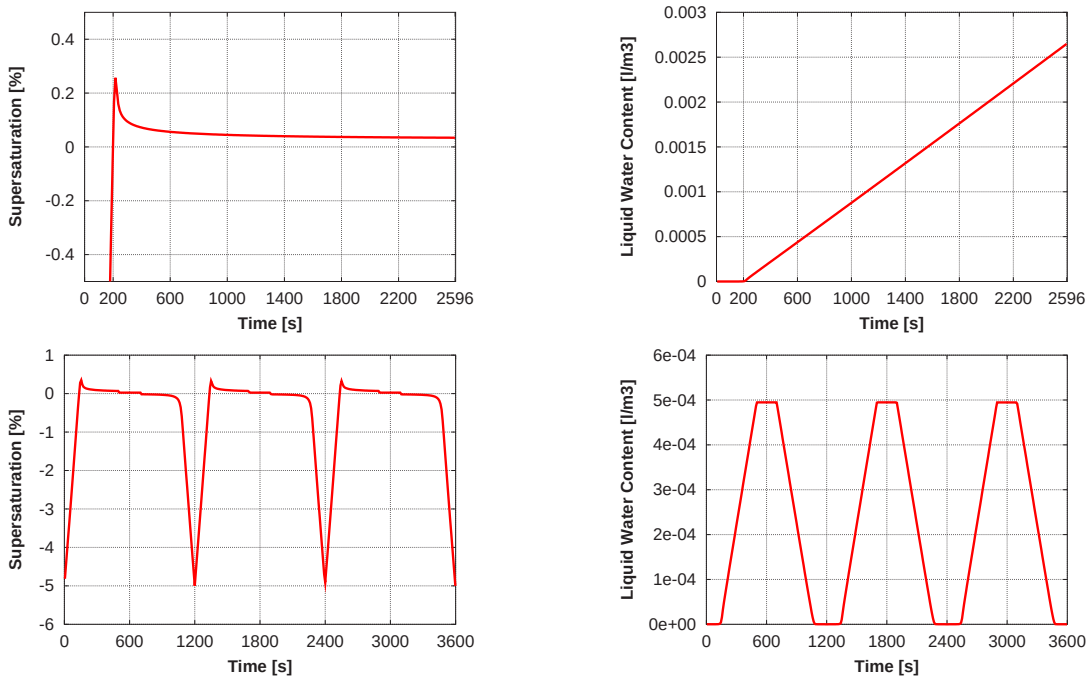

Figure 7.2: Supersaturation (left) and LWC (right) during RISING (top) and WAVE (bottom).

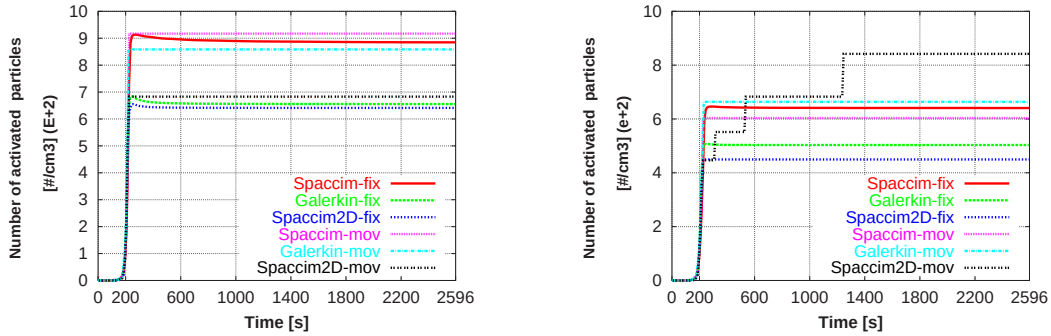

Figure 7.3: Number concentration of "activated" droplets ($R > 1$ μm) during RISING: AEROSOL1 (left); AEROSOL2 (right).

Fig. 7.4 (right) shows the effect of the external mixing of two modes with different hygroscopicity on activation (AEROSOL2). In Fig. 7.5 (left) the number distribution of SPACCIM1D-FIX and SPACCIM1D-MOV are compared for RISING. Such plots are problematic and require a regriding of the moving bin approach. Usually the size represented by a moving bin is compressed by condensation which leads to a higher number of bins with smaller sizes especially for the activated part of the spectrum. Therefore, the particle numbers of the k-th "moving bin" is scaled by the "compress-

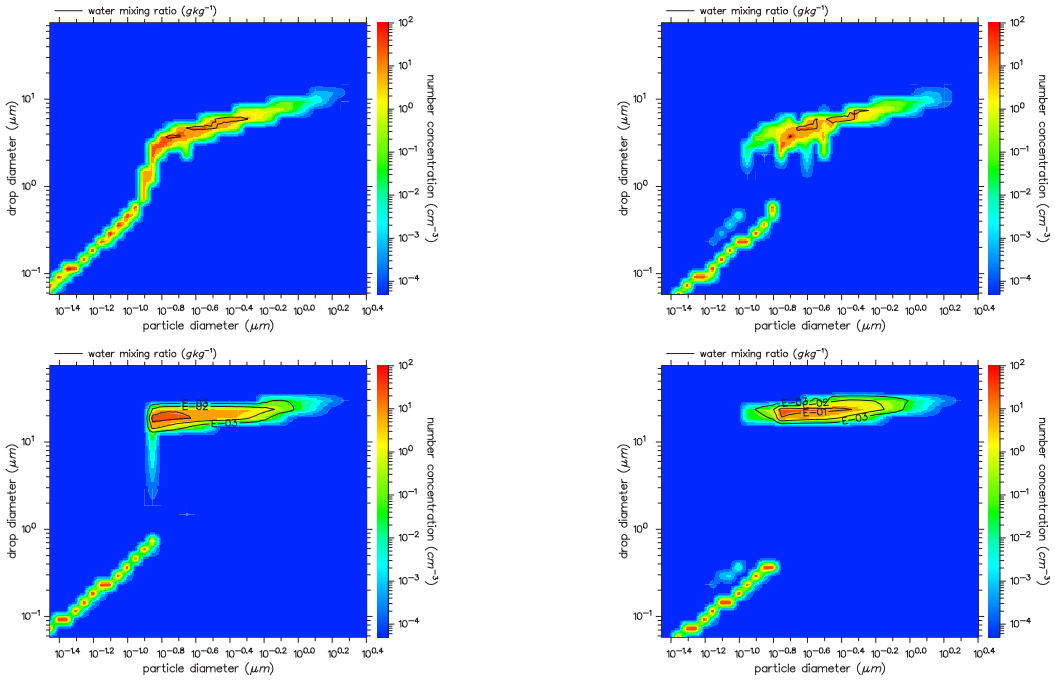

Figure 7.4: 2D number size distribution during RISING with SPACCIM2D-FIX: 26 m above cloud base (top) and at cloud top (bottom) for AEROSOL1 (left) and AEROSOL2 (right).

ing" factor $\log(d_0^{k+1}/d_0^{k-1})/\log(d^{k+1}/d^{k-1})$ where d_0^k and d^k denote the starting and the current mean diameter of the k-th bin. The good agreement between the "fixed" and "moving bin" approach for the non-activated spectrum is a hint that this scaling is appropriate. Fig. 7.6 (left) shows the development of the number distribution for SPACCIM1D-FIX and the WAVE AEROSOL1 scenario. Note that the parcel is located in the centre of the plateau after 600 s as well as 3000 s. At the end of the cycles, the two initial modes are more pronounced which is due to numerical diffusion.

A comparison between SPACCIM1D-FIX and GALERKIN-FIX for both scenarios is presented in Fig. 7.5 (right) and 7.6 (right). Additionally, a SPACCIM1D-FIX run without feedback is plotted. For both scenarios, feedback is insignificant. The main reason may be that the Raoult term is calculated from the soluble fraction of the initial aerosol composition. For the "non-activated" particles, the ratio between soluble and total mass is only slightly changed by the gas uptake. For the "activated" particles, the Raoult term is dominated by the large water fraction. For scenarios with higher gas scavenging or/and heterogeneous particle compositions, appreciable differences are observed (Wolke et al., 2005). The differences between SPACCIM1D-FIX and GALERKIN-FIX result from the different numerical schemes. An additional reason for this effect in GALERKIN, where gas uptake modifies directly the total mass

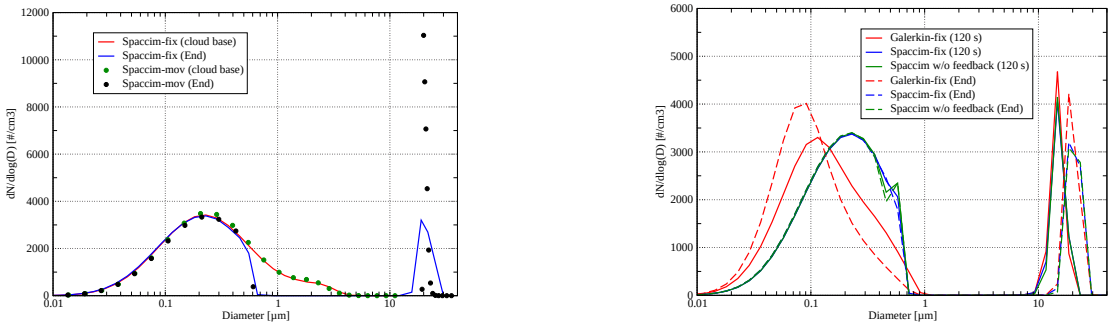

Figure 7.5: Number size distribution during RISING AEROSOL1 using CAPRAM2.3: With SPACCIM1D-FIX and SPACCIM1D-MOV (scaled according to the fraction size) at two different points of the trajectory (left); comparison between GALERKIN-FIX and SPACCIM1D-FIX (with and without feedback) at two positions of the air parcel (right).

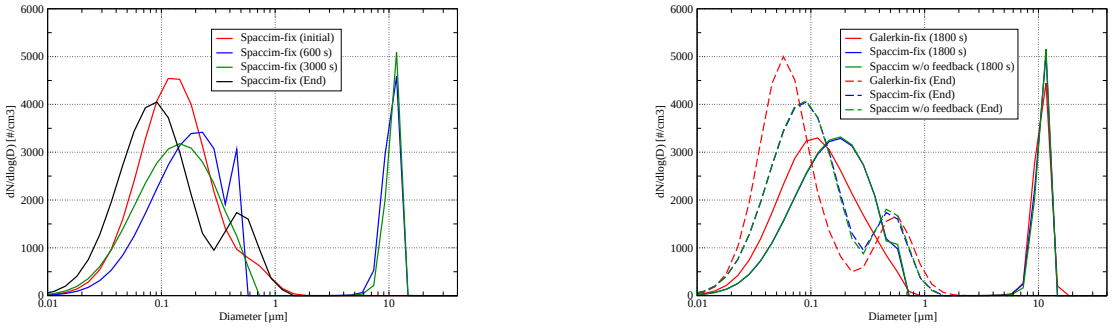

Figure 7.6: Number size distribution during WAVE AEROSOL1 using CAPRAM2.3: With SPACCIM1D-FIX at two different points of the trajectory (left); comparison between GALERKIN-FIX and SPACCIM1D-FIX (with and without feedback) at two positions of the air parcel (right).

in each bin, may be the redistribution of total mass from smaller to larger particles by phase transfer. Fig. 7.7 illustrates the evolution of non-water mass (NWM) during WAVE AEROSOL1. The order of complexity of the mechanism plays an important role here (left). The reacting systems INORG and BARTH where several pathways are omitted simulate 35 % less uptake from the gas phase compared to CAPRAM2.3. The increase of NWM over the simulation period is mainly caused by the nitrate production. Using CAPRAM2.3 for different models yields no significant differences regarding NWM (Fig. 7.7 right).

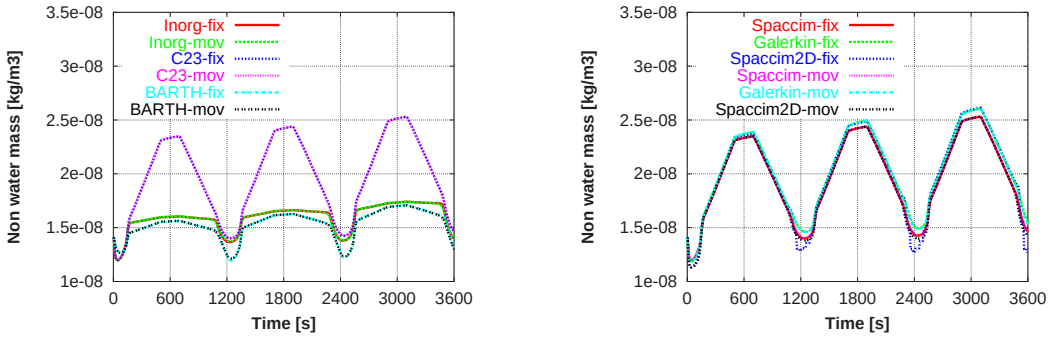

Figure 7.7: Time evolution of non-water mass during WAVE AEROSOL1 case: With SPACCIM for the three involved mechanisms (left); with the six models using CAPRAM2.3 (right).

7.4.2 Chemical aspects

Several species (SO_2, HNO_3, OH, SO_4^{2-}, HSO_4^-, NO_3^-, OH(aq)) are chosen to figure out the deviations between the participating models. The BARTH mechanism is excluded from the sulfur chemistry discussion. It has to be noted that the averaged values in Tables 7.2, 7.3, 7.5 and 7.6 are calculated without taking into account the values given by SPACCIM2D-FIX. Those last were singular and deviated in some cases largely from the ones given by the other participating models. As mentioned before, the coupling with chemistry in the case of SPACCIM2D-FIX is done in "1D way". Aerosol mass is collected over the dry mass spectrum for every droplet class (projection on y-axis in Fig. 7.4). The remapping on the fixed droplet grid of the so collected dry mass induces a different hygroscopic behavior that is not comparable with the other models. SPACCIM2D-MOV is rather comparable in this 1D projection (on x-axis in Fig. 7.4) to SPACCIM1D-MOV and, therefore, remains close to other models.

Sulfur chemistry. The in-cloud sulfate production from SO_2 oxidation takes place mainly in the activated part of the spectrum. During RISING , the vertical profile of sulfate production shows that the sulfate is formed mostly (70 % to 85 % depending on the models and mechanisms used) within 150 m above cloud base and that at the end of the simulation, 20 % to 45 % of SO_2 is oxidized. The "moving bin" models tend to predict more SO_2 uptake from the gas phase as shown in Fig. 7.8 and Tables 7.2 and 7.3. This deviation takes place all over the time beyond the start of activation and begins to be significant from nearly 300 m above cloud base in AEROSOL1 and 200 m in AEROSOL2. The number of activated particles is similar for the two approaches. The previous discrepancy can be explained by a different spectral distribution of the activated particles. A presence of more small activated droplets in the "fixed bin" approach due to the "remapping" can decrease the pH value and thus weakens the uptake process. In the "moving" representation, bins

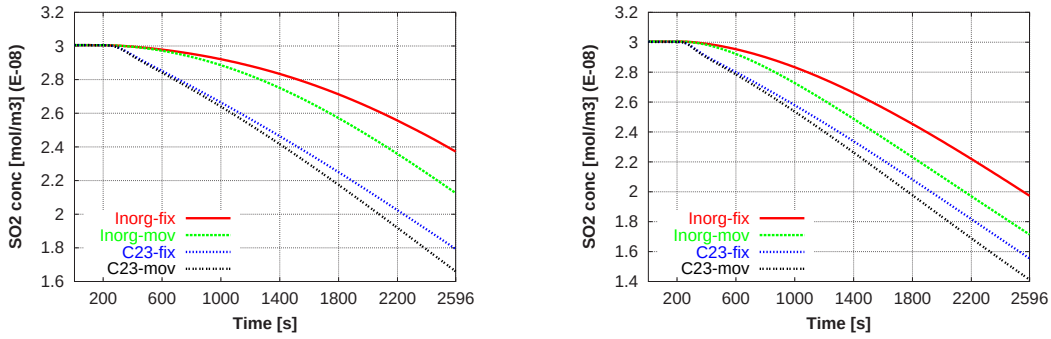

Figure 7.8: Time evolution of SO_2 concentration during RISING simulation with the SPACCIM model using INORG and CAPRAM2.3 mechanisms: AEROSOL1 (left); AEROSOL2 (right).

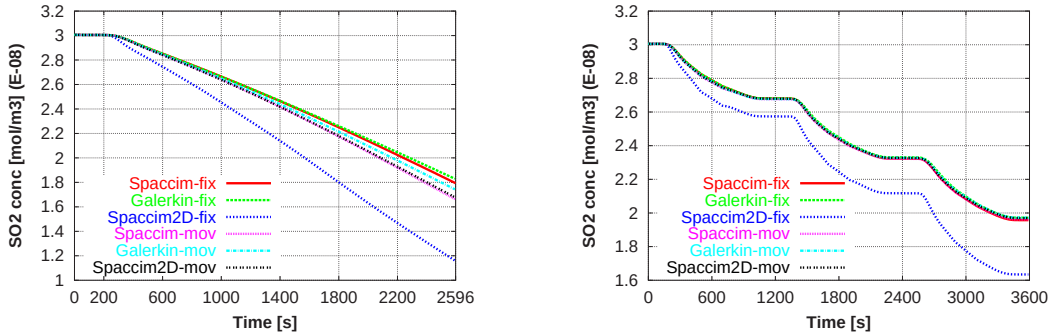

Figure 7.9: SO_2 concentration with the participating models using CAPRAM2.3 mechanism: RISING AEROSOL1 (left); WAVE AEROSOL1 (right).

grow independently from each other without microphysical fluxes. Deviation is increasing with droplet size. Apart from that, SO_2 uptake depends on the acidity of droplets. To investigate this phenomenon, additional simulations with higher pH values were performed and showed a better agreement between the "fixed" and "moving" approaches. In addition, simulations using weaker updraft velocities allowing a slower dilution process through water condensation which by turn also means higher pH values showed likewise a better agreement. The above considerations are relevant for both mechanisms involving sulfur. As shown in Fig. 7.8 there is more SO_2 uptake for CAPRAM2.3 where other pathways compete for reacting with aqueous SO_2. The gas phase species uptake and production are also sensitive to initial aerosol mixture. A lower soluble fraction like in AEROSOL2 restricts the activation of particles compared to AEROSOL1 as shown in Fig. 7.3. As a result, less droplets compete for the same available water vapor and, consequently, grow to bigger sizes with higher pH values which in turn means more SO_2 uptake. Fig. 7.9 shows that the GALERKIN models tend to take up less SO_2 while preserving the difference noted

between the "fixed" and "moving bin" approach. During WAVE, SO_2 undergoes a continuous uptake to the aqueous phase and its concentration decreases to the end of the cycles. The differences observed above between the mechanisms and the initial aerosol mixing for RISING are valid during WAVE although the dynamics are different. The different model results for SO_2 are close for both scenarios except the SPACCIM2D-FIX one where a singular behavior is observed. Tables 7.2 and 7.3 summarize the final concentrations of some gas phase species during RISING for both cases AEROSOL1 and AEROSOL2.

Table 7.2: Relative deviation of gas phase species to the average concentration for the involved models in % during RISING AEROSOL1. Average concentrations are in mol m^{-3}.

	SO_2		HNO_3			OH	
mechanism	INORG	CAPRAM2.3	INORG	CAPRAM2.3	BARTH	CAPRAM2.3	BARTH
AVERAGE	2.272e-8	1.739e-8	1.104e-11	1.951e-12	3.302e-12	7.231e-13	1.472e-12
SPACCIM1D-FIX	+4.4	+3.1	-11.6	-22.4	-18.3	-5.1	-2.9
SPACCIM1D-MOV	-6.4	-4.5	-15.2	-23.2	-26.9	-7.5	-12.8
GALERKIN-FIX	+7.4	+5.1	+22.7	+40.4	+49.1	+9.8	+17.5
GALERKIN-MOV	-0.6	+0.2	+4.0	+10.0	+2.3	+2.2	+1.4
SPACCIM2D-MOV	-4.7	-3.7	+0.1	-4.8	-6.0	+0.6	-2.9
SPACCIM2D-FIX	-33.4	-33.4	+115.6	-20.7	-47.8	+51.8	-18.2

Table 7.3: Relative deviation of gas phase species to the average concentration for the involved models in % during RISING AEROSOL2. Average concentrations are in mol m^{-3}.

	SO_2		HNO_3			OH	
mechanism	INORG	CAPRAM2.3	INORG	CAPRAM2.3	BARTH	CAPRAM2.3	BARTH
AVERAGE	1.909e-8	1.528e-8	1.293e-11	2.117e-12	3.972e-12	7.832e-13	1.490e-12
SPACCIM1D-FIX	+3.3	+1.7	-6.9	-12.3	-17.0	-4.3	-4.9
SPACCIM1D-MOV	-10.2	-7.5	-9.2	-15.7	-23.5	-5.5	-10.9
GALERKIN-FIX	+13.3	+9.0	+18.2	+33.9	+23.9	+8.2	+16.1
GALERKIN-MOV	-0.7	+0.5	0.0	+1.1	+23.9	+0.3	+0.2
SPACCIM2D-MOV	-5.5	-3.4	-1.9	-6.8	-7.3	+1.3	-0.2
SPACCIM2D-FIX	-20.3	-23.1	+100.6	+596.7	+318.6	+49.6	-3.7

The SO_2 analysis for RISING constitutes a basis to discuss differences between the models and the effect of different initial aerosol compositions. As mentioned above SO_4^{2-} and HSO_4^- are the products of SO_2 oxidation in clouds. Fig. 7.10 (top-left) illustrates the anti-correlation existing between HSO_4^- and SO_4^{-2} due to dissociation. The equilibrium is reached rapidly during the start phase. Between this period and the start of activation, SO_4^{2-} increases strongly accompanied by a moderate decrease in HSO_4^-. After the activation, this scheme is inverted. The differences noted previously for SO_2 are reflected clearly on SO_4^{2-}. HSO_4^- does not experience a significant difference. As expected, the models simulate more SO_4^{2-} where more SO_2 uptake is found. Obviously, the lower sulfate fraction of AEROSOL2 leads to a faster

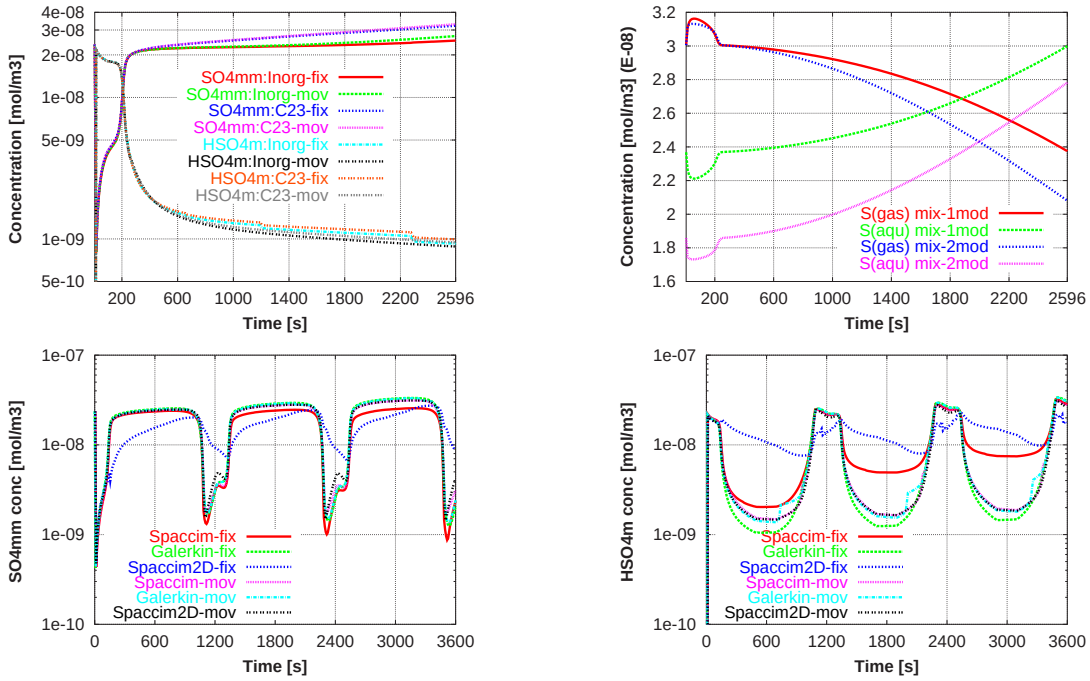

Figure 7.10: Evolution of SO_4^{2-} and HSO_4^- concentrations during RISING simulation with SPACCIM using INORG and CAPRAM2.3 mechanisms (top-left). Comparison of total sulfur processing in the gas and aqueous phase between AEROSOL1 and AEROSOL2 using the INORG mechanism (top-right). SO_4^{2-} and HSO_4^- evolution during the WAVE AEROSOL1 simulation with the participating models using CAPRAM2.3 mechanism (bottom).

SO_2 uptake (Fig. 7.10, top-right). The total sulfur concentration for both cases is conserved. Using WAVE to analyse SO_4^{2-} and HSO_4^- evolution allows to stress the effect of the hill cap cycles. As plotted in Fig. 7.10 (bottom), a cyclic behavior of SO_4^{2-} and HSO_4^- is observed. The minimum (maximum) SO_4^{2-} concentrations in the valleys (on the hills) decreases (increases) from cycle to cycle. Among the models, SPACCIM1D-FIX delivers lower SO_4^{2-} and consequently higher HSO_4^- concentrations. SPACCIM2D-FIX deviates again observably.

pH value. While a huge number of aqueous reactions depends on the acidity of the droplets, the variation of pH during any cloud exposure plays a substantial role. Cloud water pH starts with a low value determined by the charge balance and the initial aerosol composition. Then pH increases rapidly due to dilution as illustrated in Fig. 7.11. During RISING the four versions of SPACCIM are in good agreement. The two GALERKIN models deliver at the end of the simulation a higher pH value as resumed in Table 7.4. For all models, the average cloud water pH over the hills during WAVE decreases with the cycles (Fig. 7.11). The same behavior is observed

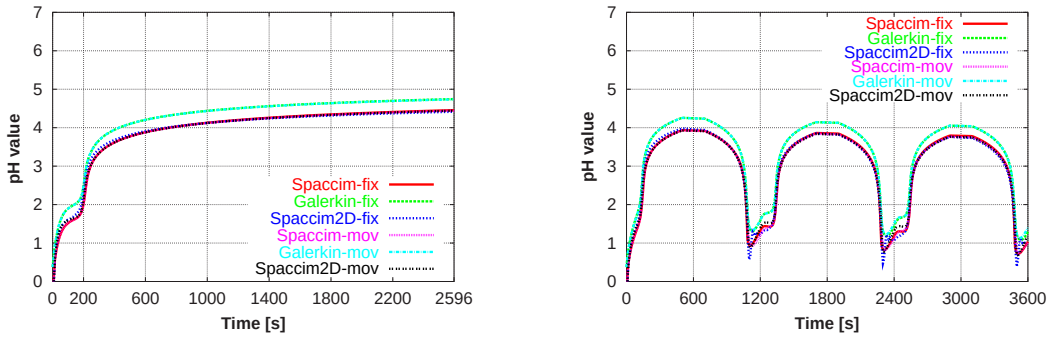

Figure 7.11: Mean cloud water pH (averaged over all bins) using CAPRAM2.3 mechanism according to models involved in the study: RISING AEROSOL1 (left); WAVE AEROSOL1 (right).

for the particles during the valley phases. This confirms the acidification of cloud condensation nuclei by cloud processing. Furthermore, pH changes lead to differences in cloud chemistry and gas uptake from cycle to cycle.

Table 7.4: Average cloud water pH values.

	AEROSOL1			AEROSOL2		
models	INORG	CAPRAM2.3	BARTH	INORG	CAPRAM2.3	BARTH
SPACCIM1D-FIX	4.51	4.45	4.40	4.67	4.58	4.54
SPACCIM1D-MOV	4.49	4.44	4.40	4.62	4.56	4.54
GALERKIN-FIX	4.82	4.74	4.68	4.97	4.86	4.81
GALERKIN-MOV	4.80	4.73	4.68	4.92	4.85	4.81
SPACCIM2D-MOV	4.49	4.44	4.40	4.62	4.55	4.53
SPACCIM2D-FIX	4.47	4.41	4.41	4.61	4.52	4.53

Nitrogen chemistry. Only WAVE results presented in Fig. 7.12 and 7.13 are discussed due to its clearness. The gas phase HNO_3 concentrations increases during the start period to realize the equilibrium with the particle phase. After the activation it is taken up rapidly almost completely. During the two following hill cap passages, HNO_3 experiences the same fate with differences between the mechanisms concerning the maximum concentration level. These discrepancies are reflected also on NO_3^- (Fig. 7.13). The periods of NO_3^- concentration sink correspond to valley periods where a transfer into the gas phase occurs. A more detailed analysis shows that NO_3^- is mainly formed by the HNO_3 uptake and, during cloudy periods, by oxidation processes. The partitioning between gas and particle/droplet phase is mainly controlled by the pH values. The BARTH mechanism, which tends to the highest acidity (Tab. 7.4), simulates less NO_3^- than the two other mechanism. Furthermore, the pH dependency entails also to differences between the models. The GALERKIN mod-

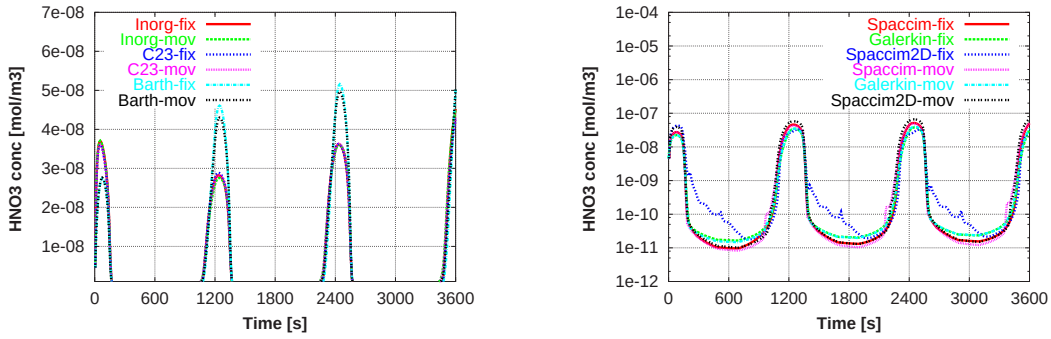

Figure 7.12: Time evolution of HNO_3 concentration during the WAVE AEROSOL1 simulation: with SPACCIM using the participating mechanisms (left); with the participating models using the BARTH mechanism (right) .

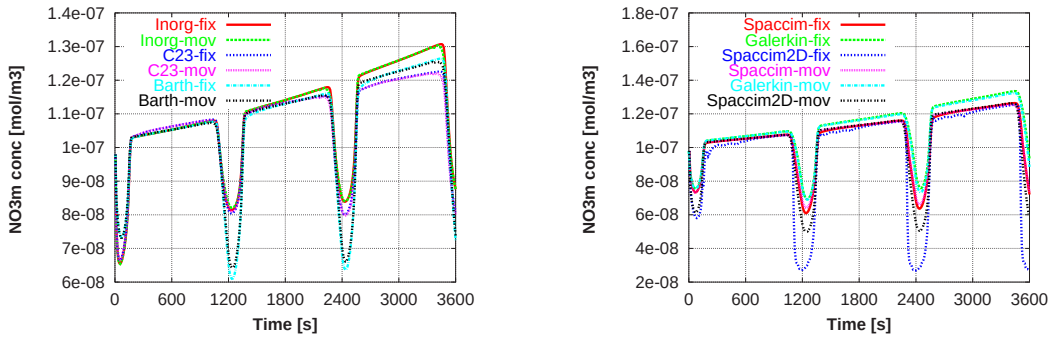

Figure 7.13: Time evolution of NO_3^- concentration during the WAVE AEROSOL1 simulation: with SPACCIM using the participating mechanisms (left); with the participating models using the BARTH mechanism (right).

els produce more particulate NO_3^- during cloudy period caused by the higher pH values. Altogether, SPACCIM1D, GALERKIN and SPACCIM2D-MOV show a relative good agreement. Again SPACCIM2D-FIX simulates less NO_3^- for the times corresponding to HNO_3 peaks. Fig. 7.14 summarizes the nitrogen processing. A global decrease tendency of gaseous nitrogen and, consequently, a global increase for aqueous nitrogen from cycle to cycle is observed. This increase contributes mainly to the NWM production discussed above. Deviations between the models are not substantial and occur during the valley periods. These observations are also valid for AEROSOL2 where less initial NO_3^- is included. Tables 7.5 and 7.6 summarize some aqueous phase species concentrations during WAVE at the end of the cycles for AEROSOL1 and AEROSOL2.

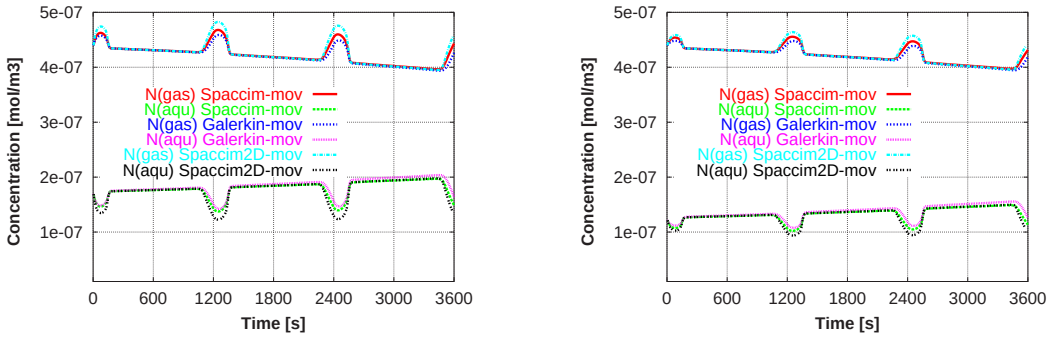

Figure 7.14: Comparison of nitrogen processing in the gas and aqueous phase between the participating models (moving bin) during WAVE using BARTH mechanism: AEROSOL1 (left) and AEROSOL2 (right).

Table 7.5: Relative deviation of selected aqueous phase species to the average concentration for the involved models in % at the end of the cycle during WAVE AEROSOL1. Average concentrations are in mol m^{-3}.

	SO_4^{2-}		HSO_4^-		NO_3^-		
mechanism	INORG	CAPRAM2.3	INORG	CAPRAM2.3	INORG	CAPRAM2.3	BARTH
AVERAGE	2.018e-9	2.803e-9	2.032e-8	2.864e-8	8.994e-8	8.399e-8	7.759e-8
SPACCIM1D-FIX	-6.0	-15.6	0.0	-1.5	-2.6	-3.6	-7.1
SPACCIM1D-MOV	+2.0	+14.9	-0.5	-3.7	-2.5	-4.5	-5.2
GALERKIN-FIX	-18.8	-25.3	+2.9	+7.4	+6.8	+5.4	+20.1
GALERKIN-MOV	-12.7	-13.8	+2.8	+5.4	+4.6	+2.4	+14.0
SPACCIM2D-MOV	+35.6	+39.9	-4.9	-7.5	-6.2	+0.3	-21.8
SPACCIM2D-FIX	+317.7	+217.4	-33.7	-38.5	-25.6	-20.3	-64.9

Table 7.6: Relative deviation of selected aqueous phase species to the average concentration for the involved models in % at the end of the cycle during WAVE AEROSOL2. Average concentrations are in mol m^{-3}.

	SO_4^{2-}		HSO_4^-		NO_3^-		
mechanism	INORG	C23	INORG	C23	INORG	C23	BARTH
AVERAGE	2.496e-9	3.593e-9	1.594e-8	2.456e-8	7.569e-8	6.926e-8	5.780e-8
SPACCIM1D-FIX	-7.2	-18.1	-0.6	-1.2	-3.4	-4.9	-9.1
SPACCIM1D-MOV	+22.4	+36.9	-3.6	-8.7	-3.6	-6.7	-6.1
GALERKIN-FIX	-23.1	-30.7	+3.6	+10.3	+7.2	+5.4	+20.2
GALERKIN-MOV	-20.5	-23.8	+6.1	+8.9	+5.5	+3.2	+14.8
SPACCIM2D-MOV	+28.5	+35.9	-5.2	-9.1	-5.6	+3.0	-19.6
SPACCIM2D-FIX	-39.7	-57.2	+82.0	+65.2	-31.9	-25.6	-66.5

7.4.3 Numerical aspects

The simulations offer the opportunity to examine the sensitivity of the model results to the applied numerical schemes and the way the coupling of microphysics

with chemistry is implemented. A fair and reliable numerical comparison between the six approaches is not possible since they are implemented and optimized for different kinds of applications. For instance, GALERKIN focuses on the description of aerosol-dynamical and multiphase chemical processes for non-activated particles. In the SPACCIM1D approach, an "optimal" choice of several control parameters (coupling time step Δt_{cpl}, required tolerance for the BDF scheme) can reduce the numerical costs markedly (Wolke et al., 2005). In this case, the numerical error is often increased. The compromise between accuracy and computational cost depends on the application as well as the objective of the simulation. In SPACCIM2D, the used implementation of the coupling scheme (especially the computation of the microphysical flux matrix) works well, but not very efficiently. An improvement should reduce the costs substantially.
Altogether the following remarks can be stated about the numerical efficiency. More processing costs are needed for "fixed bin" runs in comparison to the "moving bin" ones. The microphysical fluxes vanish during the last and no "remapping" to the original grid is done. In general, the computational costs are much lower for AEROSOL1 than for AEROSOL2. SPACCIM and GALERKIN yield comparable results. Usually, an "optimal" choice of Δt_{cpl} in the SPACCIM approach depends on the considered scenario. Large coupling time steps reduce the number of restarts which are expensive for higher order implicit solvers. Otherwise, the increased deviations between the interpolated microphysical variables and their real values can adulterate also species chemical evolution. The benefit in the computational effort is bought by a lower accuracy (Wolke et al., 2005). In this study, a coupling time step of 10 s seems to be reasonable and gives satisfactory results. Additionally, SPACCIM allows a dynamic control of Δt_{cpl} during the runs with respect to significant local liquid water content variations as shown before. This is to retrieve some special times like entering and leaving the cloud and also to catch the "turn over" points during the second scenario. The runs involving CAPRAM2.3 and BARTH in WAVE AEROSOL2 failed for weaker tolerances. High accuracy requirements are necessary to complete the runs. That is a synonym for smaller time steps and consequently more computational cost. Due to the detailed 2D microphysical structure, SPACCIM2D is much more expensive than the two others. As expected the INORG mechanism simulations run faster than BARTH which also runs faster than CAPRAM2.3 although the number of right hand side and Jacobian evaluations remain comparable for the three mechanism. Less time is spent for calculating the expensive Arrhenius terms in INORG. A complete numerical sensitivity study for SPACCIM can be found in Wolke et al. (2005).

Table 7.7: Numerical efficiency (CPU in s) of SPACCIM , SPACCIM2D and GALERKIN models during RISING using BARTH mechanism.

	AEROSOL1			AEROSOL2		
models	INORG	CAPRAM23	BARTH	INORG	CAPRAM23	BARTH
SPACCIM1D-FIX	207	599	256	302	980	393
SPACCIM1D-MOV	22	44	25	26	68	29
GALERKIN-FIX	285	850	178	138	2063	435
GALERKIN-MOV	96	473	99	78	649	223
SPACCIM2D-MOV	1875	2351	2259	13752	11022	17112
SPACCIM2D-FIX	6772	8229	7423	31058	46181	31987

7.5 Conclusion

The objective of this study was to figure out discrepancies between several detailed cloud chemistry models related to the use of different microphysical size-resolved approaches and numerical schemes with a focus on the "fixed bin" and "moving bin" representations. For that aim, various scenarios, initial aerosol mixing and chemical mechanisms of different complexity were involved with initial data taken from field measurements. It was shown that five out of the six participating models agree in an appreciable way in all scenarios and all cases. In principle, the SPACCIM2D models allow a more realistic description of the mixing state regarding hygroscopic properties of the particles. However, SPACCIM2D-FIX shows a singular behavior when calculating species concentrations. Further investigations including 2D chemistry discretization should be carried out to get a better evaluation. Moreover, the "fixed bin" models where a "remapping" to original grid is considered, simulate less uptake of gas phase species during RISING (cumulus type cloud). That has obviously a direct effect on the aqueous phase species evolution. During WAVE calculations imitating the natural cycle of air parcels entering and leaving clouds in the boundary layer, the differences stated above for the gas uptake between the "fixed bin" and "moving bin" representations are not observed. The pH values are in good agreement for all participating models with lower ones for WAVE. The loss of accuracy due to the use of "splitting" between microphysics and multiphase chemistry in the case of SPACCIM approach and the accompanying numerical costs are not significant in comparison with the fully coupled approach in GALERKIN. This indicates that the coupling strategy is robust and reliable.

Chapter 8

Parcel and 3D simulations

8.1 Introduction

The last years efforts invested to develop sophisticated cloud models with complex multiphase chemistry yields also to size-resolved parameterizations of cloud chemistry in chemistry-transport codes (Gong et al., 2003). We will focus here on the description and the numerical treatment of the interactions of microphysical processes and multiphase chemistry in regional chemistry-transport codes. For this purpose, a new coupling scheme between transport processes, microphysics and multiphase chemistry was developed and implemented in the model system LM-MUSCAT (Wolke et al., 2004). This coupling scheme is adapted to the implicit-explicit (IMEX) time integration scheme used in MUSCAT. In contrast to the usual "operator splitting" approach, the mass balance equations for all chemical species and all processes are integrated in a coupled way. The IMEX scheme utilizes the special sparse structure of the large system of stiff ordinary differential equations.
Evaluation of used atmospheric process parameterizations by mean of field measurements is often not possible or very expensive. Therefore, simulation studies under realistic atmospheric conditions which compare the results for these parameterizations with that of detailed parcel models involving an explicit description of the processes is necessary to quantify the error of the parameterization. We present cloud chemistry results simulated by LM-MUSCAT in comparison to SPACCIM simulations which uses a more detailed process description. The loss in the quality of the process description due to the simplification and its influence on the simulation results is discussed in view of an improvement of cloud chemistry parameterizations in higher dimensional models. Using SPACCIM , the movement of the air parcel follows a predefined trajectory generated by LM-MUSCAT. Entrainment and detrainment processes are considered in a parameterized form.

8.2 Entrainment and detrainment

The adaptation of the box model to simulate air parcels undergoing forcing along a trajectory delivered by a 3-D meteorological model (LM) implies the treatment of new issues that were neglected or did not show influence during the simulation of local adiabatic events as discussed in chapter 6 and 7.
Considering a more general non-adiabatic case needs the characterization of entrainment/detrainment processes. In contrast to 1-D and higher models where entrainment is parameterized with an entrainment rate depending on boundary conditions or velocities (e.g., linear variation with altitude), the parcel resolved model can only involve a constant or quasi-constant rate. In our approach, the entrainment is described by

$$\frac{\mathrm{d}x}{\mathrm{d}t} = ... - \mu(x - x_{env}) \ , \tag{8.1}$$

where x is the value of the variable in the air parcel, x_{env} the one in the environment and μ the entrainment rate given in [s^{-1}]. It represents the fraction of the unit volume of the parcel exchanged with the entrained air per unit time. This parameterization includes the exchange of meteorological variables like heat, and moisture as well as physical and chemical ones like aerosols and gas phase species. Recent studies for 1-D models with updraft velocities of the order of $1\,ms^{-1}$ (Liu and Seidl, 1998) and preliminary simulations have shown that a magnitude of the order of 10^{-2} to $10^{-4}\,s^{-1}$ constitutes a reasonable range for μ. The two boundaries correspond respectively to strong and weak entrainment. In our parcel simulations, two different entrainment rates were taken. A strong entrainment rate μ_{met} of the order of $10^{-2}\,s^{-1}$ is used for the meteorological forcing data. The mixing occurs rapidly in order to bring the parcel into the trajectory. To account for aerosol mixing, another approach for the entrainment rate is considered namely $\mu = \mu^{'}[\frac{N-N_{ent}}{N_{ent}}]$. N represents the total number of particles in the parcel and N_{ent} the total number of entrained particles at a supersaturation in the vicinity of 100 %. For $\mu^{'}$, the value of $10^{-4}\,s^{-1}$ is considered. Consequently, a detrainment process like sedimentation is compensated by entrainment making the total number of particles remaining constant. In such an approach, the effect of particle entrainment can have a significant influence only when coagulation process is acting. That requires generally a high liquid water content ratio in the parcel. In the present study, coagulation and, consequently, sedimentation play a negligible role. For the gas phase mixing, several entrainment rates ranging from the weaker value of 10^{-5} to the stronger one of 10^{-2} are tested to figure out the effect of gas phase entrainment.

8.3 Further adjustments.

Photolysis frequency correction due to cloud radiative forcing is also an issue that should be treated during the simulation of air parcels along trajectories delivered by a 3-D meteorological model. An option to adjust photolysis rates for the presence of clouds is to use the approach developed for the Regional Acid Deposition Model (RADM) (Chang et al., 1987) given by

$$j = j_{clear}[1 + a(F_{cld} - 1)] \tag{8.2}$$

where j is the corrected photolysis rate and j_{clear} the clear sky one. The cloud coverage a is in the range $0 \leq a \leq 1$. The cloud coverage field like the forcing meteorological data is delivered off-line by LM-MUSCAT. F_{cld} is the transmission coefficient depending on the zenith angle and accounting for the reflection effect of the surface and clouds. In this approach, the vertical direction is subdivided into three layers, below cloud , in cloud and above cloud. Accordingly, F_{cld} can assume three different formulations:

$$\begin{aligned} F_{cld} &= 1 + \alpha_i(1 - t_r)\cos\chi_0 && \text{above cloud layer ,} \\ F_{cld} &= 1.4 \cdot \cos\chi_0 && \text{in cloud layer ,} \\ F_{cld} &= 1.6\, t_r \cdot \cos\chi_0 && \text{below cloud layer.} \end{aligned}$$

The entities t_r and $(1 - t_r)$ represent respectively the reflection units due to surface and clouds albedo. We take $t_r = 0.5$. The factor α_i is a reaction dependent coefficient around unity and considered equal to one in our simulations. χ_0 is the solar zenith angle. The above formulations are valid for $\chi_0 \leq 60^0$. When $\chi_0 > 60^0$ values for F_{cld} evaluated at $\chi_0 = 60^0$ are used.
Sedimentation is considered using the approximate terminal fall velocity presented in (2.4.2).

8.4 The 3D modeling system

The model system consists of the chemistry-transport model MUSCAT and the online-coupled, non-hydrostatic meteorological model LM (Doms and Schättler, 1999; Schättler and Doms, 1999) which is the operational forecast model of the German Weather Service DWD. Both codes are parallelized, work on their own predefined fraction of available processors and have their own time step control. In the multiscale chemistry-transport code MUSCAT, the chemistry-transport processes are described by systems of time–dependent, three–dimensional transport equations with reactive terms.

Multiblock Grid. In MUSCAT a static grid nesting technique (Wolke and Knoth, 2000; Knoth and Wolke, 1998b) is implemented. The horizontal grid is subdivided into so-called "blocks". Different resolutions can use for individual sub-domains in the multiblock approach. This allows fine resolution for the description of the dispersion in urban regions and around large point sources. This structure originates from dividing an equidistant horizontal grid (usually the meteorological grid) into rectangular blocks of different size. By means of doubling or halving the refinement level, each block can be coarsened or refined separately. This is done on condition that the refinements of neighbouring blocks differ by one level at the most. The maximum size of the already refined or coarsened blocks is limited by a given maximum number of columns. The vertical grid is the same as in the meteorological model.

The spatial discretization is performed by a finite-volume scheme on a staggered grid. Such schemes are known to be mass conservative because of the direct discretization of the integral form of the conservation laws. For the approximation of the surface integrals, point values of the mixing and its first derivative are needed on the cell surfaces. To approximate the mixing ratio at the surface both first order upwind and biased upwind third order procedure with additional limiting (Hundsdorfer et al., 1995) are implemented. This scheme has to be applied to non-equidistant stencils which occur at the interface of blocks with different resolutions (Knoth and Wolke, 1998b).

Time Integration. For the integration in time of the spatially discretized equation an IMEX scheme (Wolke and Knoth, 2000; Verwer et al., 1998) is applied. This scheme uses explicit second order Runge-Kutta methods for the integration of the horizontal advection and an implicit method for the processes taking place in a column. The fluxes resulting from the horizontal advection are defined as a linear combination of the fluxes from the current and previous stages of the Runge-Kutta method. These horizontal fluxes are treated as "artificial" sources within the implicit integration. A change of the solution values as in conventional operator splitting is thus avoided. Within the implicit integration, the stiff chemistry and all vertical transport processes (turbulent diffusion, advection, deposition) are integrated in a coupled manner by the second order BDF method. We apply a modification of the code LSODE (Hindmarsh, 1983) with a special linear system solver and a restriction of the BDF order to 2. The error control can lead to several implicit time steps per one explicit step. Furthermore, different implicit step sizes may be generated in different blocks. The "large" explicit time step is chosen as a fraction of the CFL number. This value has to be determined for each Runge-Kutta method individually in order to guarantee stability and positivity. Higher order accuracy and stability conditions for this class of IMEX schemes are investigated in Knoth and Wolke (1998a).

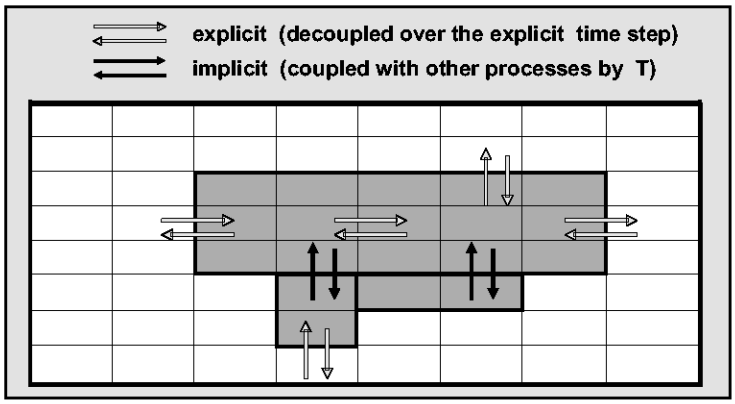

Figure 8.1: Schematic representation of the mass fluxes in the cloud chemistry implementation.

Gas Phase Chemistry. The chemical reaction systems are given in ASCII data files in a notation that is easily understandable. For the task of reading and interpreting these chemical data we have developed a preprocessor. Contained in its output file are all data structures required for the computation of the chemical term and the corresponding Jacobian. Changes within the chemical mechanism or the replacement of the whole chemistry can be performed in a simple and comprehensive way. Several gas phase mechanisms (e.g. RACM, RADM2, CBM IV) are used successfully in 3D case studies. Time resolved anthropogenic emissions are treated in the model as point, area and line sources. It is distinguished between several emitting groups. Biogenic emissions are parameterized in terms of land use type, temperature and radiation. Dry and wet deposition processes are also included.

Implementation of cloud chemistry. For the description of multiphase processes in LM-MUSCAT, the SPACCIM approach is applied to Eulerian grid models. According to the IMEX time integration scheme in MUSCAT, all horizontal mass fluxes and the mass fluxes over cloud boundaries (only for the main aerosol species) are integrated explicitly (Fig. 8.1). All time-averaged mass fluxes between neighbored vertical cloud grid cells are included in the microphysical fluxes f_{mphys}. Using an appropriate order of variables, the mass fluxes T_{ij} in (5.3) become tridiagonal matrices. An efficient numerical solution of this extended system requires an adapting of the sparse linear system solvers.

Aerosol Dynamics. For simulation of aerosol-dynamical processes the model MADMAcS I (Wilck and Stratmann, 1997) was included in MUSCAT. The particle

size distribution and the aerosol-dynamical processes (condensation, coagulation, sedimentation and deposition) are described using the modal technique. The mass fractions of all particles within one mode are assumed to be identical. Particle size distribution changes owing to various mechanisms, which are divided into external processes like particle transport by convection and diffusion, deposition and sedimentation as well as internal processes like condensation and coagulation.

Parallelization. The parallelization approach is based on the distribution of blocks among the processors. Inter-processor communication is realized by means of MPI. The exchange of boundary data is organized as follows. Since the implicit integration does not treat horizontal processes, it can be processed in each column separately, using its own time step size control. An exchange of data over block boundaries is necessary only once during each Runge-Kutta sub-step. Each block needs the concentration values in one or two cell rows of its neighbours, according to the order of the advection scheme. The implementation of the boundary exchange is not straightforward because of the different resolutions of the blocks. The possibilities of one cell being assigned to two neighbouring cells or of two cells receiving the same value must be taken into account. We apply the technique of "extended arrays": the blocks use additional boundary stripes on which incoming data of neighbouring blocks can be stored. Hence, each processor only needs memory for the data of blocks that are assigned to it.

Online-coupling between muscat and lm The meteorological and the chemistry-transport algorithms have their own separate time step size control. The coupling procedure is adapted to the applied IMEX schemes in the chemistry-transport code. Each stage of the IMEX scheme requires a new calculation of the horizontal fluxes and an implicit integration cycle. All meteorological fields are given with respect to the equidistant horizontal meteorological grid. They have to be averaged or interpolated from the base grid into the block-structured chemistry-transport grid with different resolutions. The velocity field is supplied by its normal components on the faces of each grid cell, and their corresponding contravariant mass flux components fulfill a discrete version of the continuity equation in each grid cell. Since LM solves a compressible version of the model equations an additional adjustment of the meteorological data is necessary. The velocity components are projected such that a discrete version of the continuity equation is satisfied. The main task of this projection is the solution of an elliptic equation by a preconditioned conjugate gradient method. This is also done in parallel on the LM processors. The projected wind fields and the other meteorological data are gathered by one of the LM processors. This processor communicates directly with each of the MUSCAT processor.

Dynamical Load Balancing. Consider a static partition where the blocks are

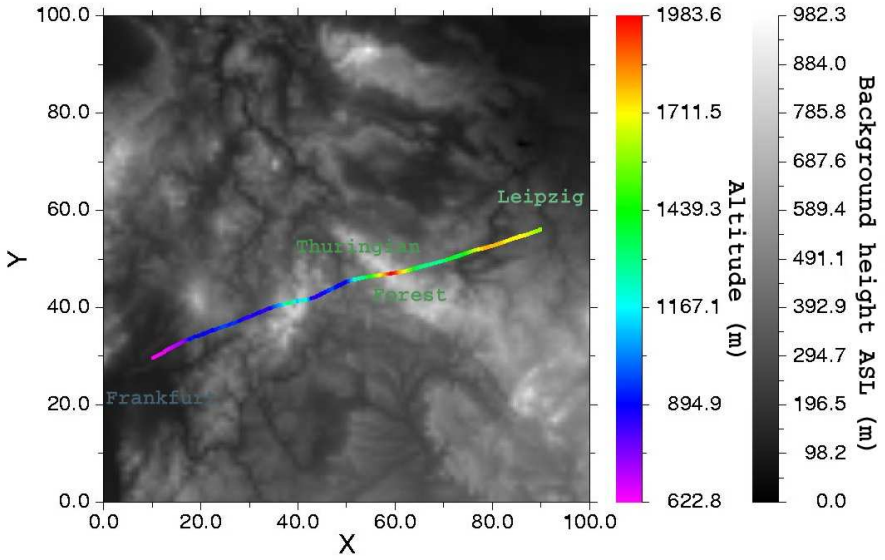

Figure 8.2: Trajectory simulated by LM-MUSCAT for a period of 8 hours on 25 October 2001, Ref. time 11h.00 min (start at 6h.10 min). Horizontal resolution 2.8 km.

distributed between the processors only once at the beginning of the programs run time. Here, we use the number of horizontal cells (i.e., of columns) as measure of the work load of the respective block. Therefore, the total number of horizontal cells of each processor is to be balanced. This is achieved by the grid-partitioning tool ParMetis (Karypis et al. 1998). It optimizes both the balance of columns and the "edge cut", i.e., it takes care of short inter-processor border lines. In order to improve the load balance, techniques for redistribution of blocks have been implemented (Wolke et al., 2001). A blocks work load is estimated using the numbers of Jacobian and function evaluations applied during a past time period. According to the work loads of the blocks, ParMetis searches for a better distribution, besides minimising the movements of blocks. The communication required for the exchange of block data can be done by means of similar strategies as for the boundary exchange.

8.5 Results and discussion

8.5.1 Description of the scenarios.

The parcel trajectory is determined inside the domain simulated by the 3-D LM-MUSCAT system for a prescribed period. The trajectory is calculated through the

definition of a reference point from which backward and forward time resolved interpolated meteorological variables are calculated parting from the coarser data delivered from LM. This constitutes the whole forcing data of the event. LM-MUSCAT is used on a 100 × 100 × 40 grids cells domain with 2.8 km horizontal grid resolution. Two parcel simulations are performed on two different domains. The first one covers central Germany (Thuringia) and the second one the northeast part of Germany (Saxony) as shown in Fig. 8.2 and 8.7. During the first scenario, only a parcel simulation is carried out. The aim at this stage was to test the feasibility of such an approach and to asses the quality of the results under the lightening of the used parametrizations. This scenario is characterized by a high LWC at the reference point (Mount *Schmücke* in the Thuringian forest). The simulation is performed for 8 hours. The air parcel starts traveling at 50.22^o N, 8.82^o W and 624 m altitude on 25 October 2001 at 6h.10 min (UTC). The reference point is reached at 11.00 AM. The background gas phase initial concentrations as well as initial dry aerosol composition are delivered by a preliminary LM-MUSCAT run which uses an emission inventory registered by the German environment agency. The initial dry aerosol number size distribution consists of two lognormal modes, covering the Aitken and the accumulation size range derived from FEBUKO field measurements. The initial pH value is determined through the charge balance and aerosols initial composition and is then computed dynamically throughout the whole simulation time.

In the second scenario, cloud chemistry simulations for both parcel and 3D models are performed. The simulation covers 5 hours. The air parcel starts traveling at 50.32^o N, 11.72^o W and 1280 m altitude on 24.10.2001 at 13.00 PM (UTC). This scenarios is designed mainly to perform comparison between the two approaches. It has to be noticed that the two scenarios use the same gas phase and aerosol initial conditions.

8.5.2 Results for the 25th October 2001 case study

As mentioned before, the first case study aims to assess the quality of the results given by the parcel simulation and in particular the reliability of the used parametrization of the entrainment process. The first indication is obtained by comparing the total LWC simulated by SPACCIM and LM. The two models show a good agreement (Fig. 8.3). The maximum LWC (10^{-3} l/m^3) corresponds to the reference point (Schmücke) after nearly 5 hours traveling. The number and LWC size distributions at different points of the trajectory plotted in Fig. 8.4 illustrate the explicit description of activation and its dependence on the available humidity and the processing of aerosol when the parcel travels out off clouds.

A high LWC means that droplets which grew by condensation are large enough in size to trigger the coagulation process. In this case, the total number of particles do

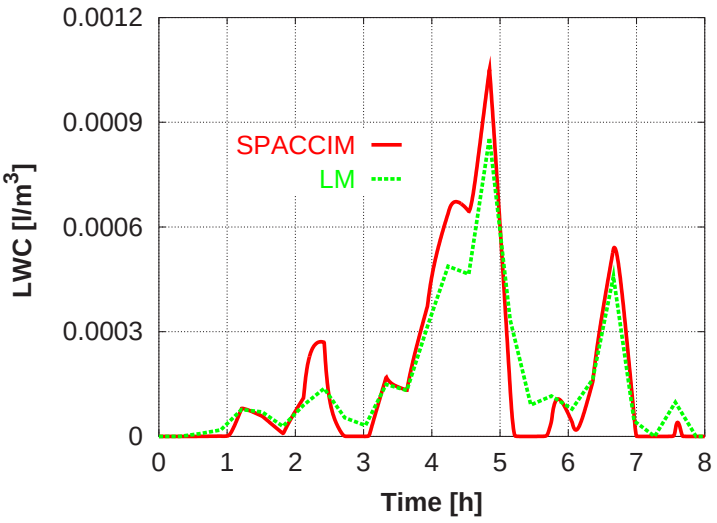

Figure 8.3: Total LWC calculated by SPACCIM compared with the one given by the forcing data from LM.

not remain constant but decreases (Fig. 8.5 right). During the non-cloudy simulation periods, the total number of particles remains constant as expected. The correlation between total LWC and NWM shown in Fig. 8.5 (left) due to phase transfer processes is another indication that the weak entrainment rate for gas phase species is justified. This issue is discussed in more detail in the second case study. The continuous increase of the total mass of ammonium, nitrate and S(VI) in the parcel is a direct effect of the entrainment process (Fig. 8.6). In an adiabatic case, one should expect a stronger decrease in the total species mass when LWC vanish. Another

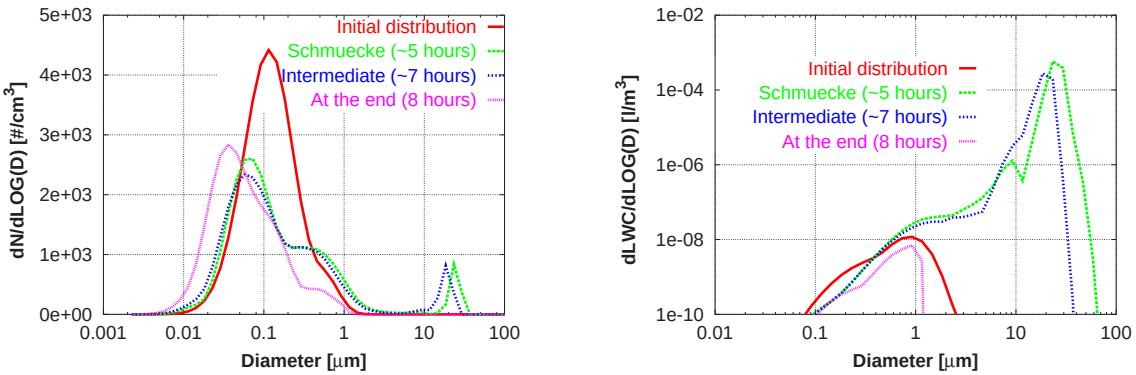

Figure 8.4: Number (left) and LWC (right) size distribution evolution for four positions of the air parcel simulated with SPACCIM during the first test scenario.

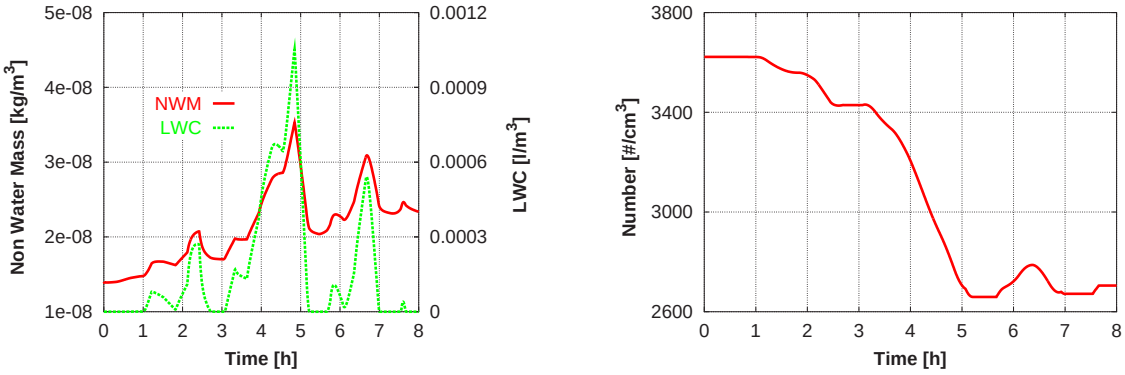

Figure 8.5: Correlation existing between the total LWC and the total NWM relative to the uptake process. The entrainment rate for gas phase species $\mu_{gas} = 10^{-4}.s^{-1}$(left); Time series of the total number of particles during the first scenario simulated with SPACCIM (right).

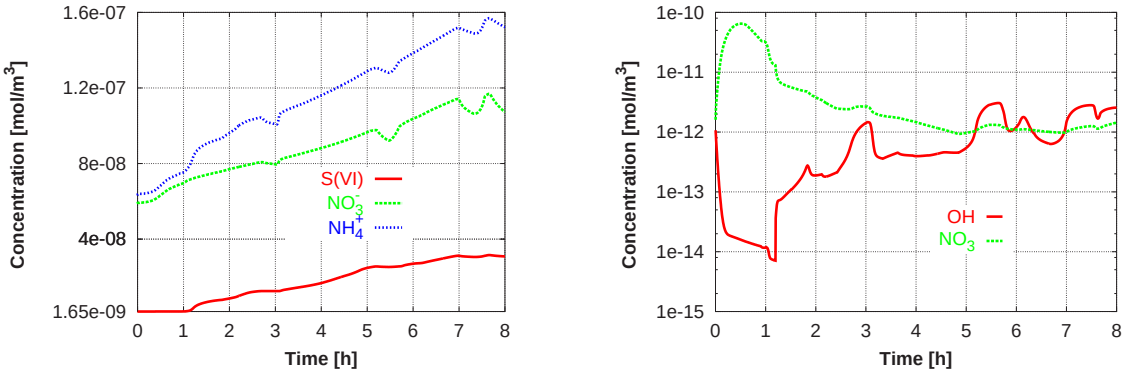

Figure 8.6: Time series of S(VI), NO_3^- and NH_4^+ (left); OH and NO_3 (right) during the first scenario.

feature recovered by the simulation is the simultaneous presence of the night time chemistry radical NO_3 and the day time radical OH during the sunrise period (after nearly 1 hour simulation corresponding to 7h.00 min (UTC))and shortly after.

8.5.3 Results for the 24th October 2001 case study

Influence of the gas phase entrainment rate. Gas phase species evolution shows an important dependence on the gas phase entrainment rate for parcel simulations. A high entrainment factor comparable to the meteorological one makes the concentration of gas phase species strongly dependent on the LWC in the parcel. The production of gas phase species during evaporation periods is observed (e.g., SO_2, Fig. 8.8 right). In this case, the pH value which represents the averaged one over the

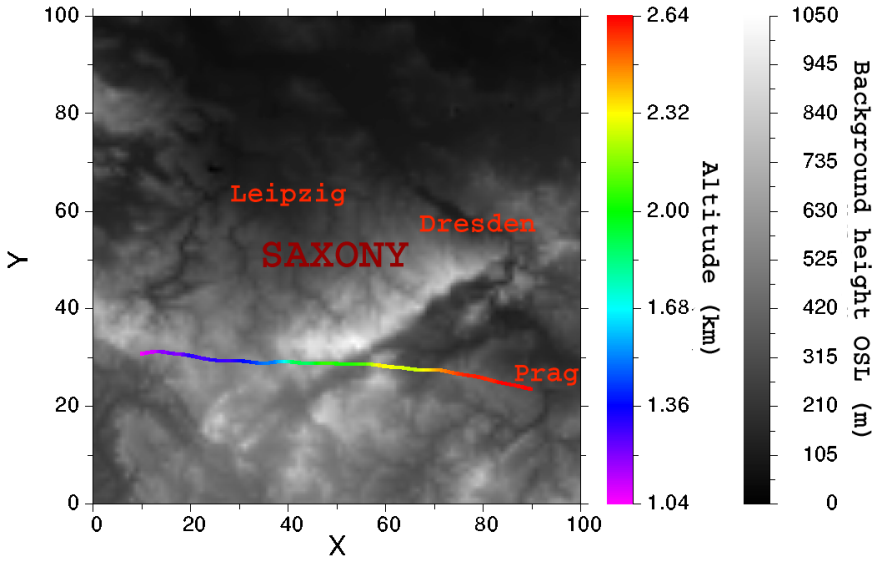

Figure 8.7: Trajectory simulated by LM-MUSCAT for a period of 5 hours on 24 October 2001, Ref. time 15h.00 min (start at 13.00 min). Horizontal resolution 2.8 km.

whole spectrum tends to increase and remains over the value of 5 for entrainment rates larger than $10^{-3}s^{-1}$. On the other hand, considering smaller or no entrainment leads to a non-realistic description of trace gas processing by clouds. The gas phase moderate entrainment rate of $10^{-4}s^{-1}$ seems to constitute an appropriate value in order to account for both aspects. This is confirmed by Fig. 8.8 (right) where the correlation between the NWM and LWC is still present for $\mu(g) = 10^{-4}s^{-1}$ all over the simulation time and is lost for $\mu(g) = 10^{-3}s^{-1}$ during the evaporation period.

Comparison of parcel and 3D simulations. As shown in Fig. 8.9 (left), SPACCIM simulates more total liquid water content (LWC) compared to the one given by the forcing data from LM. This deviation reaches its maximum of more than 30 % after 2 hours. In SPACCIM, cloud processes are treated explicitly in a spectral form including activation and the description of the water phase transfer feedback on water vapor and air temperature (latent heat release). In the 3D model LWC is parametrized in a bulk form including cloud water and rain water. The discrepancy mentioned above is due to 3D effect and should be minimized through the appropriate choice of μ_{met}. The number size distribution in Fig. 8.9 (right) illustrates the broadening and the splitting of the spectrum into activated and non activated parts caused by the explicit description of activation after 2 hours corresponding with maximum LWC. Currently, these issues are not implemented in LM-MUSCAT.

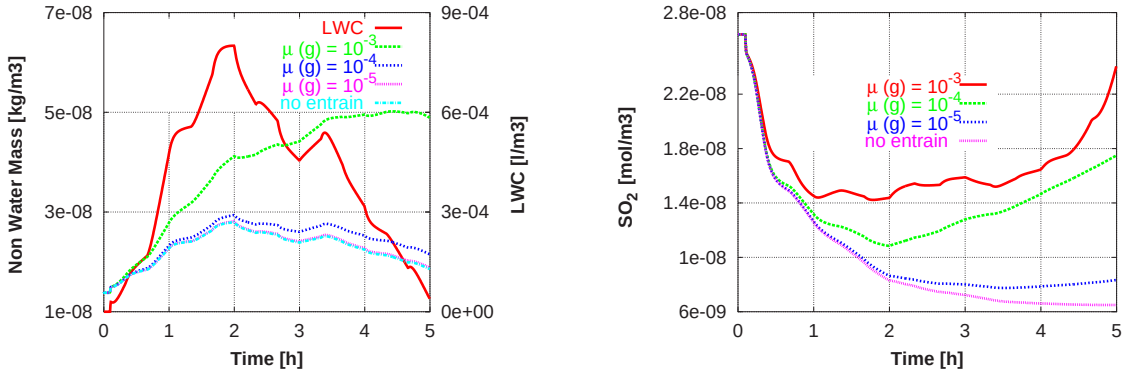

Figure 8.8: Influence of the gas phase entrainment rate on: Non Water Mass evolution (left), SO_2 concentration (right) during the simulation with SPACCIM .

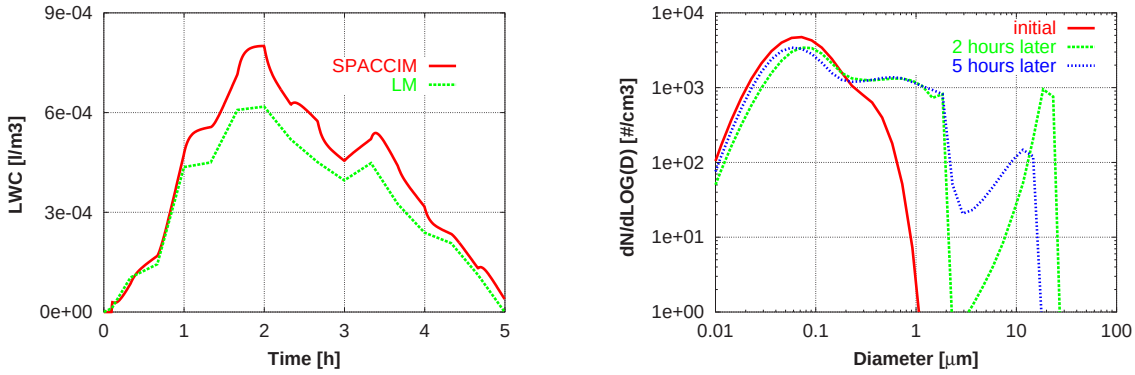

Figure 8.9: Total LWC calculated by SPACCIM compared with the one given by the forcing data from LM (left); Number size distribution evolution for three position of the air parcel simulated with SPACCIM (right).

Furthermore, MUSCAT includes a multidimensional cloud chemistry parameterizations involving the same processes described in the parcel model SPACCIM . This leads to a relative good agreement between the two approaches for aqueous phase species concentration as shown for nitrate and ammonium in Fig. 8.10. The gas phase entrainment rate of $10^{-4}s^{-1}$ constitutes again an appropriate choice.

8.6 Conclusion

Results of cloud chemistry modeling in the size-resolved parcel model SPACCIM and the 3-D chemistry-transport model LM-MUSCAT are presented. It is shown that the detailed parcel model with necessary adjustments can be used to asses and evaluate the parameterizations applied in the 3D code. The analysis of the entrainment pa-

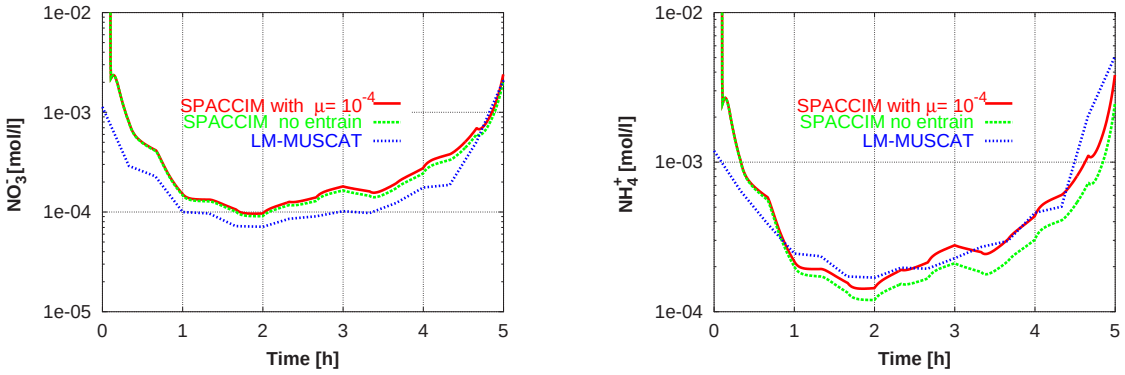

Figure 8.10: Comparison of NO_3^- and NH_4^+ molalities between SPACCIM with and without gas phase entrainment and LM-MUSCAT during the 5 hours simulations. The entrainment rate μ refers to the gas phase entrainment rate.

rameterization in SPACCIM indicates that a moderate entrainment rate of $10^{-4}s^{-1}$ for the gas phase represents a reliable value. On the other hand, entrainment of aerosol becomes significant only in the case of coagulation and sedimentation initiated by higher LWC. The results and analysis presented in this chapter needs surely more investigations. The relative good agreement between the two approaches for aqueous phase species stresses the seriousness of such a comparison study.

Chapter 9

Summary

In this thesis we have considered the coupling between a complex multiphase chemistry and a detailed microphysics in a size resolved cloud model. That constitutes a new contribution in modeling and understanding the physico-chemical processes in the atmosphere. The size resolved multiphase chemistry model involves reactions in the gas and aqueous phase including dissociation and phase transfer. The size resolved microphysical model is based on the discretization in mass space of the general dynamic equation (GDE) governing the processes undergone by a population of aerosols (droplets) using a linear discrete method (LDM) with an explicit description of activation. Moreover, a new descritization method based on the Discontinuous Galerkin Method (DGM) was presented and tested for the one component and multicomponent systems with satisfactory results.

The main target of this work has been to develop, implement and test a coupling strategy between a microphysicsal and a multiphase chemistry models that were designed to simulate processes evolving in different space and time scales. Meanwhile, a huge number of problems and difficulties appeared and had to be solved. That allowed us a better understanding of some processes , the way they interact and to figure out the quality of their parametrizations.
The coupling scheme is inspired from the first order operator splitting and source splitting techniques. It provides time-interpolated values of the meteorological variables (temperature, water vapor, liquid water content) and generates time-averaged mass fluxes T over a defined coupling time interval for chemistry. The changes in the chemical aerosol composition by gas scavenging and the chemical reactions feed back on the microphysical processes (e.g., water condensation growth rates via changes in surface tension and the Raoult term). The resulting ODEs are large non-linear and extremely stiff. For solving this system, implicit time integration schemes are required. Indeed, the numerical scheme used is based on the high order multistep backward differentiation formula (BDF) with a Newton like corrector iteration. The

resulting linear systems are solved by direct sparse solvers exploiting the sparsity and the block structure of the Jacobian matrix. In order to improve the efficiency of the direct sparse solvers, an approximate matrix factorization is utilized at the linear algebra level.

In the aim of testing the coupled model, various case studies were simulated inspired from field experiment and literature and self developed ones. The first case studies were aimed to investigate some features and parameter setups of the coupled model from a numerical point of view. This sensitivity study is performed in order to determine "optimal" control parameters without significant loss of accuracy. Comparison with measured value during the FEBUKO field experiment showed a good agreement and proofed that the coupling strategy is robust and reliable. Moreover, we have shown that the developed model simulates chemical mechanisms of different complexity with high flexibility. Simulations involving simple inorganic mechanisms like INORG and complex ones from the CAPRAM family were carried out. The sensitivity of the model to the degree of description of targeted reacting pathways was demonstrated. The effect of feeding back the chemical composition to microphysics in order to compute a more realistic growing term during the condensation process was likewise investigated. The coupling time step Δt_{cpl} is a key control parameter in SPACCIM. It has an influence on chemistry, numerics and also on microphysics when considering feedback. For the simulated scenarios, a coupling time step of 10 s is reasonable and gives satisfactory results. Furthermore, under the conditions of a relative monotone liquid water content evolution, the control of the coupling time step is possible and bring substantial computing gain with negligible loss of accuracy. Coarser resolutions RESCHEM for multiphase chemistry calculations reduce the dimension of the system and, consequently, the numerical costs. The use of RESCHEM = 2 is a good compromise between the loss of accuracy and the numerical gain.
In the present work a special attention has been paid for the time integration scheme. Especially, the approximate matrix factorization was investigated. We figured out that the order in the AMF can become important under some microphysical conditions. The deviations between the numerical efficiencies of AMF (5.7), (5.10) and (5.11) become substantial during the "monotone" RISING scenario.
Additionally, another popular numerical scheme is involved in the present work namely the second order non-autonomous Rosenbrook method. Under realistic conditions and for complex multiphase reacting mechanisms, it is shown that the sparse techniques based on the BDF scheme are more efficient than the ones based on ROS2.

The evaluation of the uncertainties due to the "splitting" between microphysics and multiphase chemistry in comparison with a fully coupled model and those concerning the use of the two representations "fixed bin" and "moving bin" is achieved. For that, six different approaches are compared and discussed for four scenarios derived from field measurements. The study focuses on the effects of different mi-

crophysical and numerical approaches on the multiphase chemistry. The interaction between numerical schemes, microphysics and multiphase chemistry is discussed for three chemical reaction schemes of different complexity. It is shown that the simulation results of the participating models agree in an appreciable way mostly. Observable differences are noticed between the "moving bin" approach and models using fixed grids for the discretization of the particle/droplet spectrum. Furthermore, the initial aerosol composition influences the fate of chemical species as well as the behavior of the numerical solver in a substantial way. The loss of accuracy due to the use of "splitting" between microphysics and multiphase chemistry in the case of SPACCIM approach is not significant in comparison with the fully coupled approach in GALERKIN.

Obviously, the performance of the parcel model SPACCIM had to be established for scenarios involving not only orographic cloud events but also other cloud types where coagulation can constitute an important process. For that aim, realistic calculations delivered by the 3D mesoscale model LM are used as off-line forcing data for the parcel model. It is shown that the parametrization developed for the entrainment/detrainment process gives reasonable results and is reliable.
The parcel models are known to be a powerful tool to simulate detailed local events and to test theoretical approaches and parametrizations. In air pollution modeling, their importance rises with the complexity reached by 3D models. Comparison of the results given by the parcel model SPACCIM driven by off-line forcing data delivered by the LM-MUSCAT system inside a certain domain and the ones simulated by LM-MUSCAT using complex multiphase reacting mechanisms demonstrates the seriousness of such an approach.

The above discussed issues highlight the capability of the coupled model to handle different microphysical approaches and to deal with different reacting mechanisms under various types of dynamics using implicit time integration schemes with high flexibility.

Appendix A

A.1 Reactions rates calculation

Here the reaction rate formulas for forward reaction types in gas and aqueous phase are presented.

Photolysis:

The reaction rates are of the form $k = A \exp y$, where $y = B\ [1 - \frac{1}{\cos z}]$ and $z = e\ C$. The parameter e represents the zenith angle in radian and A,B and C represent the parameters of the reaction. The rate of aqueous photolysis reactions have to be corrected due to cloud scattering effect.

Temperature dependent reactions:

First form:
Reaction rates are $k = k_{298}\ exp[-\frac{E_A}{R}(\frac{1}{T})]$

Second form:
Reaction rates are $k = k_{298}\ T^2\ exp[-\frac{E_A}{R}(\frac{1}{T})]$

Third form:
Reaction rates are $k = k_{298}\ exp[-\frac{E_A}{R}(\frac{1}{T} - \frac{1}{298}]$

Special reactions in the gas phase:

Pressure dependent reactions (TROE in RACM):
Reaction rates are of the form

$$k = \frac{k_1}{1 + \frac{k_1}{k_2}}\ 0.6^{\frac{1}{(1+(\log_{10}\frac{k_1}{k_2}))^2}}$$

where $k_1 = M_{air}\ k_{298}\ (\frac{T}{300})^{-N}$ and $k_2 = k_{inf}\ (\frac{T}{300})^{-M}$. M_{air} represents the molar mass of air. k_{298}, k_{inf}, N and M are the parameters of the reaction.

Equilibrium pressure dependent reactions (TROEQ in RACM):
Reaction rates are of the form
$k = \frac{k_3}{k_{298}\ exp[-B\ \frac{1}{T}]}$ where $k_3 = \frac{k_1}{1+\frac{k_1}{k_2}}\ 0.6^{\frac{1}{(1+(\log_{10}\frac{k_1}{k_2}))^2}}$, $k_1 = M_{air}\ k_{298}\ (\frac{T}{300})^{-N}$ and $k_2 = k_{inf}\ (\frac{T}{300})^{-M}$. M_{air} represents the molar mass of air. k_{298}, k_{inf}, N and M are the parameters of the reaction.

Density dependent reactions (SPEC1 in RACM):
Reaction rates are of the form
$k = C_1\ [1 + M_{air}\ C_2]$ where C_1 and C_2 are the parameters of the reaction.

Density dependent reactions (SPEC2 in RACM):
Reaction rates are of the form
$k = M_{air}\ C_1\ (\frac{T}{300})^{C_2}$ where C_1 and C_2 are the parameters of the reaction.

Density dependent reactions (SPEC3 in RACM):
Reaction rates are of the form
$k = k_A + \frac{k_B}{(1+\frac{k_B}{k_C})}$ where $k_A = k_1\ \exp(\frac{k_2}{T})$, $k_B = k_3\ \exp(\frac{k_4}{T})$ and $k_C = M_{air}\ k_5\ \exp(\frac{k_6}{T})$ are the parameters of the reaction. The other constants are given by $k_1 = 7.25\ 10^{-15}$, $k_2 = 785.$, $k_3 = 4.1\ 10^{-16}$, $k_4 = 1440.$, $k_5 = 1.9\ 10^{-33}$ and $k_6 = 725.$

Density dependent reactions (SPEC4 in RACM):
Reaction rates are of the form
$k = C_1\ \exp\frac{C_2}{T} + M_{air}\ C_3\ \exp\frac{C_4}{T}$. C_1, C_2, C_3 and C_4 are the parameters of the reaction.

Special reactions in the aqueous phase:

pH dependent reactions (first form):
Reaction rates are $k = [H^+]k_{298}\ exp[-\frac{E_A}{R}(\frac{1}{T} - \frac{1}{298})]$.

pH dependent reactions (second form):
Reaction rates are $k = [H^+]^B k_{298}\ exp[-\frac{E_A}{R}(\frac{1}{T} - \frac{1}{298})]$.

A.2 Prechem

PreChem is a preprocessor for converting a multiphase chemical mechanism into input-data for the multiphase parcel model. In the following, an example of the preprocessor input file is given

```
#  ==================   Unit options   =====================
UNIT GAS   0  #  Gas phase units     (0 = molec/cm3, 1 = mol/m3)
UNIT AQUA  0  #  Aqueous phase units (0 = mol/l)
#  ==================   Gas Phase      =====================
CLASS: GAS
NO2           =     O3PX   +   NO
PHOTABC:  A: 7.67e-03  B: 1.773179e-00  C:  0.77233e-00
CLASS: GAS
O3  +  NO   =  NO2   + [O2]
TEMP1:   KO:  2.00E-12  E/R:  1400.0
#  ==================   Phase Transfer  =====================
CLASS: HENRY
O3 = aO3
TEMP3:   A: 1.1e-2  B: 2300.0
CLASS: HENRY
H2O2 = aH2O2
TEMP3:   A: 1.0e5  B: 6340.0
#  ==================   Liquid Phase    =====================
CLASS: AQUA
HSO3m  + aH2O2 +  Hp = SO4mm  + 2 Hp + [aH2O]
TEMP3:   A: 6.9e7  B: -4000.0
CLASS: AQUA
aSO2  + aO3  = HSO4m   + Hp + aO2 - [aH2O]
TEMP3:   A: 2.4e4 B: 0.0
CLASS: AQUA
HSO3m  + aO3  = SO4mm  + Hp  + aO2
TEMP3:   A: 3.7e5 B: 0.0
#  ==================   Dissociation    =====================
CLASS: DISS
aHNO3         =    NO3m + Hp
DTEMP:   A: 22.0  B: 1800.0  C: 5.0e10
CLASS: DISS
aSULF = HSO4m + Hp
DCONST:  A:  1000.0  B: 5e10
CLASS: DISS
HSO4m = Hp + SO4mm
DTEMP:  A: 1.02e-2  B: -2700.0 C: 1e11
```

Every reaction is defined by its class and its type and is interpreted according to a proper syntax convention. Four reaction classes are considered: GAS, HENRY, DISS, and AQUA referring to gas phase, Henry equilibrium, dissociation and aqueous phase reactions respectively. The type of the reactions refers to the way the reaction rate is calculated as presented in the previous section.

Reactions are defined through the stoichiometric constants and through the kinetics characterizing every reaction kind (i.e., the parameters needed to calculate the reaction rate constants). These are delivered by PreChem as an output file.
Among other informations, the core of the output for the previous input is listed as

```
  ======================  Reactions   ========================

#----------- 1. Reaction ------ Input index 1 ------
GAS   PHOTABC
1 2 1 2
3 5 2 3
2 1.000000e+00 3 -1.000000e+00 5 1.000000e+00
3  7.670000e-03 1.773179e+00 7.723300e-01
#----------- 2. Reaction ------ Input index 2 ------
GAS   TEMP1
2 2 2 1
4 2 3 1 3
2 -1.000000e+00 3 1.000000e+00 4 -1.000000e+00
2  2.000000e-12 1.400000e+03
#----------- 3. Reaction ------ Input index 1 ------
HENRY   TEMP3
1 1 1 1
4 8 2
4 -1.000000e+00 8 1.000000e+00
2  1.100000e-02 2.300000e+03
#----------- 4. Reaction ------ Input index 2 ------
HENRY   TEMP3
1 1 1 1
1 5 2
1 -1.000000e+00 5 1.000000e+00
2  1.000000e+05 6.340000e+03
#----------- 5. Reaction ------ Input index 1 ------
DISS   DTEMP
1 2 1 2
6 3 11 3
3 1.000000e+00 6 -1.000000e+00 11 1.000000e+00
3  2.200000e+01 1.800000e+03 5.000000e+10
#----------- 6. Reaction ------ Input index 2 ------
DISS   DCONST
1 2 1 2
10 2 11 3
2 1.000000e+00 10 -1.000000e+00 11 1.000000e+00
2  1.000000e+03 5.000000e+10
#----------- 7. Reaction ------ Input index 3 ------
DISS   DTEMP
1 2 1 2
2 11 4 3
2 -1.000000e+00 4 1.000000e+00 11 1.000000e+00
3  1.020000e-02 -2.700000e+03 1.000000e+11
```

```
#----------- 8. Reaction ------ Input index 1 ------
AQUA   TEMP3
3 3 3 2
1 5 11 4 11 2 4
1 -1.000000e+00 4 1.000000e+00 5 -1.000000e+00 11 1.000000e+00
2  6.900000e+07 -4.000000e+03
#----------- 9. Reaction ------ Input index 2 ------
AQUA   CONST
2 4 2 3
9 8 2 11 7 2 5
2 1.000000e+00 7 1.000000e+00 8 -1.000000e+00 9 -1.000000e+00 11 1.000000e+00
1  2.400000e+04
#----------- 10. Reaction ------ Input index 3 ------
AQUA   CONST
2 3 2 3
1 8 4 11 7 5
1 -1.000000e+00 4 1.000000e+00 7 1.000000e+00 8 -1.000000e+00 11 1.000000e+00
1  3.700000e+05
```

Species names are allowed to occur in alphabetical, appearance or prescribed orders. The corresponding values of species physical parameters like the accommodation coefficient, the molar mass, solubility and diffusion coefficients for gas phase are given in a separated data file (see B.1).

Appendix B

B.1 Constants for species considered in mass transfer

The constants for species involved in mass transfer process in RACM mechanism are given in the following

Spieces	Molar mass [g/mol]	Accomodation coef. (α)	Diffusion coef. (Dg)
ACO3	75.0	0.019	0.00001
ALD	44.0	0.03	0.0000122
Br_2	160.0	0.08	0.00001
CH_3OH	32.0	0.0271	0.0000116
CH4	16.0	5.0e-5	0.0000141
Cl_2	71.0	0.08	0.0000128
CO_2	44.0	1.5e-4	0.0000155
ETE	28.0	1.0e-4	0.0000101
ETEPX	77.0	8.2e-3	0.0000082
ETH	30.0	1.0e-4	0.0000095
ETHPX	61.0	8.2e-3	0.0000108
ETOH	46.0	0.0176	0.0000095
GLY	58.0	0.023	0.0000115
H_2O_2	34.0	0.1532	0.0000146
HCHO	30.0	0.02	0.0000164
HCl	36.0	0.1158	0.0000189
HNO_3	63.0	0.0868	0.0000132
HNO_4	79.0	0.1	0.0000130

(continuation)

Spieces	Molar mass [g/mol]	Accomodation coef. (α)	Diffusion coef. (Dg)
HO	17.0	0.05	0.0000153
HO_2	33.0	0.01	0.0000104
HONO	47.0	0.05	0.000013
MO2	47.0	6.7581e-3	0.0000135
N_2O_5	108.0	0.018	0.000011
NH_3	17.0	0.091	0.000023
NO	30.0	0.001	0.0000224
NO_2	46.0	1.5e-3	0.0000192
NO_3	62.0	4.0e-3	0.00001
HCHO	30.0	0.02	0.0000164
HCl	36.0	0.1158	0.0000189
HNO_3	63.0	0.0868	0.0000132
HNO_4	79.0	0.1	0.0000130
HO	17.0	0.05	0.0000153
HO_2	33.0	0.01	0.0000104
HONO	47.0	0.05	0.000013
MO2	47.0	6.7581e-3	0.0000135
N_2O_5	108.0	0.018	0.000011
NH_3	17.0	0.091	0.000023
NO	30.0	0.001	0.0000224
NO_2	46.0	1.5e-3	0.0000192
NO_3	62.0	4.0e-3	0.00001
O_3	48.0	0.1	0.0000148
OP1	48.0	6.7581e-3	0.0000131
OP2	62.0	0.01	0.0000076
ORA1	46.0	2.29e-2	0.0000153
ORA2	60.0	3.22e-2	0.0000124
PAA	76.0	1.9e-2	0.0000102
PAN	121.0	0.019	0.0000063
SO_2	64.0	0.11	0.0000128
SULF	98.0	0.12	0.000013
(O_2)	32.0	0.1	0.0000112

B.2 RISING and WAVE initial data

Initial gas phase concentration

Species	Concentration [molec/cm^3]	Species	Concentration [molec/cm^3]
SO_2	1.81e+10	HC5	2.45e+10
CO	7.34e+12	HC8	2.45e+09
NO	1.89e+10	ETE	2.47e+10
NO_2	2.16e+11	OLT	2.45e+09
O_3	4.13e+11	TOL	6.92e+10
HONO	2.86e+09	CSL	2.45e+07
HNO_3	2.75e+09	XYL	5.87e+10
ORA1	4.40e+09	PAN	1.22e+10
ORA2	6.29e+09	OP1	2.45e+10
GLY	6.36e+08	OP2	2.45e+09
MGLY	8.81e+08	PAA	2.45e+07
ALD	3.41e+10	NH_3	2.45e+10
MACR	1.88e+09	HCl	4.89e+09
KET	2.06e+10	CH_3OH	1.22e+11
HKET	5.87e+08	ETOH	2.45e+10
H_2O_2	2.45e+08	API	9.78e+08
HCH0	2.86e+10	LIMN	4.89e+08
H_2	1.22e+13	ISO	1.30e+10
CH_4	4.16e+13	[H_2O]	4.89e+17
CO_2	8.73e+15	[O2]	4.89e+18
ETH	3.40e+10	[N2]	1.91e+19
HC3	4.89e+10	-	-

Parameters of the initial aerosol distribution

Modes	Number [mg^{-1}]	Radius [nm]	Geom σ
First mode	2971.5	34	1.86
Second mode	161.1	167.5	1.39

Composition of the initial aerosol distribution

Species	Molar mass [g/mol]	First mode [g/g]	Second mode [g/g]
SO_4^{2-}	96.00	5.99522e-2	1.62205e-1
NO_3^-	62.00	9.70520e-3	4.33233e-1
NO_2^-	46.00	6.44347e-3	5.65258e-3
Cl^-	35.50	0.00000e+0	7.54111e-3
NH_4^+	18.00	3.32982e-2	8.91392e-2
Mn^{3+}	55.00	5.31060e-5	4.65870e-5
Fe^{3+}	56.00	2.64820e-4	2.32315e-4
Cu^{2+}	63.50	2.11714e-4	1.85728e-4
Na^+	23.00	0.00000e+0	5.24309e-4
K^+	39.00	3.93256e-3	4.01641e-3
Ca^{2+}	40.00	6.29720e-4	3.33050e-4
Zn^{2+}	65.00	5.82745e-4	5.11217e-4
$C_2O_4^{2-}$	88.00	3.07109e-3	3.40404e-3
$WSOC^-$	121.50	1.41869e-3	7.38041e-3
aWSOC	100.00	1.27109e-1	6.80049e-2
sWISOC	250.00	8.01933e-2	4.80122e-2
sEC	12.00	1.02812e-1	4.72648e-2
sUNSOL	61.00	5.70322e-1	1.22313e-1

$WSOC^-$ is the representing element for the ionic water soluble organic compounds. aWSOC and sWISOC stand for non-ionic water soluble organic compounds and non-soluble organic compounds, respectively. sEC is the non-soluble black carbon and sUNSOL represents the rest measured non-soluble material.

B.3 FEBUKO simulation initial data

Species	Concentration [molec/cm^3]	Species	Concentration [molec/cm^3]
SO_2	1.81e+10	HC5	3.03e+11
CO	7.34e+12	HC8	9.30e+09
NO	1.89e+10	ETE	2.47e+10
NO_2	2.16e+11	OLT	2.96e+10
O_3	4.13e+11	TOL	9.85e+10
HONO	2.86e+09	CSL	2.45e+07
HNO_3	2.75e+09	XYL	5.87e+10
ORA1	4.40e+09	PAN	1.23e+10
ORA2	6.29e+09	OP1	2.45e+10
GLY	6.36e+08	OP2	2.45e+09
MGLY	8.81e+08	PAA	2.45e+07
ALD	3.60e+10	NH_3	2.45e+10
MACR	1.88e+09	HCL	1.23e+08
KET	2.06e+10	CH_3OH	1.22e+11
HKET	5.87e+08	ETOH	2.45e+10
H_2O_2	9.26e+08	API	9.78e+08
HCH0	2.86e+10	LIMN	4.89e+08
H_2	1.22e+13	ISO	1.30e+10
CH_4	4.16e+13	[H_2O]	4.89e+17
CO_2	8.73e+15	[O2]	4.89e+18
ETH	3.40e+10	[N2]	1.91e+19
HC3	4.39e+11	-	-

Composition of the initial aerosol distribution

The initial aerosol composition is directly derived from the measured one. The measure technique rest on the use of five different impactor stages collectors aimed to capture particles mass in all size ranges. The size limits of the impactor stages in meter are successively
18.87e-9 52.83e-9 156.57e-9 430.77e-9 1224.50e-9 3498.56e-9.
sizes $<$ 18.87e-9 and $>$ 3498.56e-9 are classified in the first and fifth impactor stages respectively. The subtraction of water fractions allows to make the transformation from aerodynamic to geometric diameters. The impactor stages are given in [g/g].

Spieces	Molar mass [g/mol]	Impact 1	Impact 2	Impact 3	Impact 4	Impact 5
aWSOC	100.0	0.127109444	0.085094494	0.068004857	0.093935903	0.211880145
sWISOC	250.0	0.080193272	0.057375242	0.048012236	0.062378992	0.131876838
sEC	12.0	0.102811887	0.105923523	0.047264793	0.061517743	0.072459801
SO_4^{2-}	96.0	0.059952182	0.143982433	0.162205074	0.046230584	0.032244612
NO_3^-	62.0	0.009705196	0.247710643	0.433233409	0.296488485	0.199176399
NO_2^-	46.0	0.006443473	0.005717357	0.005652583	0.007329693	0.007764278
Cl^-	35.5	0.000000000	0.004089176	0.007541105	0.007192528	0.000000000
$C_2O_4^{2-}$	88.0	0.003071086	0.003506091	0.003404041	0.004549281	0.000000000
$C_3H_3O_4^-$	103.0	0.000000000	0.001032678	0.001471588	0.001638144	0.001546790
$C_4H_5O_4$	117.0	0.000196700	0.000408852	0.000657513	0.000395162	0.000442453
$C_4H_5O_4I^-$	117.0	0.000288006	0.000598637	0.000962724	0.000578591	0.000647834
$C_5H_7O_4^-$	131.0	0.000000000	0.000066983	0.000072804	0.000000000	0.000000000
$C_5H_7O_4I^-$	131.0	0.000000000	0.001668300	0.001813292	0.000000000	0.000000000
$C_3H_3O_5^-$	119.0	0.000000000	0.000286683	0.000315486	0.000000000	0.000000000
$C_4H_5O_5^-$	133.0	0.000663496	0.000585923	0.000719819	0.000712233	0.001570122
$C_4H_5O_6^-$	149.0	0.000000000	0.000347860	0.000366331	0.000000000	0.000000000
$C_5H_7O_5^-$	147.0	0.000000000	0.000000000	0.000183736	0.000000000	0.000000000
$C_4H_3O_4^-$	115.0	0.000000000	0.000317738	0.000579834	0.000248524	0.000000000
$C_8H_14O_4^-$	174.0	0.000111876	0.000099268	0.000098144	0.000127263	0.000134808
$C_9H_16O_4^-$	188.0	0.000158609	0.000140735	0.000139141	0.000180423	0.000191121
NH_4^+	18.0	0.033298200	0.096043212	0.089139201	0.072443295	0.022897297
Mn^{3+}	55.0	0.000053106	0.000047121	0.000046587	0.000060410	0.000063991
Fe^{3+}	56.0	0.000264820	0.000234977	0.000232315	0.000301242	0.000319103
Cu^{2+}	63.5	0.000211714	0.000187856	0.000185728	0.000240833	0.000255112
Na^+	23.0	0.000000000	0.000350136	0.000524309	0.040989272	0.054900376
K^+	39.0	0.003932555	0.005764005	0.004016408	0.006280962	0.007439206
Ca^{2+}	40.0	0.000629723	0.000000000	0.000198952	0.016628246	0.049514198
Mg^{2+}	24.0	0.000000000	0.000000000	0.000134100	0.006520881	0.013670749
Al^{3+}	27.0	0.000000000	0.000000000	0.000000000	0.000000000	0.000000000
Zn^{2+}	65.0	0.000582745	0.000517075	0.000511217	0.000662894	0.000702198
sUNSOL	1.0	0.570321914	0.237903001	0.122312673	0.272368415	0.190302568

Parameters of the initial aerosol distribution

Modes	Number [mg^{-1}]	Radius [nm]	Geom σ
First mode	47.8	3.9	1.32
second mode	2971.5	34.	1.86
Third mode	161.1	167.5	1.39
Coarse mode	0.5	625.	1.5

Appendix C

C.1 INORG mechanism

The gas phase reacting system is RACM (Stockwell et al., 1997).

Aqueous Phase Reactions

Number	Reaction	k_{298}	$-\frac{E_A}{R}$
A(1)	$HSO_3^- + H_2O_2 + H^+ \rightarrow SO_4^{2-} + 2H^+ + H_2O$	6.9×10^7	-4000.
A(2)	$SO_2 + O_3 \rightarrow HSO_4^- + H^+ + O_2$ - H_2O	2.4×10^4	0.
A(3)	$HSO_3^- + O_3 \rightarrow SO_4^{2-} + H^+ + O_2$	3.7×10^5	0.
A(4)	$SO_3^{2-} + O_3 \rightarrow SO_4^{2-} + O_2$	1.5×10^9	-5280.

Reaction rates are of the form $k = k_{298} exp[-\frac{E_A}{R}(\frac{1}{T} - \frac{1}{298})]$.

Henry's law equilibria

Number	Reaction	k_{298}	$-\frac{\Delta H}{R}$
E(1)	$O_3(g) \rightleftharpoons O_3(aq)$	1.1×10^{-2}	2300.
E(2)	$H_2O_2(g) \rightleftharpoons H_2O_2(aq)$	1.0×10^5	2300.
E(3)	$NH_3(g) \rightleftharpoons NH_3(aq)$	60.7	3920.
E(4)	$HCL(g) \rightleftharpoons HCL(aq)$	1.1	2020.
E(5)	$HNO_3(g) \rightleftharpoons HNO_3(aq)$	2.1×10^5	8700.
E(6)	$CO_2(g) \rightleftharpoons CO_2(aq)$	3.1×10^{-2}	2423.
E(7)	$SO_2(g) \rightleftharpoons SO_2(aq)$	1.24	3300.
E(8)	$H_2SO_4(g) \rightleftharpoons H_2SO_4(aq)$	1.1×10^{-2}	2300.

Reaction rates are of the form $k = k_{298} exp[-\frac{\Delta H}{R}(\frac{1}{T} - \frac{1}{298})]$.

Dissociation equilibria

Number	Reaction	A	B	C
E(9)	$H_2SO_4(aq) \rightleftharpoons HSO_4^- + H^+$	1000.	0.	$5.\times 10^{10}$.
E(10)	$NH_3(aq) + H_2O \rightleftharpoons NH_4^+ + OH\_$	$3.17 \times 10\_{-7}$	-560.	3.47×10^{10}
E(11)	$HCL(aq) \rightleftharpoons Cl^- + H^+$	1.72×10^6	6890.	2.9×10^5
E(12)	$HNO_3(aq) \rightleftharpoons NO_3 + H^+$	22.	1800.	5.0×10^{10}
E(13)	$CO_2(aq) \rightleftharpoons HCO_3 + H^+$	4.3×10^{-7}	-913.	5.6×10^4
E(14)	$HCO_3^-(aq) \rightleftharpoons CO_3^{2-} + H^+$	$4.7 \times 10\_{-11}$	-1820.	$5. \times 10^{10}$
E(15)	$SO_2(aq) + H_2O \rightleftharpoons HSO_3^- + H^+$	$3.15 \times 10\_{-4}$	1940.	$2. \times 10^8$
E(16)	$HSO_3^-(aq) \rightleftharpoons SO_3^{2-} + H^+$	$6.22 \times 10\_{-8}$	1960.	$5. \times 10^{10}$
E(16)	$HSO_4^-(aq) \rightleftharpoons SO_4^{2-} + H^+$	$1.02 \times 10\_{-2}$	-2700.	$1. \times 10^{11}$

C.2 BARTH mechanism

In the sulfur free mechanism (Barth et al., 2003), called BARTH here, the gas phase reacting system was replaced by RACM (Stockwell et al., 1997).

Aqueous Phase Reactions (Photolysis)

Number	Reaction	A	B	C
A(1)	$O_3 + h\nu + H_2O \rightarrow H_2O_2 + O_2$	3.83×10^{-5}	4.11188	7.7335×10^{-1}
A(2)	$H_2O_2 + h\nu \rightarrow 2OH$	11.47×10^{-6}	2.35766	7.6470×10^{-1}

The aqueous phase reacting system was slightly modified and adapted to the intercomparison study. Thus, the photoloysis rates were not kept constant, but replaced by the corresponding zenith angle dependent ones from the gas phase increased by a factor of 1.5. To ensure the electroneutrality reactions ($A13$) and ($A17$) in the original mechanism were replaced by

$$O_3 + OH \rightarrow HO_2 + O_2$$
$$HCO_3^- + O_2^- \rightarrow CO_3^- + HO_2^-$$

N_2O_5 phase transfer reaction ($E12$) was replaced by

$$N_2O_5 \rightarrow N_2O_5(aq) \qquad k_{298} = 1.4$$
$$N_2O_5(aq) \rightarrow 2\ H^+ + 2\ NO_3^- \qquad k_{298} = 5.0 \times 10^9 \qquad \frac{E_A}{R} = -1800.$$

H_2O_2 dissociation reaction ($E15$) was replaced by the forward reaction with the corresponding rate due to the presence of reaction ($A10$) in the aqueous phase.

$$H_2O_2(aq) \rightarrow HO_2^- + H^+ \qquad k_{298} = 11.0 \times 10^{-2} \qquad \frac{E_A}{R} = -5200.$$

Reactions rates are of the form $k = k_{298}\ exp[-\frac{E_A}{R}(\frac{1}{298} - \frac{1}{T})]$.

Aqueous Phase Reactions

Number	Reaction	k_{298}	$-\frac{E_A}{R}$
A(3)	$CH_2(OH)_2 + OH + O_2 \rightarrow HCOOH + HO_2 + H_2O$	2.0×10^9	-1500.
A(4)	$HCOOH + OH + O_2 \rightarrow CO_2 + HO_2 + H_2O$	1.6×10^8	-1500.
A(5)	$HCOO^- + OH + O_2 \rightarrow CO_2 + HO_2 + OH^-$	2.5×10^9	-1500.
A(6)	$CH_3OO + O_2^- + H_2O \rightarrow CH_3OOH + OH^- + O_2$	5.0×10^7	-1600.
A(7)	$CH_3OOH + OH \rightarrow CH_3OO + H_2O$	2.7×10^7	-1700.
A(8)	$CH_3OOH + OH \rightarrow CH_2(OH)_2 + OH$	1.9×10^7	-1900.
A(9)	$HO_2 + O_2^- \rightarrow HO_2^- + O_2$	1.0×10^8	-1500.
A(10)	$HO_2^- + H^+ \rightarrow H_2O_2$	5.0×10^{10}	-1500.
A(11)	$OH + OH \rightarrow H_2O_2$	5.2×10^9	-1500.
A(12)	$O_3 + O_2^- + H_2O \rightarrow OH + 2O_2 + OH^-$	1.5×10^9	-1500
A(13)	$O_3 + OH \rightarrow HO_2 + O_2$	3.0×10^9	-1500
A(14)	$H_2O_2 + OH \rightarrow HO_2 + H_2O$	2.7×10^7	-1700
A(15)	$OH + O_2^- \rightarrow OH^- + O_2$	1.0×10^{10}	-1500.
A(16)	$HCO_3^- + OH \rightarrow CO_3^- + H_2O$	1.0×10^7	-1500.
A(17)	$HCO_3^- + O_2^- \rightarrow CO_3^- + HO_2^-$	1.5×10^6	-1500.
A(18)	$CO_3^- + H_2O_2 \rightarrow HCO_3^- + HO_2$	8.0×10^5	-2800.
A(19)	$CO_3^- + O_2^- \rightarrow HCO_3^- + O_2 + OH^-$	4.0×10^8	-1500.
A(20)	$HO_2 + Cl_2^- \rightarrow 2Cl^- + O_2 + H^+$	4.5×10^9	-1500.
A(21)	$O_2^- + Cl_2^- \rightarrow 2Cl^- + O_2$	1.0×10^9	-1500.
A(22)	$H_2O_2 + Cl_2^- \rightarrow 2Cl^- + HO_2 + H^+$	1.4×10^5	-3400.
A(23)	$H_2O_2 + Cl \rightarrow Cl^- + HO_2 + H^+$	4.5×10^7	0.
A(24)	$NO_3 + Cl^- \rightarrow NO_3^- + Cl$	1.0×10^8	-1500.
A(25)	$NO_3 + O_2^- \rightarrow NO_3^- + O_2$	1.0×10^9	-1500.
A(26)	$N_2O_5 + H_2O \rightarrow 2H^+ + 2NO_3^-$	$5. \times 10^9$	-1800.

Reaction rates are of the form $k = k_{298} exp[-\frac{E_A}{R}(\frac{1}{T} - \frac{1}{298})]$.

Henry's law equilibria

Number	Reaction	k_{298}	$-\frac{\Delta H}{R}$
E(1)	$O_3(g) \rightleftharpoons O_3(aq)$	1.1×10^{-2}	2300.
E(2)	$H_2O_2(g) \rightleftharpoons H_2O_2(aq)$	8.3×10^{4}	7400.
E(3)	$OH(g) \rightleftharpoons OH(aq)$	30.	4500.
E(4)	$HO_2(g) \rightleftharpoons HO_2(aq)$	$4. \times 10^{3}$	5900.
E(5)	$CH_3OO(g) \rightleftharpoons CH_3OO(aq)$	15.	5600.
E(6)	$CH_3OOH(g) \rightleftharpoons CH_3OOH(aq)$	3.1×10^{2}	5200.
E(7)	$CH_2O(g) \rightleftharpoons CH(OH)_2(aq)$	3.2×10^{3}	6800.
E(8)	$HCOOH(g) \rightleftharpoons HCOOH(aq)$	5.4×10^{3}	5700.
E(9)	$NO(g) \rightleftharpoons NO(aq)$	1.9×10^{-3}	1500.
E(10)	$NO_2(g) \rightleftharpoons NO_2(aq)$	6.4×10^{-3}	2500.
E(11)	$HNO_3(g) \rightleftharpoons HNO_3(aq)$	2.4×10^{6}	8700.
E(12)	$N_2O_5(g) \rightarrow N_2O_5(aq)$	1.4	0.
E(13)	$NO_3(g) \rightleftharpoons NO_3(aq)$	1.8	2000.
E(14)	$CO_2(g) \rightleftharpoons CO_2(aq)$	3.6×10^{-2}	2200.

Reaction rates are of the form $k = k_{298} exp[-\frac{\Delta H}{R}(\frac{1}{T} - \frac{1}{298})]$.

Dissociation equilibria

Number	Reaction	A	B	C
E(16)	$H_2O_2(aq) \rightarrow HO_2^- + H^+$	$11. \times 10^{-2}$	0.	-5200.
E(17)	$HO_2(aq) \rightleftharpoons O_2^- + H^+$	3.5×10^{-5}	0.	$5. \times 10^{10}$
E(18)	$HCOOH(aq) \rightleftharpoons HCOO^- + H^+$	1.8×10^{-4}	-1500.	$5. \times 10^{10}$
E(19)	$HNO_3(aq) \rightleftharpoons NO_3 + H^+$	15.	0.	$5. \times 10^{10}$
E(20)	$CO_2(aq) \rightleftharpoons HCO_3 + H^+$	4.5×10^{-7}	-1000.	5.6×10^{4}
E(21)	$Cl_2^-(aq) \rightleftharpoons Cl^- + Cl(aq)$	5.3×10^{-6}	0.	$6. \times 10^{4}$

C.3 CAPRAM mechanisms

The aqueous phase reacting mechanism CAPRAM2.3 (Chemical Aqueous Phase RAdical Mechanism, Hermann et al., 2000) contains an explicit description of aqueous phase chemical transformation of tropospheric constituants initiated by primary radicals and secondary radical anions such as OH, NO_3, SO_4^-, Cl_2^-,Br_2^- or CO_3^-. In addition, a module of halogen activation is also included. Apart from that, CAPRAM2.3 considers organic compounds up to two carbon atoms. Starting from the alcohols, methanol and ethanol, the aldehydes and acids are produced. The gas phase in CAPRAM2.3 is described by RACM.
The CAPRAM2.4 version (Ervens et al., 2003) is based on the former version 2.3 and contains extended organic and transition metal chemistry and is formulated more explicitly based on a critical review of the literature. A reduced version of CAPRAM2.4 is also available. Here the ability of a simpler mechanism to reproduce concentration levels of selected target species (i.e. NO_x, S(IV), H_2O_2, NO_3, OH, O_3 and H^+) within the limits of $\pm$ 5 % was used to eliminate unimportant reactions from the complete CAPRAM2.4 scheme.
The previous three version of the mechanism are available in electronic form under http://projects.tropos.de:8088/capram/
The CAPRAM3.0 mechanism is a refined version of the 2.4 version 2.4 with a particular focus on organic chemistry. The gas phase scheme was replaced by the newer gas phase mechanism RACM (Stockwell et al., 1997). The mechanism contains 261 gas phase reactions, 775 aqueous phase reactions and 51 phase transfer processes.

Bibliography

Audiffren, N.,Renard, M., Buisson, E., Chaumerliac, N., 1998. Deviation from the Henry's law equilibrium during cloud events: A numerical approach of the mass transfer between phases and its specific numerical effects. Atmospheric Research 49, 139-161.

Barth, M.C., Rasch, P.J., Kiehl, J.T., Benkovitz, C.M., Schwartz, S.E., 2000. Sulfur chemistry in the National Center for Atmospheric Research Community Climate Model: Description, evaluation, features and sensitivity to aqueous chemistry. Journal of Geophysical Research 105, 1387-1415.

Barth, M.C., Sillman, R., Hudman, R., Jacobson, M.Z., Kim, C.H., Monod, A., Liang, J., 2003. Summary of the cloud chemistry modeling intercomparison: Photochemical box model simulation. Journal of Geophysical Research 108 (D7), doi:10.1029/2002JD002673.

Bott, A., 1999. A numerical model of the cloud-topped planetary boundary layer: chemistry in marine stratus and the effects on aerosol particles. Atmospheric Environment 33, 1921–1936.

Bott, A., 2000. A flux method for the numerical solution of the stochastic collection equation: Extension to two-demensional particle distribution. Journal of Atmospheric Science 57, 284-294.

Chang, J.S., Brost, R.A., Isaksen, I.S.A., Madronich, S., Middleton, P., Stockwell, W.R., Walcek, C.J., 1987. A three-dimensional Eulerian acid deposition model: Physical concepts and formulation. Journal of Geophysical Research, 92, 14,681-14,700.

Chaumerliac, N., Leriche, M., Audiffren, N., 2000. Modeling of scavenging processes in clouds: some remaining questions about the partitioning of gases among gas and liquid phases. Atmospheric Research 53, 29-43.

Cockburn, B., 1988. An introduction to the discontinuous Galerkin method for convection dominated problems. In: Quarteroni, A. (Ed.), Advanced numerical approximation of non-linear hyperbolic equations. Springer, pp. 151-268.

Dabdub, D., Seinfeld, J.H., 1995. Extrapolation techniques used in the solution of stiff ODEs associated with chemical kinetics of air air quality models. Atmospheric Environment 29, 403-410.

Djouad, R., Sportisse, B., Audiffren, N., 2002. Numerical simulation of aqueous-phase atmospheric models: use of non-autonomous Rosenbrock method. Atmospheric Environment 36, 873-879.

Djouad, R., Sportisse, B., 2002. Partitioning techniques for reduction in chemical kinetics. APLA: an Automatic Partitioning and Lumping Algorithm. Applied Numerical Mathematics 43(4), 383-898.

Djouad, R., Michelangeli, D.V.,Gong, W., 2003. Numerical solution for atmospheric multiphase models: Testing the validity of equilibrium assumtions. Journal of Geophysical Research 108 (D19), 4602-4614, doi:10.1029/2002JD002202.

Doms, G., Schättler, U. 1999. The Nonhydrostatic Limited-Area Model *LM* (Lokal Model) of DWD: I. Scientific Documentation (Version *LM*-F90 1.35). German Weather Service, Offenbach.

Ervens, B., George, C., Williams, J.E., Buxton, G.V., Salmon, G.A., Bydder, M., Wilkinson, F., Dentener, F., Mirabel, P., Wolke, R., Herrmann, H., 2002. CAPRAM2.4 (MODAC mechanism): An extended and condensed tropospheric aqueous phase mechanism and its application. Journal of Geophysical Research 108 (D14), 4426, doi:10.1029/2002JD002202.

Ervens, B., Feingold, G., Frost, G.J., Kreidenweis, S.M., 2004. A modeling study of aqueous production of dicarboxylic acids: 1. Chemical pathways and speciated organic mass production. Journal of Geophysical Research 109, D15205, doi:10.1029/2003JD004387.

Ervens, B., Feingold, G., Clegg, S.L., Kreidenweis, S.M., 2004. A modeling study of aqueous production of dicarboxylic acids: 2. Implications for cloud microphysics. Journal of Geophysical Research 109, D15206, doi:10.1029/2004JD004575.

Fahey, K.M., Pandis, S.N, 2001. Optimizing model performance: Variable size resolution in cloud chemistry modeling. Atmospheric Environment 35, 4471-4478.

Fleicher, J., Kjellström, E., Rodhe, H., Dentener, F., Lelieveld, J., Roelofs, G.J.H, 1996. Simulation of the tropospheric sulfur cycle in a global climate model. Atmospheric Environment 30, 1693-1707

Friedlander, S.K., 1977. Smoke, Dust and Haze. Wiley, New York, 317pp.

Fukuta, N., Walter, L.A., 1970. Kinetics of hydrometeor growth from a vapor-spherical model.Journal of Atmospheric Science, 27, 1160-1172.

Gelbard ,F., Seinfeld, J.H., 1980. Simulation of multicomponent aerosol dynamics. Journal of Colloid Interface Science 78, 485-501.

Gong, W., Dastoor, A.P., Bouchet, V.B., Gong, S., Makar, P.A., Moran, M.D., Pabla, B., 2003. Cloud processing of gases and aerosols in a regional air quality model (AURMAMS) and its evaluation against precipitation-chemistry data. Proceedings of thr Fifth Conference on Atmospheric Chemistry: Gases, Aerosols, and Clouds, 2.3 (CD-ROM), AMS.

Hairer, E., Wagner, G., 1991. Solving ordinary differential equations II. Stiff and differential-algebraic problems. Springer series in computational mathematics 14. Springer Verlag.

Hairer, E., Norsett, S.P., Wagner, G., 1993. Solving ordinary differential equations I. Nonstiff Problems 8. Second Revised Edition. Springer Verlag.

Hegg, D.A, 1985. The importance of liquid-phase oxidation of SO_2 in troposphere. Journal of Geophysical Research, 90, 3773-3779.

Herrmann, H., Ervens, B., Jacobi, H.W., Wolke, R., Nowacki, P., Zellner, R., 2000. CAPRAM2.3: A chemical aqueous phase radical mechanism for tropospheric chemistry. Journal of Atmospheric Chemistry 36, 231-284.

Herrmann, H., Wolke, R., Müller, K., Brüggemann, E., Gnauk, T., Barzaghi, P., Mertes, S., Lehmann, K., Massling, A., Birmili, W., Wiedensohler, A., Wieprecht, W., Acker, K., Jaeschke, W., Kramberger, H., Syrcina, B., Bächmann, K., Collett, J.L., Jr., Galgon, D., Schwirn, K., Nowak, A., van Pinxteren, D., Plewka, A., Chemnitzer, R., Rüd, C., Hofmann, D., Tilgner, A., Diehl, K., Heinold, B., Hinneburg, D., Knoth, O., Sehili, A.M., Simmel, M. Wurzler, S., Mauersberger, G., Majdik, Z., Müller, F., 2005. FEBUKO and MODMEP: Field measurements and modelling of aerosol and cloud multiphase processes. Atmospheric Environment, in press.

Herrmann, H., Tilgner, A., Barzaghi, P., Majdik, Z., Gligorovski, S., Poulain, L., Monod, A., 2005. Towards a more detailed description of tropospheric aqueous phase organic chemistry: CAPRAM 3.0. Atmospheric Environment, in press.

Hertel, O., Berkowicz, R., Christensen, J., Hov, O., 1993.Test of two numerical schemes for use in atmospheric transport-chemistry models. Atmospheric Environment, 27, 2591-2611.

Hindmarsh, A.C., 1983. Scientific Computing. Chapter ODEPACK: A Systematized Collection of ODE Solvers. North-Holland, Amsterdam, pp. 55-74.

Jacobson, M.Z., Turco, R.P., 1994. SMVGEAR: A sparse-matrix, vetorized gear code for atmospheric models. Atmospheric Environment, 28, 273-284.

Jacobson, M.,Turco, R., Jensen, E., Toon, O., 1994. Modeling coagulation among particles of different composition and size. Atmospheric Environment 28, 1327-1338.

Jacobson, M., 1999. Fundamentals of Atmospheric Modelling. Cambridge University Press.Cambdridge, UK.

Jacobson, M.Z, 2002. Analysis of aerosol interactions with numerical techniques for solving coagulation, nucleation, condensation, and reversible chemistry among multiple size distributions. Journal of Geophysical Research 107(D19),4366.

Jay, L.O., Sandu, A., Potra, F.A., Carmichael, G.R., 1997. Improved quasi-steady -state-approximation methods for atmospheric chemistry integration. SIAM. Journal of Scientific Computation, 18, 182-202.

Karypis, G., Schloegel, K., Kumar, V., 1998. ParMETIS, Parallel graph partitioning and sparse matrix ordering library. Version 2.0, University of Minnesota, 1998.

Kasten, F., 1968. Falling speed of aerosol particles. Journal of Applied Meteorologie 7, 944-947.

Knoth, O., Wolke, R., 1995. Numerical methods for the solution of large kinetic systems. Applied Numerical Mathematics 18, 211-221.

Knoth, O., Wolke, R., 1998. An explicit-implicit numerical approach for atmospheric chemistry-transport modeling. Atmospheric Environment, 32, 1785-1797.

Knoth, O., Wolke, R., 1998. Implicit-explicit Runge-Kutta methods for computing atmospheric reactive flow, Applied Numerical Mathematics, 28, 327-341.

Knoth, O., 2005. A parcel model for the combined treatment of microphysical and multiphase chemistry processes. Atmospheric Environment, in press.

Kreidenweis, S.M., Walcek, C.J., Feingold, G., Gong, W., Jacobson, M.Z., Kim, C., Liu, X., Penner, J.E., Nenes, A., Seinfeld, J.H., 2003. Mopdification of aerosol mass and size distribution due to aqueous phase SO_2 oxidation in clouds: Comparisons of several models. Journal of Geophysical Research 108 (D7), 4213, doi:10.1029/2002JD002697.

Laaksonen, A., Korhonen, P., Kulmala, P., Charlson, R., 1997. Modification of the Köhler equation to include soluble trace gases and slightly soluble substances. American Meteorological Society, 55, 853-862.

Langner, J., Rodhe, H., 1991. A global three-dimensional model of the tropospheric sulfur cycle.Journal of Atmospheric Chemistry 13,225-263.

Lanser, D., Verwer, J.G., 1999. Analysis of operator splitting for advection-diffusion-reaction problems from air pollution modelling. Journal of computational and applied mathematics, 111,201-216.

Leriche, M., Voisin, D., Chaumerliac, N., Monod, A., Aumont, B., 2000. A model for tropospheric multiphase chemistry: Application to one cloudy event during the CIME experiment. Atmospheric Environment 34 (29/30), 5015-5036.

Leriche, M., Chaumerliac, N., Monod, A., 2001. Coupling quasi-spectral microphysics with multiphase chemistry: A case study of a polluted air mass at the top of the Puy de Dome mountain (France). Atmospheric Environment 35, 5411-5423.

Leriche, M., Deguillaume, L., Chaumerliac, N., 2003. Modeling study of strong acids formation and partitioning in a polluted cloud during wintertime. Journal of Geophysical Research 108 (D14), 4433, doi:10.1029/2002JD002950.

Lelieveld, J., Crutzen, P.J., 1996. The role of clouds in tropospheric photochemistry. Journal of Atmospheric Chemistry 12, 229-267.

Liu, X., Seidl, W., 1998. Modelling study of cloud droplet nucleation and in-cloud sulfate production during the Sanitation of the Atmosphere (SANA) 2 campaign. Journal of Geophysical Research 103(D13), 16145-16158.

Long, A.B., Manton, M.J., 1974. On the evaluatin of the colection kernel for the coalescence of water drops.Journal of Atmospheric Science 31, 1053-1057.

Mauersberger, G., 2005. ISSA (Iterative Screening and Structure Analysis) - a new reduction method and its application to the tropospheric cloud mechanism RACM/CAPRAM2.4. Atmospheric Environment, in press.

Müller, F., 2001. Splitting error estimation for micro-physical-multiphase chemical systems in meso-scale air quality models. Atmospheric Environment, 35, 5749-5764.

Pilinis, C., 1991. Derivation and numerical solution of the species mass distribution equations for multicomponent particulate systems. Atmospheric Environment, 24A, 1923-1928.

Pitzer, K.S., 1991. Activity coefficients in electrolyte solutions. Second edition, London, CRC Press, Boca Raton.

Pruppacher, H.R., Klett,J.D., 1997. Microphysics of Clouds and Precipitation. Kluwer Academic Publishers, Dordrecht Netherlands.

Rasch, P.J., Barth, M.C., Kiehl, J.T., Schwartz, S.E., Benkovitz, C.M., 2000. A discription of the global sulfur cycle and its controlling processes in the National Center for Atmospheric Research Community Climate Model Version 3. Journal of Geophysical Research 105, 1367-1385.

Roelofs, G.J.H., 1993. A cloud chemistry sensitivity study and comparison of explicit and bulk cloud model performance. Atmospheric Environment., 27A-15,2255-2264.

Rogers, R.R., Yau, M.K., 1989. A short course in cloud physics. Pergamon Press.

Sandu, A., Potra, F.A., Charmichael, G.R., Damian, V., 1996. Efficient implementation of fully implicit methods for atmospheric chemical kinetics. Journal of Computational Physics 129, 101-110.

Sandu, A., Verwer, J.G., Van Loon, M., Charmichael, G.R., Potra, F.A., Dabdub, D., Seinfeld, J.H., 1997. Benchmarking stiff ODE solvers for atmospheric chemistry problems I: Implicit versus explicit. Atmospheric Environment 31, 3151-3166.

Sandu, A., Verwer, J.G., Van Loon, M., Spee, E.J., Charmichael, G.R., Potra, F.A., 1997. Benchmarking stiff ODE solvers for atmospheric chemistry problems II: Rosenbrock solvers. Atmospheric Environment 31, 3151-3166.

Doms, G., Schättler, U., 1999. The Nonhydrostatic Limited-Area Model *LM* (Lokal Model) of DWD: II. Implementation Documentation (Version *LM*-F90 1.35). German Weather Service, Offenbach.

Schwartz, S.E., 1986. Mass transport considerations pertinent to aqueous phase reactions of gases in liquid water clouds. NATO ASI Series, Vol. G6, Chemistry of Multiphase Atmospheric Systems. Springer, Berlin, 415-471.

Sehili, A.M., Wolke, R., Knoth, O., Simmel, M., Tilgner, A., Herrmann, H., 2005. Comparison of different model approaches for the simulation of multiphase processes. Atmospheric Environment, in press.

Sehili, A.M., Wolke, R., Helmert, J., Simmel, M., Schröder, W., Renner, E., 2005. Cloud chemistry modeling: Parcel and 3D simulations. In: Borrego, C., Norman, A.L. (EDs), Air Pollution Modeling and Its Application XVII, Kluwer Academic Publishers, New York, in press.

Simmel, M., Trautmann, T., Tetzlaff, G., 2002. Numerical solution of the stochastic collection equation - Comparison of the linear discrete method with other methods. Atmospheric Research, 61, 137-150.

Simmel, M., Diehl, K., Wurzler, S., 2005. Numerical simulation of the microphysics of an orographic cloud: Comparison with measurements and sensitivity studies. Atmospheric Environment, in press .

Simmel, M., Wurzler, S., 2005. Condensation and nucleation in sectional cloud microphysical models based on the Linear Discrete Method. Atmospheric Research, accepted.

Sportisse, B., 2000. An Analysis of operator splitting techniques in the stiff case.Journal of computational physics., 161,140-168.

Srivastava, R.C., 1971. Size distribution of raindrops generated by their break up and coalescence. Journal of Atmospheric Science, 28, 410-416.

Stockwell, W.R., Kirchner, F., Kuhn, M., Seefeld, S., 1997. A new mechanism for regional atmospheric chemistry modeling. Journal of Geophysical Research 102 (D22), 25847–25879.

Tilgner, A., Majdik, Z., Sehili, A.M., Simmel, M., Wolke, R., Herrmann, H., 2005. SPACCIM Simulations of Multiphase Chemistry occuring in the FEBUKO Hill-Capped Cloud Experiments. Atmospheric Environment, in press.

Trautmann, T., Wanner, C., 1999. A fast and efficient modified sectional method for simulating multicomponent collisional kinetics. Atmospheric Environement 33, 1631-1640.

Tzivion, S., Feingold, G., Levin, Z., 1987. An efficient numerical solution to the stochastic collection equation. Journal of Atmospheric Science 41, 1648-1661.

Verwer, J.G., 1994. Gauss-Seidel iteration for stiff ODEs from chemical kinetics. SIAM Journal of Scientific Computing 15, 1243-1250.

Verwer, J.G., Simpson, D., 1995. Explicit methods for stiff ODEs from atmospheric chemistry. Applied Numerical Mathematics 18, 413-430.

Verwer J.G., Hundsdorfer W., Blom J.G., 1998. Numerical time integration for air pollution models. Modelling, Analysis and Simulation (MAS). CWI Report MAS-R9825, Centre for Mathematics and Computer Science, Amsterdam.

Verwer J.G. and Sportisse B., 1998. A note on operator splitting in a stiff linear case. CWI Report MAS-R9830, Centre for Mathematics and Computer Science, Amsterdam.

Verwer J.G., Spee E.J., Blom J.G., Hundsdorfer W., 1999. A second order Rosenbrock method applied to photochemical dispersion problems. SIAM Journal of Scientific Computation., 20, 456-480.

Walcek, C.J., Taylor, G, 1986.A theoretical method for computing vertical distributions of acidity and sulfate production within cumulus clouds. Journal of Atmospheric Science, 43, 339-355.

Whitby, E.R., MC Murry, P.H., 1997. Modal Aerosol Dynamics Modeling. Aerosol Science and Technology 27, 673-688.

Wolke, R., Knoth, O., 2000. Implicit-explicit Runge-Kutta methods applied to atmospheric chemistry-transport modelling. Environmental Modelling and Software 15, 711-719.

Wolke, R., Knoth, O., Herrmann, H., 2001. Numerical treatment of aqueous phase chemistry in atmospheric chemistry transport modelling. Air Pollution Modeling and Its Application XIV. Kluwer Academic / Plenum Publishers, New York, pp. 399-407.

Wolke, R., Knoth, O., 2002. Time-integration of multiphase chemistry in size-resolved cloud models. Applied Numerical Mathematics 42, 473-487.

Wolke, R., Sehili, A.M., Knoth, O., Simmel, M., Tilgner, A., Hermann, H., 2005. SPACCIM: A parcel model with detailed microphysics and complex multiphase chemistry. Atmospheric Environment, in press.

Wolke, R., Hellmuth, O., Knoth, O., Schröder, W., Renner, E., 2004 b. The parallel model system LM-MUSCAT for chemistry-transport simulations: Coupling scheme, parallelization and application. In: Parallel Computing: Software Technology, Algorithms, Architectures, and Applications (Series: Advanced in Parallel Computing), edited by G.R. Joubert, W.E. Nagel, F.J. Peters, and W.V. Walter. Elsevier, The Netherlands, 363-370.

Zaveri, R.A, Easter, R.C., Wexler, A.S., 2005. A new method for multicomponent activity coefficients of electrolytes in aqueous atmospheric aerosol. Journal of Geophysical Research. 110, D1, D01202 10.1029/2004JD004681.